

**Exhumation history and tectonic across the  
Hardangerfjord Shear Zone, using apatite fission track  
thermochronology**

**Kurnia Juli Utami**



**Thesis for the degree Master Science**

**Department of Earth Science**

**University of Bergen**

**2012**

## ACKNOWLEDGEMENTS

I would like to thank my supervisors, Joachim Jacobs and Håkon Fossen. I thank Joachim for his encouragement, guidance, and advice throughout my time as a master student. I also thank him for help me in the field, and correction my thesis.

I thank Fabian Kohlmann for always willing to assist me, accompany me during field trip, help me with the microscope stuff, correcting my drafts and giving comments, sharing his knowledge about apatite fission tracks, and give me solutions for the problems appeared in my work. You are my hero.

I am grateful for Martina Suppersberger. You are really super nice and helpful with very boring laboratory works. I thank also to Mariella for helping me making thin sections, Corine David and Anna Ksienzyk for assist me during the last step of preparing the mounts and giving me the whole samples.

I would like to thank my colleagues in the geodynamic group especially Karen C. Johanessen and Bjørgunn Dalslaen who has been helpful and very patient to correct my bad writing. Also thanks to my friends in the U101 room, Donald, Irina Dumitru and Isaac who always encourage and support me. You made my day. A great thank to Indonesian community in Bergen, thank and proud to be part of you. I also would like to thank my parents and siblings for their support.

Finally, to my husband Muhammad Fachri, thank you very much for your love and support. To my son, Rumi Robbani Rafsanjani, you are my sun. Your encouragement has been a tremendous source of motivation for me to accomplish this master thesis.

Kurnia Juli Utami

Bergen, 7<sup>th</sup> of February 2012

## ABSTRACT

The Hardangerfjord Shear Zone (HSZ) is a large scale, ductile low angle shear zone, with SW-NE trending and NW dipping direction in the Caledonian crust. This zone has been formed at about 408-402 Ma (Fossen, 1992, 2000). A set of brittle faults formed about ~367 Ma (Schärer, 1980), northeast of the Hardangerfjord area, known as the Lærdal-Gjende Fault. Offshore, a set of brittle faults with NE-SW orientation, known as the Ling depression, may be linked to the HSZ in southwest. The North Sea area has protracted several rifting events following the Caledonian Orogenic collapse. The successive rifting events are believed responsible to the reactivation of the HSZ.

By applying apatite fission track analysis, the possible reactivation of the HSZ was tried to be unrevealed, which could be reflected by an offset of Apatite Fission Track (AFT) ages between the two blocks. Five thermal history models were also developed to unravel the thermal histories of the rocks in the study area.

The AFT ages show a significant difference between the two blocks whereas the samples were taken from the hanging wall of the HSZ have AFT ages range from  $146.2 \pm 9.3$  Ma –  $227.4 \pm 14.3$  Ma, with a weighted mean age of  $174 \pm 12$  Ma (Middle Jurassic). Meanwhile, from the footwall is obtained AFT ages range of  $180 \pm 8.4$  -  $105.6 \pm 7.9$  Ma, and the weighted mean is  $145 \pm 16$  Ma (Late Jurassic – Early Cretaceous time).

The thermal history models result that the two blocks was subjected to a reactivation at about 250-180 Ma. This Permian cooling rate is rather slow about  $1.5^0\text{-}3^0\text{C/Ma}$ . The second cooling event initiated at early Jurassic time, and only reactivated the footwall of the HSZ. It was documented in sample BG-62 which describes cooling rate of  $6^0\text{C/Ma}$  at 190-180 Ma and shows a steep gradient. Both the cooling events occurred coincided to the Permian and Jurassic rifting in the North Sea. The area then experienced the burial event at the Middle Jurassic-Middle Cretaceous coincided with a period of transgression at Middle-Late Cretaceous (Doré, 1992; Riis, 1996). It is predicted from the cooling rate that the cooling event in the area occurred due to tectonic and erosional process.

## TABLE OF CONTENTS

<b>ACKNOWLEDGEMENTS</b>	ii
<b>ABSTRACT</b>	iii
<b>TABLE OF CONTENTS</b>	iv
<b>1. INTRODUCTION</b>	1
<b>1.1 Introduction and Research Objective</b>	1
<b>1.2 The Study Area</b>	4
<b>1.3 Previous Low Thermochronology Studies in Southern Norway</b>	5
<b>2. GEOLOGICAL SETTING</b>	9
<b>2.1 Baltica during the Pre-Caledonian Orogeny</b>	9
<b>2.2 Caledonian Orogeny</b>	9
<b>2.3 Norway in the Scandian Event</b>	10
<b>2.4 Norway in the late-to post-Scandian Event</b>	12
2.4.1 <i>Devonian Extension</i>	13
2.4.2 <i>Middle Paleozoic Stability and Cooling event in the Permo-Carboniferous</i>	15
2.4.3 <i>Norway in Permian-Triassic times</i>	16
2.4.4 <i>Norway in Jurassic times</i>	20
2.4.5 <i>Norway in the Cretaceous</i>	21
2.4.6 <i>Norway during the Cenozoic</i>	22
<b>2.5 Geological Framework of the Present Study</b>	26
<b>3. APATITE FISSION TRACK METHODOLOGY</b>	30
<b>3.1 General</b>	30
<b>3.2 Apatite Properties</b>	31
<b>3.3 Track Formation Process and Theory</b>	32
<b>3.4 Track Exposure</b>	34
<b>3.5 Fading and Annealing of Fission Tracks</b>	35
3.5.1 <i>Fission Track Length</i>	35
3.5.2 <i>Fission Track Annealing</i>	36

3.5.3 <i>Partial Annealing Zone (PAZ)</i>	36
<b>3.6 Dating Procedures</b>	40
3.6.1 <i>External Detector Method (EDM)</i>	40
<b>3.7 Fundamental and Practical Fission Track Age Equation</b>	42
<b>3.8 Dating System and Calibration</b>	45
<b>3.9 Data Analysis and Statistics</b>	46
3.9.1 <i>Error in the Age Determination</i>	48
3.9.2 <i>Age Component Analysis</i>	48
<b>3.10 Samples Preparation</b>	49
3.10.1 <i>Crushing and Density Separation</i>	49
3.10.2 <i>Magnetic Mineral Separation</i>	49
3.10.3 <i>Heavy Liquid Separation</i>	50
3.10.4 <i>Sample Mounting, Polishing and Cutting</i>	50
3.10.5 <i>Etching and Packing</i>	51
3.10.6 <i>Unpacking</i>	51
<b>3.11 Microscopy and Modelling</b>	52
3.11.1 <i>Calculating the <math>\zeta</math> Calibration Factor and AFT Ages</i>	53
3.11.2 <i>Track Length Measurement and <math>D_{par}</math></i>	56
3.11.3 <i>Thermal History Modeling</i>	57
<b>4. RESULTS</b>	60
<b>4.1 Field Structural Data and Analysis</b>	60
4.1.1 <i>Fracture Analysis</i>	62
4.1.2 <i>Fault Analysis</i>	64
4.1.3 <i>Foliation Analysis</i>	65
<b>4.2 Result of AFT</b>	65
4.2.1 <i>Apatite Description</i>	66
4.2.2 <i>Zeta Calibration Factor</i>	66
4.2.3 <i>AFT Data and Inverse Thermal Modelling</i>	67
4.2.3.1 <i>Footwall of the Hardangerfjord Shear Zone</i>	67

<i>4.2.3.2 Hanging wall of the Hardangerfjord Shear Zone</i>	72
<i>4.2.3.3 Hanging wall of the Bergen Arc Shear Zone</i>	72
<i>4.2.4 AFT Diagrams</i>	73
<i>4.2.4.1 AFT Age Variation along the Profile</i>	74
<i>4.2.4.2 AFT Age vs. Elevation</i>	74
<i>4.2.4.3 AFT Age vs. Mean <math>D_{par}</math></i>	75
<i>4.2.4.4 AFT Age vs. MTL</i>	76
<i>4.2.4.5 MTL vs. Mean <math>D_{par}</math></i>	76
<b>5. DISCUSSION AND INTERPRETATION</b>	77
<b>5.1 Interpretation of the AFT data</b>	77
<i>5.1.1 AFT Ages</i>	77
<i>5.1.2 Zeta Calibration</i>	78
<i>5.1.3 Mean Track Length and <math>D_{par}</math></i>	78
<i>5.1.4 Comparison of AFT Ages vs. Elevation</i>	80
<i>5.1.5 Comparison of AFT ages and annealing kinetic parameters</i>	81
<b>5.2 Evaluation of the Inverse Thermal History Model</b>	82
<b>5.3 Movement of Faults</b>	86
<b>5.4 Comparison to Previous Studies</b>	89
<b>5.5 Proposed Exhumation History of the HSZ</b>	92
<b>6. CONCLUSION</b>	97
<b>REFERENCES</b>	99
<b>APPENDIX</b>	111

# 1. INTRODUCTION

## 1.1 Introduction and Research Objective

The Scandinavian North Atlantic passive margin includes not only the offshore and basin domains but also large portions of the onshore domains of the Scandinavian Caledonides. The passive margin is located between the continent-ocean boundary (COB) and the Innermost Boundary Fault system (IBF) (Fig. 1.1). The boundaries of the IBF are determined by geomorphic features (morphology, water/glacial divides, topographic crest), structural features (normal faults), uplift data, and geophysical data. Hence, the IBF are visually expressed by a set of linked normal west dipping crustal faults, which extends over a distance exceeding 2000 km from the North Sea, across the Caledonian mountain belt to the Barents Sea. The position of the IBF system is associated with the position of the rift flank (Mosar, 2003). Rift flanks develop as a result of succession uplifts induced either thermally or mechanically along the IBF (Kooi and Cloetingh, 1992).

A state of stress may influence a development of the basins, especially intraplate stress. This stress could be compression stress which could produce relative uplift of the basin flank, subsidence at the basin centre, and seaward migration of the shoreline. Increasing the level of tensional stress however, induces widening of the basin, subsidence of the basin flank, and thus causes landward migration of the shoreline (Kooi and Cloetingh, 1992). Therefore, a rifting activity which involves crustal stretching by tensional stress either acceleration of subsidence would certainly give effects to the basin flank and shifting of the shoreline.

The North Sea area has protracted several rifting events following the Caledonian Orogenic collapse. In the North Sea, rifting started in the Permian which related to the separation of Greenland and Norway (Torsvik et al. 2002). Furthermore, the major rifting events occurred also in the Permian/Triassic, Late Jurassic/Early Cretaceous and Late Cretaceous/Early Tertiary (Brekke, 2000). Nevertheless, continental rifting cannot be solely regarded as a responsible factor for repeated faults reactivation and uplift. Another factor which triggers the faults reactivation may be derived by the latest phase of pre-drift extension (Redfield et al. 2005).

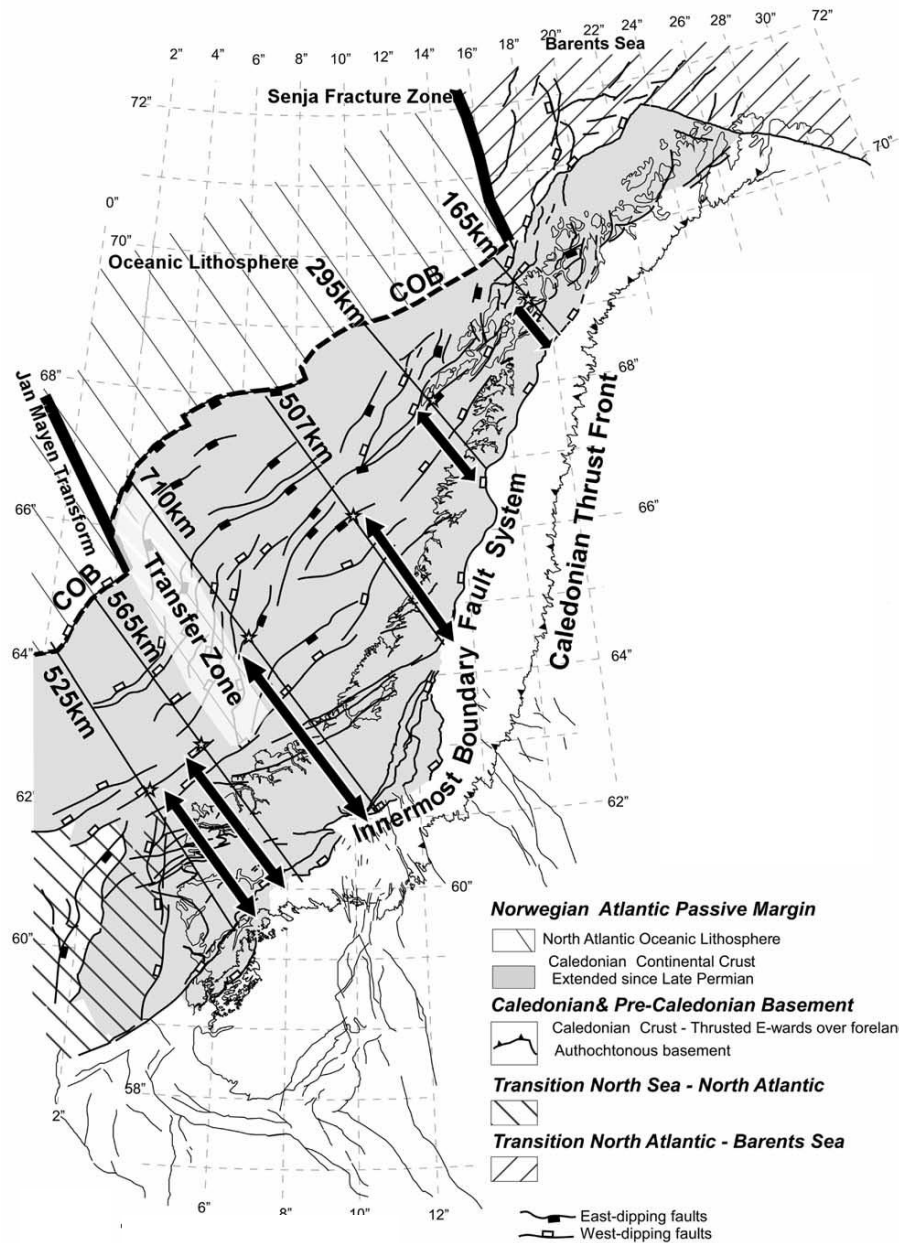


Fig.1.1: Map shows a simplified tectonic map of the Scandinavian North Atlantic passive margin. The map indicates the position of the innermost boundary fault system (IBF) and the present location of the Caledonian thrust front. Only the main normal faults are outlined. Margin width is represented by six different cross lines. (Mosar, 2003)

The Hardangerfjord Shear Zone (HSZ) is a large scale, ductile low angle shear zone, with SW-NE trending and NW dipping direction in the Caledonian crust. This shear zone is also part of the IBF system (Mosar, 2003). As an element of the IBF system, the HSZ has been formed at about 408-402 Ma, when kinematics reversed from convergent to divergent motions (Fossen, 1992, 2000). Later or simultaneous sets of brittle faults formed, such as the Lærdal-Gjende fault in the Lærdal-Gjende area, northeast of the Hardangerfjord area. This brittle fault zone dies out between Aurland and the Hardangerfjord. Offshore, a set of brittle faults with NE-SW orientation, known as the Ling depression, may be linked to the HSZ in southwest. Both of these fault systems represent reactivation along the HSZ, with a total length of at least 600 km.



The extensional deformation of the Scandinavian orogeny generated a rapid denudation of the orogen. Many of the detachment faults in western Norway exhume the lower crustal rocks to the surface. Meanwhile Devonian basins are formed in the upper plate (hanging wall) due to extensional deformation (Andersen, 1995). The Nordfjord-Sogn Detachment fault (NSDZ) is one example, which is located northward of the HSZ. Many of the Devonian basins developed on the hanging wall of the NSDZ, namely the Hornelen basin, Solund basin, Kvamshesten basin and Håsteinen basin.

Several evidences along and adjacent of the HSZ prove a similar characteristic to those in the NSDZ. According to the gravity modeling (Hurich and Kristoffresen, 1988) displayed that the HSZ bounds a half-graben in the offshore which contain up to 10 km of the Caledonian allochthons. These allochthons consist of Devonian sediments, supported by boreholes drilled on the Utsira High, located north of the HSZ. It is therefore inferred that down-to-the-NW movements on the HSZ associated with the deposition of Devonian sediments in the hanging wall (Færseth et al, 1995).

The reconstruction of the bedrock map of southern Norway displays a footwall uplift of the HSZ reaching 800-1000 m. The contour map also shows a similar trend parallel to the HSZ, in an area about 40-50 km to the SE of Hardangerfjord (Fossen and Hurich, 2005). Other evidence obtained from shallow drilling has revealed a thin Jurassic sequence in the mouth of the Hardangerfjord (Rokoengen and Sørensen, 1990). These evidences imply that the HSZ may have experienced reactivation in the Permo-Triassic, even though the main displacement is assigned to Devonian normal faulting (Færseth et al, 1995).

In this study, we try to unravel the exhumation history in the south western part of the HSZ by means of a low temperature-thermochronological technique, apatite fission track analysis. With application of this method, it is also attempted to determine patterns and the timing of possible vertical movements along the HSZ. This possible reactivation could be reflected by an offset of Apatite Fission Track (AFT) ages between tectonical blocks in this area in combination with structural data analysis, geological and topographical data. Another objective of this study is to unravel the thermal histories of the rocks in the study area, to obtain new insight into the exhumation and uplift history of the outer Hardangerfjord region.

## 1.2 The Study Area

The research area is located in Sunnhordland, between north latitude  $59^{\circ} 24' 57.09''$ -  $60^{\circ} 13' 46.28''$  and east longitude  $5^{\circ} 10' 39.43''$ - $5^{\circ} 49' 55.83''$  (Fig. 1.2). The total size of the study area is about 60 km x 96 km. The study area covers islands namely Bømlo, Sveio and Stord. Between the Bømlo and Stord in the north, and Sveio in the south, it is located the Bømløfjorden which stretches out from the mouth of the fjord in southwest toward inland along approximately 40 km. The Bømløfjorden in the northeast has a border with the Kvinnheradjorden which extends 45 km inland. The well known Hardangerfjorden is located further inward and has a boundary with a small fjord the Eidfjorden. The morphology is rugged, with high mountains and deeply incised valleys and fjords with elevations are ranging from 150-300 m.a.s.l., up to 750 m.a.s.l.

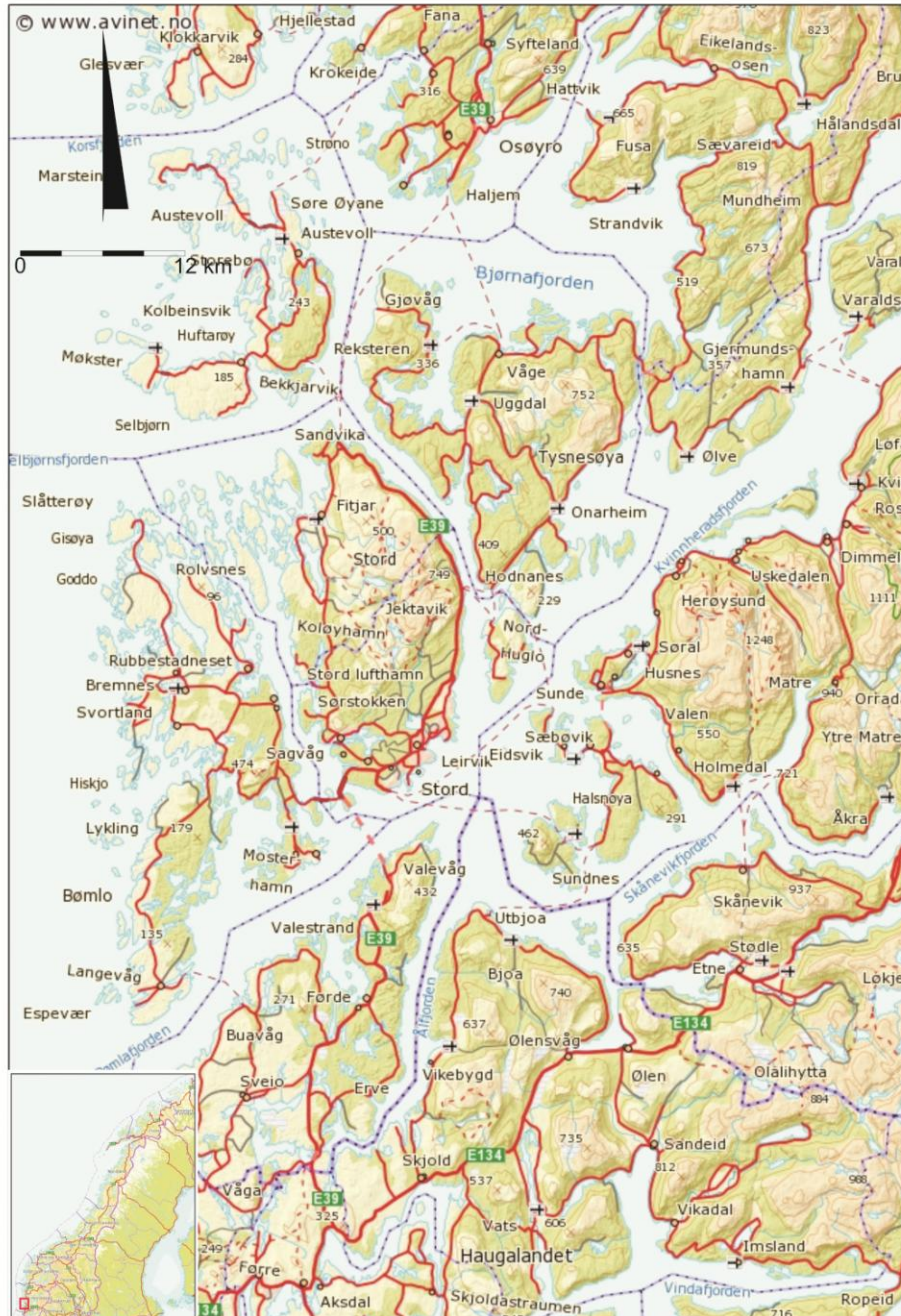


Fig. 1.2: Topographical map of the study area envelopes the main islands of Bømlo, Stord and Sveio. Inset is an index map of Norway with red box indicating the study area.

### 1.3 Previous Low Thermochronology Studies in Southern Norway

Several fission tracks thermochronological studies have been carried out in the Scandinavian region. These were focused locally on restricted small areas (e.g. Andriessen and Boss, 1986; Rohrman et al., 1994; Hansen et al., 1996; Redfield et al., 2005) or they are compiling data in

order to interpret regional data sets (e.g. Rohrman et al., 1995; Hendriks et al., 2007). Most of the data sets are derived from apatite, and few of them obtained from zircon and sphene.

The post-Caledonian uplift and denudation history of the Eidfjord crustal segment in the inner Hardangerfjord area was first observed by Andriessen and Boss (1986). Applying method was apatite, zircon fission track analysis as well as K-Ar and Rb-Sr dating of biotite. All of the samples were collected from Eidfjord granites and overthrust granitic gneisses. Dating using Rb-Sr yielded a mean age 390 Ma, which was coeval with the termination of the Caledonian metamorphism. The AFT ages yield ages between 166-110 Ma, and display a proportional function between increasing ages and the topographical altitude. Calculation using the ages of mineral pairs with different closure temperature results that the rapid uplift rate of 0.1 mm/a occurred at 80 Ma. The uplift rate was slower, approximately 0.03 mm/a between 166-110 Ma. All of the calculations are based on the assumption a geothermal gradient 30<sup>0</sup>C/km.

In order to clarify the syn- and post-rift thermal evolution of the Oslo Rift, Rohrman et al. (1994) examined the area by applying fission track data of apatites, zircons, and sphenes. The zircons and sphenes within the rift record fission track ages of between 270–180 Ma. The period between 270-260 Ma is inferred as a result of large scale batholiths intrusions, or syn-rift advective heating. The ages between 220-180 Ma are referred to as a post-rift heating induced by hydrothermal circulation. The data derived from apatite fission track data show a variation of the post-rift history from Triassic age (200-240 Ma) in the southeast areas and the Jurassic (~160 Ma) in the northwestern part. The results from inverse thermal history modelling using mean track length distributions, suggest that various denudation events occurred in the Triassic, Jurassic, and Neogene. The timing of the Triassic-Jurassic denudation is coeval with the migration of the rifting from the Oslo-Skagerrak area to the North Sea basin.

Rohrman et al. (1995) sampled the areas of Hunnedalen, Gausta, Jotunheimen and Eidfjord in southern Norway. Those samples were obtained mostly from the Precambrian and Paleozoic basement. The AFT ages show two major phases of rapid exhumation. The first is the Mesozoic phase, which started in the Triassic (220 Ma) in the east and south of the study area, and drifted to the west at Jurassic time (160 Ma). It is attested by thick continental clastic deposits in the Triassic-Jurassic half grabens in the North Sea basins. The second event is the Neogene phase, which were concluded based on forward modeling of “stacked” age-elevation plots and inversion of measured mean track length distributions. Their model suggests that

variations of the isochrones of the AFT ages are drawn from offshore in west Norway to Baltic shield delineate a domal type. Evidences of the Neogene uplift are also corroborated by basinward dipping pre-Neogene strata and the infill of a 1-2 km thick Neogene sediment wedge. In addition, the last exhumation event is coincided with the Oligocene and Pliocene plate reorganizations in the North Atlantic.

A study about the Post-Sveconorwegian exhumation was undertaken by collecting samples in the monzonitic dyke rocks which intruded the Høvringsvatn Complex in southern Setesdal area (Hansen et al. 1996). The methods used in this study are apatite and titanite fission track analysis. The sphene fission track results vary between 590-790 Ma. These ages indicate that the temperature in the host rocks cooled below circa 250<sup>0</sup>-200<sup>0</sup>C after the Sveconorwegian Orogeny. The AFT ages show a long period of constant cooling since 250-300 Ma. It is then inferred that the cooling path may be attributed to the removal of overlying volcanic and sedimentary rocks forming a sub-Permian peneplain.

The Møre-Trøndelag Fault Complex (MTFC) was re-evaluated by Redfield et al. (2005) by combining new structural data, elevation profiles from the DEM (Digital Elevation Model), drainage patterns and previous compilation of common-elevation AFT ages produced by Hendriks et al. (2004). Plotting of distribution AFT age data versus elevation along southern and mid Norway toward the Gulf of Bothnia indicates that the younger AFT ages reside near the topographic highs of the southern and northern Scandes. In this compilation AFT ages also reveal a distinctly asymmetric distribution of cooling on the western rift flank. Unlike Rohrman et al. (1995) who proposed a theory of *domal* uplift for the distribution of the AFT ages, Redfield et al. (2005) yet introduce a flexed, on its margin thinned but not-quite-broken lithospheric plate; a typical for young margin development. The reactivated faults would be uplifted in the core, neighboring a down-faulted retreating scarp. Westward shifting of the drainage patterns also infers landward migration of the flanks result of the reactivation of the fault strands. The AFT data surrounding the MTFC reflect vertical offset rather than chemical differences, differential sedimentary burial or erosion. The biggest displacement can be found in the southwest areas, which also coincided with the very different AFT ages close by. While, the AFT age in the northeastward MTFC tend to be juxtaposed, indicating a smaller faults displacement.

The scattered AFT ages delimits interpretation only on the local area. Therefore, Hendriks et al. (2007) tried to compile these data encompassing a range of the passive Norwegian Atlantic

margin in the west to the cratonic Archean province in northwestern Russia and Finland in the east. Plotting of the AFT ages versus the mean track length generates a typical boomerang pattern. The plotting demonstrates that the older ages with long MTLs (Mean Tracks Length) are originated from cratonic interior samples in Finnland. Intermediate AFT ages have the lowest MTLs which are mean they have spent the longest time in the Partial Annealing Zone (PAZ) prior to cooling. The youngest ages with long MTLs derived from samples in the north Atlantic passive margin and southern Norway. The compilation of the AFT ages data also clearly represents vertical movements in the Mesozoic and Cenozoic along the Norwegian Atlantic margin, and those occurred at Paleozoic times in the cratonic interior.

Several other studies and projects at the University of Bergen have been undertaken and now still progressing. Two master theses have been published by Johansen (2008) and Tørresen (2009), who investigated the exhumation history within and across the Bergen Arc. They proposed two possible exhumation scenarios. The first scenario is called a pinned divide landscape evolution which explains a differential rift flank uplift and exhumation in the late Jurassic. The second scenario involves uniform exhumation of the rift flank during the Permian and Triassic, followed by reactivation of pre-existing structures in Jurassic times. The newest master thesis by Magerholm (2010) was carried out across the Hardangerfjord, northeastward of the present study. The AFT ages presented in this thesis yield ages between 162-186 Ma (Jurassic times). The relatively young AFT ages and the associated mean track length distributions imply a long residence time in post-Permian times.

The geological setting of the present study will be discussed in the following chapter. The geological background of the area is discussed regionally at the beginning of the chapter, and more focus at the end of the chapter. The formation of the HSZ is during Devonian time; therefore the discussion is restricted about development of West Norway since the Caledonian Orogeny onward.

## 2. GEOLOGICAL SETTING

### 2.1 Baltica during the Pre-Caledonian Orogeny

The tectonic history of Baltica prior to the Caledonian Orogeny can be traced from the amalgamation of the Rodinia supercontinent which occurred from 900-750 Ma (Li et al., 2008). By *ca.* 750-630 Ma, the supercontinent was fragmented and each of the continental blocks moved away and collided (Cawood et al., 2001). Baltica became isolated after the break-up of the Rodinia supercontinent and did not amalgamate during the formation of Gondwanaland. In the latest Vendian (650-540 Ma), the Iapetus Ocean opened and formed a junction between a rift (Laurentia-Gondwana), a right lateral fault between Laurentia and Baltica, and a trench (inverted Baltica/Gondwana) probably around this time (Torsvik and Cock, 2005).

### 2.2 Caledonian Orogeny

The term 'Caledonian Orogeny' is restricted to the tectonic events within and on the borders of the Iapetus Ocean. The Caledonian Orogeny comprises several phases (McKerrow et al., 2000) or it has been defined as four or five orogenic events by Roberts (2003). The first is the Finnmarkian event which took place at around 505 Ma (Mørk et al. 1988). This event marked the collision between the Baltoscandian margin and a magmatic arc (Sturt and Roberts, 1991). The position of the magmatic arc was probably in the Ægir Sea between Baltica and Siberia (Hartz and Torsvik, 2002). The second one is the Trondheim event which was marked by ophiolite obduction upon epicontinental rocks of the Gula Complex (microcontinental fragment of Baltica) in the range of 480-475 Ma. In the early Arenig (488-478 Ma), Baltica had started to rotate anticlockwise away from Siberia (Torsvik et al., 1996). The third event, which took place about 470-450 Ma, is the Taconian. This event was marked by subduction and accretion, including eclogite generation along the continental margin of Laurentia. The fourth event was the Scandian which marked an oblique collision between Baltica and Laurentia at around 420-400 Ma (Fig. 2.1).



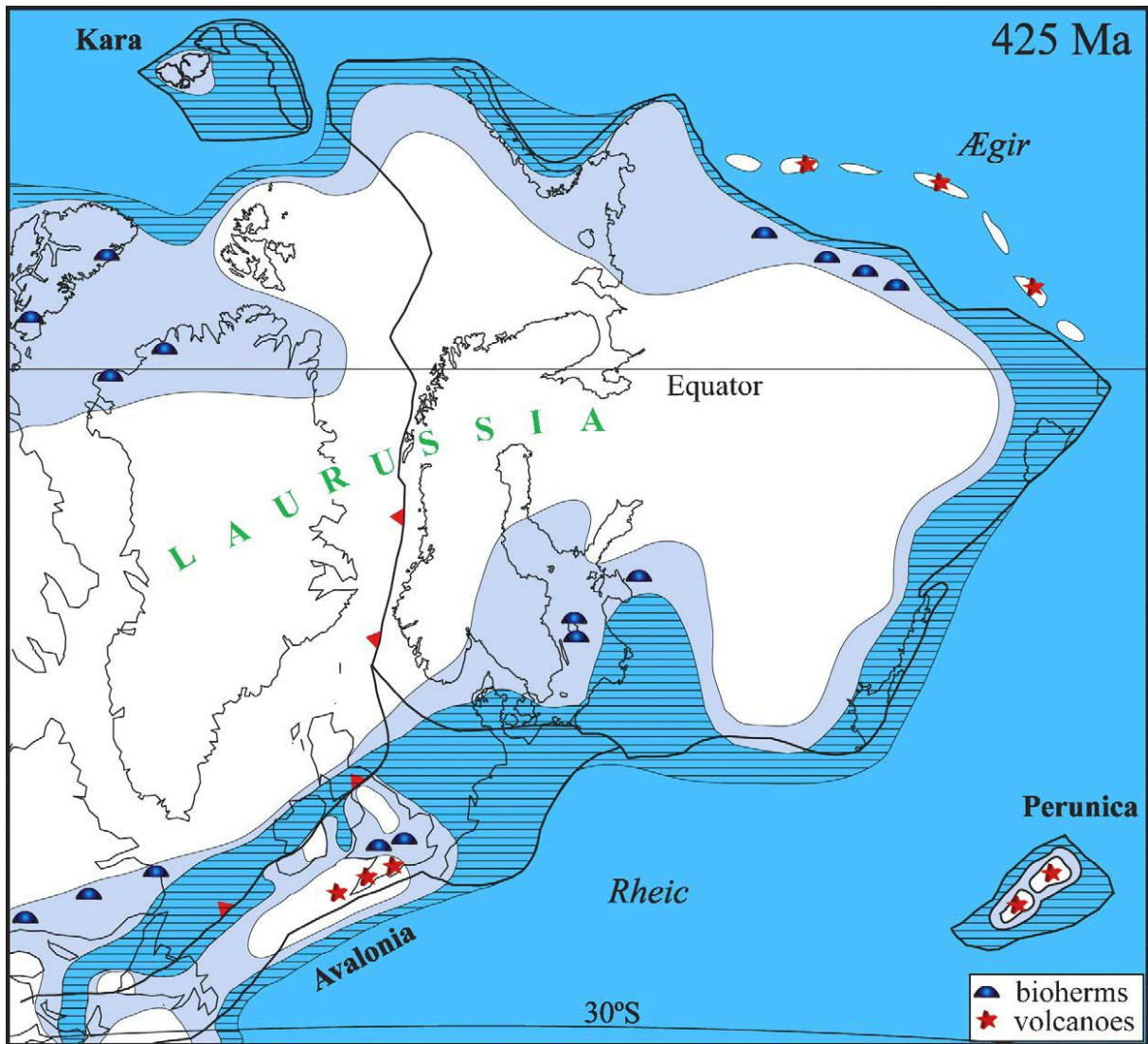


Fig. 2.1: Map shows geological reconstruction of Laurentia and Baltica (Laurussia) in the Middle Silurian or during the Scandian event. Baltica extended lengthways approximately from the equator to 20°S. The Iapetus Ocean had closed and the Rheic Ocean was starting to close (Cock and Torsvik, 2005).

### 2.3 Norway in the Scandian Event

The Scandian event involved a subduction of the Baltoscandian margin of Baltica beneath Laurentia. All the allochthons which include those affected by the earlier events (the Finnmarkian, the Trondheim and the Taconian) contribute to the Scandian event. Evidence from monazite geochronology collected from the Western Gneiss Region shows that both subduction and exhumation occurred within a short period of time, perhaps less than 10 Ma (Terry et al. 2000).

The Scandian event was also marked by the closing of the Iapetus Ocean and the collision between Baltica and Laurentia. Evidence of the event in mainland Norway can be seen by a



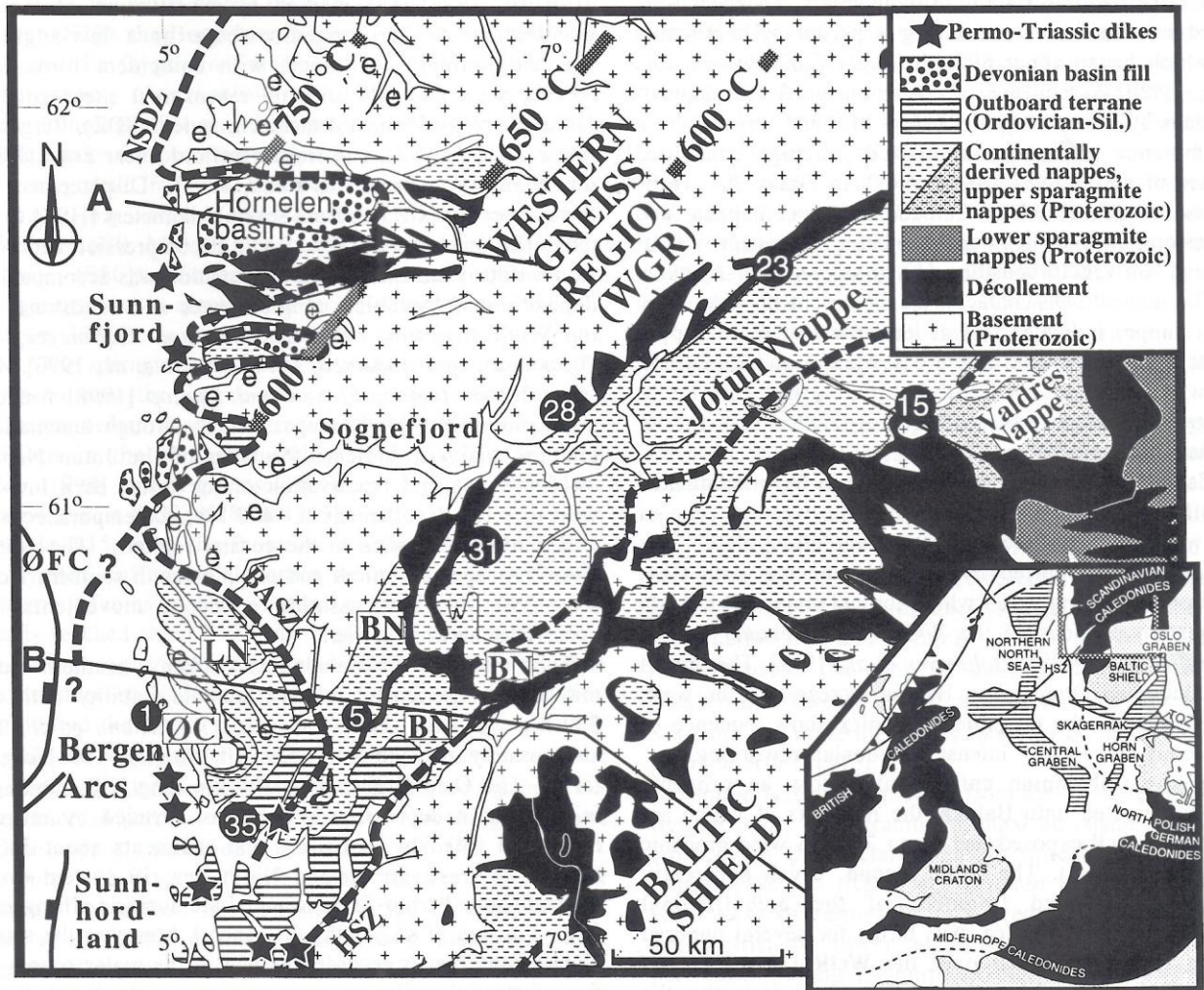
dominantly E vergent thrust with allochthons derived from the Baltoscandian platforms, the Iapetus terranes, and the Laurentian plate. Unlike in the mainland of Norway, the Caledonian Orogeny of Svalbard and the Barents Shelf was marked by splitting of the Caledonian bedrocks into four terranes generated by sinistral transtensional/transpressional regimes (Gee et al., 2008).

The basement of the W-directed subducted Baltica descended under the weight of the overriding Caledonian allochthons (nappes) which reached a crustal thickness up to 100 km (Dobrzhinetskaya et al., 1995) and metamorphic conditions of 28 kbars at 750<sup>0</sup> C in the Western Gneiss Region (see location in Fig. 2.2) (Griffin et al., 1985). This led to a deeper depression of the western margin with paleotemperature and pressure increasing toward the Norwegian coastal areas which is confirmed by the presence of high-pressure rocks such as eclogites, coesite and microdiamonds (Dobrzhinetskaya et al., 1995). Additionally, the Precambrian basement is gradually more reworked to the west.

<sup>40</sup>Ar/<sup>39</sup>Ar dating from the eclogites of the Lindås Nappe (see location in Fig. 2.2) demonstrates that the initial timing of cooling began early in the history of this orogen, *ca.* 450 Ma, followed by the exhumation at about 430 Ma, which coincides with the emplacement of the Bergen Arcs (see location in Fig. 2.2) (Boundy et al., 1996). However, U-Pb and Sm-Nd ages dating from the eclogites of the Western Gneiss Region show a cluster around 415-400 Ma (Kullerud et al., 1986) and about 425 Ma (Griffin and Brueckner, 1980, 1985). This implies that the Western Gneiss Region was subducted to extreme depth after the exhumation of the Lindås Nappe (see location in Fig. 2.2) and the emplacement of the Bergen Arcs (Boundy et al., 1996).

The allochthons were generally stacked with the most far transported ones at the top. Gee et al. (1985) grouped the thrust sheets which rest on autochthonous crystalline basement into the lower, middle, upper and uppermost allochthons. The lower and middle allochthons represent the pre-collisional continental margin of Baltica. The upper allochthons mainly consist of sedimentary and igneous rocks derived from the Iapetus Ocean and island arc complexes. The uppermost allochthons are characterized by exotic elements having an affinity to the Laurentian margin.

Fig. 2.2: The geologic map of the present study and adjacent areas. BASZ = Bergen Arcs Shear Zone, BN= Bergsdalen Nappes, HSZ=Hardangerfjord Shear Zone, LN = Lindas Nappe, NSDZ = Nordfjord-Sogn Detachment Zone, ØC = Øygarden Complex, ØFC = Øygarden Fault Complex (Dunlap and Fossen , 1998)



## 2.4 Norway in the late-to post-Scandian Event

The last and important event in the Caledonian Orogeny was the late-to post Scandian event which was initiated in the Devonian.

In relation to the contractional tectonism of the Scandian Event, extensional deformation might have taken place during syncollisional as well as after the contractional tectonics. Evidence of the syncollisional extension can be seen as orogen-parallel Caledonian lineations in the Bergen Arcs which may reflect lateral extension at a deeper level (Fossen, 2000). However, the exact timing of the syncollisional deformation is not very well constrained, probably between ~415 Ma and ~400 Ma (obtained through U-Pb and Sm-Nd dating of eclogites) which was accompanied with the initiation of a postorogenic extension (Dunlap and Fossen, 1998).

### 2.4.1 Devonian Extension

After the emplacement of the large thrust sheets with displacement in the order of 50 to 100 kilometers toward the foreland, the contractional tectonics ceased and an extensional regime became dominant. Three modes of post collisional extension which were proposed by Fossen (1992); Fossen and Dunlap (1998); and Fossen (2000) have been widely accepted. The Mode I extension (Fig. 2.3a) commenced at ~400 Ma as backsliding of an earlier ESE foreland-directed orogenic wedge shifted to WNW hinterland-directed kinematics along the basal décollement zone (Fossen 1992, 1993). The Caledonian décollement zone of the southern Norway consists of Late Precambrian to Early Paleozoic rocks (mostly phyllites and phyllonites) deposited on the Baltic Shield (basement). Fossen and Holst (1995) estimated about ~30 km of hinterland-directed translation of the orogenic wedge relative to the basement.

After the extensional tectonics by the reactivation of the basal décollement zone (Mode I), the entire crust subsequently collapsed by development of W and NW dipping extensional shear zones (Mode II, Fig 2.3b). The Hardangerfjord Shear Zone, Bergen Arc Shear Zones (BASZ) and Nordfjord-Sogn Detachment Zone (NSDZ) are major extensional shear zones formed at this stage (see locations in Fig. 2.2). It has been estimated that the lateral displacement of these shear zones is in the order of ~50 km based on the ~5 km thick mylonites found in the NSDZ (Fossen, 2000). The change of the transport direction of the orogenic wedge above the reactivated décollement zone is likely related to the exhumation of the décollement zone in the hinterland. The exhumation caused the original northwesterly dip of the décollement zone to decrease somewhat followed by rotation to a position that favored to top-to-the NW extensional reactivation.

The results of  $^{40}\text{Ar}/^{39}\text{Ar}$  thermochronology of muscovite from the NSDZ yield ages between 415 and 416 Ma (Fossen and Dunlap, 1998). It may indicate that cooling and extension had already been taken place in the hinterland concurrent with the general thrusting toward the foreland (this hypothesis has been explained by Kullerud et al., 1986). However, most of rocks ages about 402-394 Ma have also been reported from the area and are believed represent maximum ages for the late stage of Mode II extension. The closeness between the two groups of ages (the cooling and extension at 415-416 Ma and the estimation of subduction at the WGR of about 415-400 Ma) suggests a very rapid change from contractional to extensional regimes in Early Devonian times. This possible explanation is

also corroborated by the modelling of  $^{40}\text{Ar}/^{39}\text{Ar}$  data from K-feldspars which indicate a rapid cooling through the brittle-ductile transition in the early Devonian, followed by a very slow cooling (Dunlap and Fossen, 1998).

After the crustal collapse stage, the basement rocks crossed into the brittle domain which led to the formation of high angle brittle faults (Mode III, Fig. 2.3b). U/Pb dating from the basement fractures from west of Bergen yielded ages around 395 Ma, which indicate the time at which the rocks crossed the brittle-ductile transition (Pedersen et al., 1999). Kinematic fault analysis exhibits a consistent pattern of NW-SE extension and subvertical shortening (Fossen, 2000). A different trend is found in the areas to the north of the Bergen Arc which shows a more E-W direction, probably related to slip partitioning along the Møre-Trøndelag Fault Zone to the north of the present study area (Krabbendam and Dewey, 1998).

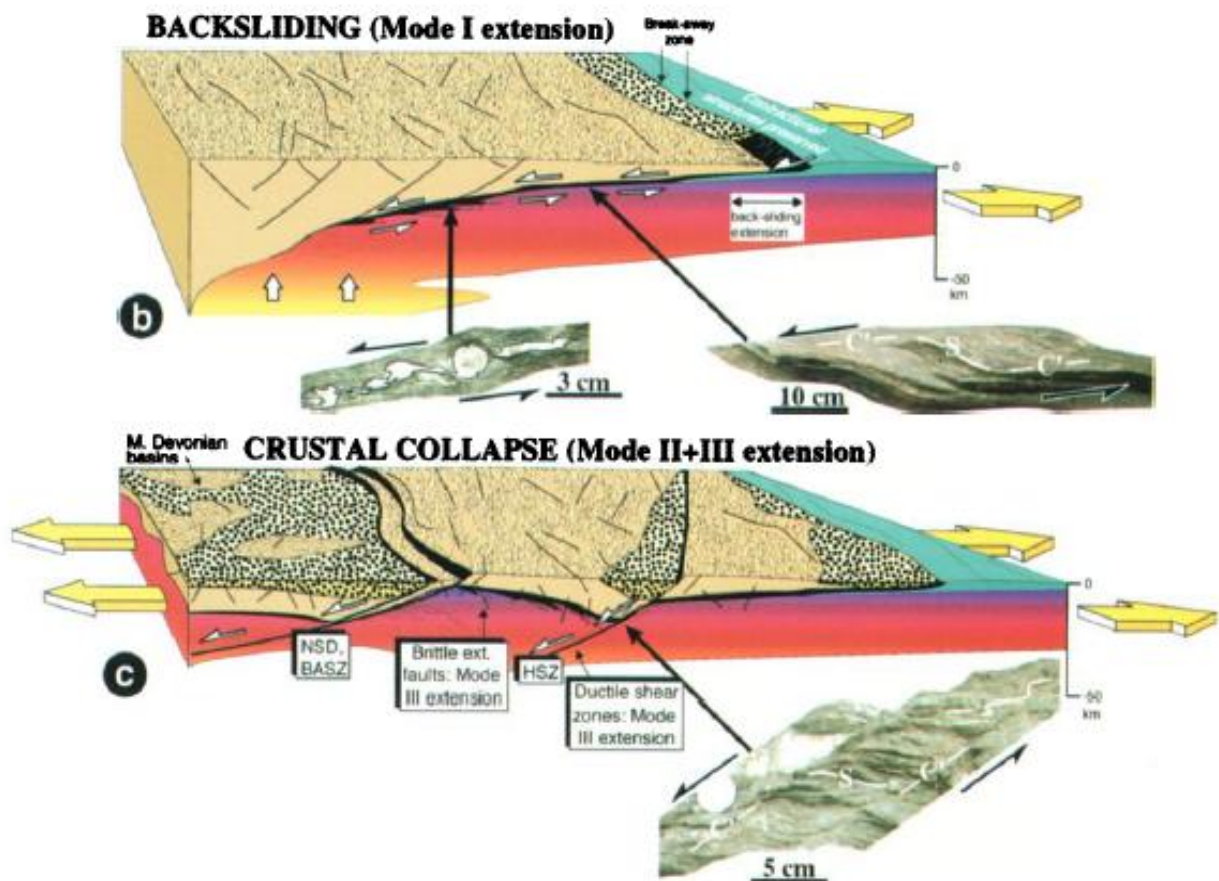


Fig. 2.3: The cartoon illustrates the three modes of post-collisional extensional tectonics in south Scandinavia proposed by Fossen (2000). (a) The transport direction of the previously ESE translated, foreland directed orogenic wedge changed to be a WNW due to backsliding along the basal décollement zone. (b) The crustal collapse stage was initiated by the development of W and NW dipping extensional shear zones (Mode II) and followed by the formation of brittle faults with NW-SE directed-extension (Mode III) (Fossen, 2000).

During the late to post orogenic extension of the Caledonian crust, the Devonian basins of western Norway formed in the hanging wall of the NSDZ (Osmundsen and Andersen, 2001). These Devonian basins include the Solund basin, the Hornelen basin (see locations in Fig. 2.2), the Håsteinen basin and the Kvamshesten basin. The presence of E-W folds parallel with extension direction of the basins is related to a releasing overstep of two major left lateral strike-slip faults, namely the Møre-Trøndelag Fault Zone (see location in Fig. 2.4) in Norway and the Highland boundary fault zone in Britain (Séranne et al., 1991). Chauvet and Séranne (1994) suggest that the folds formation were a result of buckling caused by compression perpendicular to the extension direction. From a regional perspective, this occurrence also indicates that the folds might be a product of a combination of the N-S Avalonia convergence and the palaeostress evolution during the unroofing process (Chauvet and Séranne, 1994).

#### 2.4.2 Middle Paleozoic Stability and Cooling event in the Permo-Carboniferous

In the late Carboniferous-early Permian, Laurussia was positioned at subtropical latitudes, stretching from 30° N to the equator. From early Carboniferous times, Laurussia became part of the Pangea supercontinent. During the late Carboniferous, the Barents Shelf was characterized by widespread deposition of shallow to deep water carbonates (Torsvik et al., 2002).

After a period of rapid cooling at the end of the Caledonian Orogeny, western Norway underwent a period of thermal stability between ~380-330 Ma or possibly between 380-300 Ma (Dunlap and Fossen, 1998). The evidences supporting the tectonic quiescence are among others the dating of K-feldspar using  $^{40}\text{Ar}/^{39}\text{Ar}$  (Dunlap and Fossen, 1998), the lack of evidence of metamorphism or deformation from field observations (Fossen, 1998), and the dating of fault rocks (Dunlap and Fossen (1998) and reference therein). A slightly different result was obtained by Eide et al. (1999) who also used  $^{40}\text{Ar}/^{39}\text{Ar}$  thermochronology from extensional detachment zones in western Norway (the Western Gneiss Region and the Nordfjord-Sogn Detachment Zone). Eide et al. (1999) proposed three domain changes in the late Paleozoic cooling rates: (1) slow cooling at 0.4<sup>0</sup>-2.2<sup>0</sup>C/m.yr from ca. 380-360 Ma, (2) rapid cooling at  $\geq 15^{\circ}\text{C}/\text{m.yr}$  in 360-340 Ma, and (3) slow cooling at 0.4<sup>0</sup>-1.7<sup>0</sup>C/m.yr after 340 Ma.

By the Permo-Carboniferous (300-240 Ma), magmatic and tectonic activities occurred and resulted in the development of the Oslo Rift (Sundvoll et al., 1990). The rift consists of two



graben segments: the southern Vestfold segment and the northern Akershus segment. The rift ends to the south close to the Tornquist zone. The general direction of tensional stress that developed in the Oslo Rift was E-W (Ramberg and Larsen, 1978). Buer (1990a) suggested that the stress field changed from an initially WSW-ENE to a WNW-ESE direction of the tensional axis. This is manifested in the field by deviated orientation of the grabens and blocks in this region, as seen at the Vestfold Graben which has a E-W axis direction, at the Bamble block which has a NE-SW structural trend, and at the Østfold block and Hedemark-Trysil region have a NNW-SSE trending axis direction (Ramberg et al., 1977). Russell and Smythe (1983) implied that the development of the grabens, blocks, and dikes within the Oslo Rift were related to oblique collision of plates in the Hercynian orogeny (collision of Laurussia and Gondwana to form Pangea) which was developing to the south.

The rifting event in the Oslo region also affected western Norway. Both Dunlap and Fossen (1998) and Eide et al. (1999) agreed about the occurrence of cooling events in Permo-Carboniferous times in this region, but different conclusions were drawn regarding its magnitude. Dunlap and Fossen (1998) suggested that cooling rates were in the range of 2<sup>0</sup>-5<sup>0</sup>C/Ma during the period 300-250 Ma. According to their interpretation, the timing of the onset of cooling corresponded to the magmatic event (300-240 Ma) in the Oslo Graben (Sundvoll et al., 1990). They also concluded that the cooling rate increased in the Permo-Carboniferous as a consequence of the rifting in southern Norway which generated a decrease of the base level and an increase in the rate of denudation.

A similar result was obtained by Rohrman et al. (1994) who applied fission track analysis on apatites, zircons and sphenes during their study of the Oslo Rift region. They suggested that the age of 270-260 Ma could reflect an event of syn-rift advective heating produced by large-scale batholith intrusions in the Oslo Rift region.

#### *2.4.3 Norway in Permian-Triassic times*

By the late Permian, the supercontinent Pangea was centered on the equator. The Barents Shelf region was located around 35<sup>0</sup>N during this time, whilst the North Sea was positioned in the subtropics. In the late Permian, probably most of all the continental blocks had been amalgamated; hence Pangea was at its largest. However, several rifting events occurred within the supercontinent and continental re-organization was continually initiated (Torsvik et al., 2002).

Rifting activity commenced in the Arctic-North Atlantic from Permian times onwards. In the earliest Triassic, rifting propagated into the North Sea and mainly centered in the Horda Platform (Fig.2.4) (Torsvik et al. 2002). The exact timing of this rifting event is poorly constrained, however Færseth et al. (1976) assumed that it occurred during the mid-Permian (ca. 260 Ma) when a swarm of basaltic dikes formed along the coastal area of the Sunnhorland, Sotra and Sunnfjord region. The emplacement of dikes was likely a result of upwelling and partial melting of the asthenosphere under the Horda Platform (Fossen and Dunlap, 1999). This rifting event also created new graben systems such as the Viking Graben (Fig. 2.4), the Horn Graben and the West Norway Through (Færseth et al., 1976).

Magmatism related with the rifting was studied by Færseth et al. (1976). They identified three episodes of alkaline dike intrusions derived from the Sunnhordland area using K-Ar dating on amphibole and whole rock samples. These episodes are 270 Ma; 220 Ma and 160 Ma respectively. Moreover, the paleomagnetic data from the dolerite dikes in Sunnfjord, western Norway also support the Permian extension event. Torsvik et al. (1997) produced a range of ages between 270-250 Ma from this area.

Fossen and Dunlap (1999) revised the data from the previous publications (i.e. Færseth et al., 1976; Løvlie and Mitchell, 1982; Torsvik et al., 1997) and produced new ages from K-Ar and  $^{40}\text{Ar}/^{39}\text{Ar}$ . From their work, they deduced that two pulses of magmatism occurred during the formation of the Permo-Triassic rifting based on K-Ar and  $^{40}\text{Ar}/^{39}\text{Ar}$  thermochronology of the alkaline dikes in Sunnhordland. The first event took place in early Permian times (260-250 Ma) and was followed by a second pulse represented by more extensive dike intrusions in the late Triassic (220 Ma). Additionally, thermal models using K-feldspar from the Sunnhordland area and the Jotun Nappe (see location in Fig. 2.2) by Dunlap and Fossen (1998) also revealed differential exhumation within the interval of 330-250 Ma.

Based on seismic interpretation across the Horda Platform, Færseth et.al (1995) revealed a 3-5 km throw of normal faults during the mid Permian-early Triassic. The master faults mostly have a typical N-S trend due to E-W extensional stress direction. The swarm of dikes in this area also has a similar N-S trending. Færseth et al. (1995) suggested that the N-S trend of Permo-Triassic faults was originated from rejuvenation of the pre-existing Precambrium N-S trending structures.

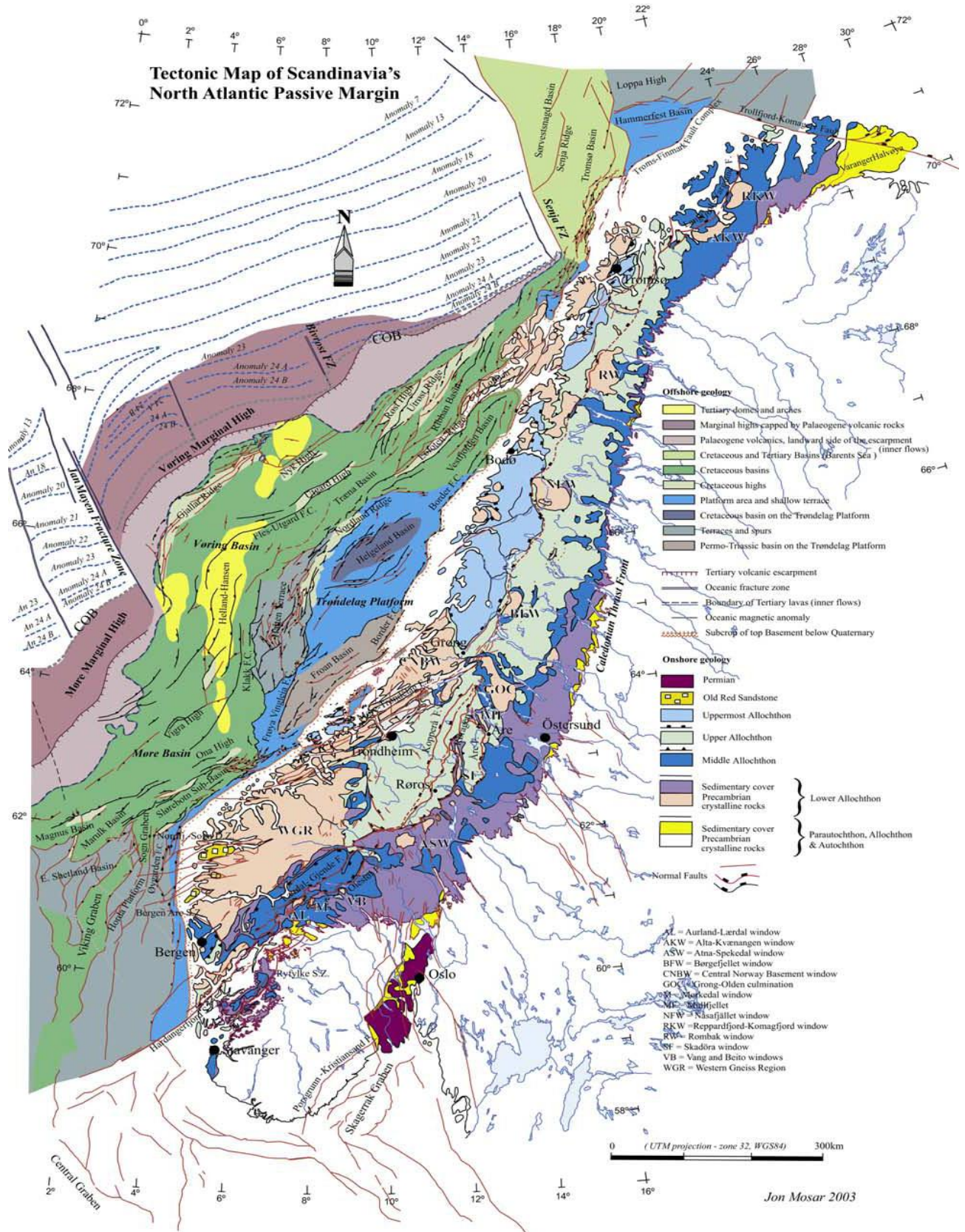
The rifting event in the North Sea was also recorded in the coastal area of western Norway by the formation of the main Lærdal-Gjende Fault (Fig. 2.4) and the subsidiary Olestøl fault. By

applying paleomagnetic analysis of cataclasite rocks in the Lærdal-Gjende Fault and its subsidiary, it was concluded that the age of fault breccias formation is in the range of 260-250 Ma (late Permian times) (Andersen et al., 1999).

By using paleomagnetic analysis, Torsvik et al. (1992) reported that the Dalsfjord fault in Sunnfjord, western Norway, underwent reactivation by generating brittle low angle normal faults (dips ranges of  $5^{\circ}$ - $15^{\circ}$ ). The faults evolved initially as ductile low angle normal faults in early Devonian times and were reactivated subsequently during the Permian (260-250 Ma) and Late Jurassic (150 Ma).

Fig. 2.4: The figure shows geological map of the Scandinavian North Atlantic passive margin. In the offshore, the different major tectonosedimentary events are indicated (modified from Blystad et al. (1995); Brekke et al. (1999); Gabrielsen et al. (1999), Mosar (2000); and Smethurst (2000)). The dip direction of the major normal faults in the offshore, such as in the Nyk High, the Utgard High, and the Gjallar Ridge are originated from interpretation deep seismic surveys by Osmundesen et al. (2002). The faults are differentiated by different color according to dip direction: red for west dipping and black for east dipping. The onshore tectonostratigraphic map has been modified from the Scandinavian Caledonides tectonostratigraphic map by Gee et al. (1985). Offshore magnetic anomalies are referring to Skogseid et al. (2000). This figure was taken from Mosar (2003).





#### 2.4.4 Norway in Jurassic times

By mid Jurassic, the supercontinent Pangea had started to break up. The two major global events that led to break up were sea floor spreading in the Central Atlantic and Gulf of Mexico and rifting of the southern elements of Pangea between Africa and the joint Antarctica-Australia-Madagascar-India landmasses (Torsvik et al., 2002).

During about 170-160 Ma (mid Jurassic), a large volcanic centre developed at the triple junction between the Viking, Central Graben and Moray Firth Graben (see location in Fig. 2.4). However, the dome had a short lifespan. In the early Late Jurassic the dome foundered and clastic supply to adjacent basins was reduced (Ziegler, 1992; Torsvik et al., 2002).

Maximum rifting activities took place in the entire Arctic-North Atlantic rift system in the Jurassic-Cretaceous. The rifting event affected mainly the formation of the Viking, Central and Moray Firth Grabens. Rapid increase of crustal stretching largely occurred in the Viking Graben which was represented by uplift of footwall blocks above the erosional base level. An accelerated crustal stretching caused rapid subsidence and about 1000 meter pelagic shales accumulated and filled the Viking Graben. Seismic interpretation indicates that the net crustal extension in the Viking Graben during Jurassic-Cretaceous times reached 19 km (Ziegler, 1991).

The Jurassic extension in the Viking Graben basically had a similar magnitude of stretching, ( $\beta$ ) 1.4-1.5, as the Permo-Triassic extension. However, there is a difference in the distribution of stretching as well as the structural expression. The main Permo-Triassic extension generated N-S trending structures, whilst the Jurassic extension was represented by those of NNE-SSW direction (Fig. 2.5) (Færseth, 1996).

In the Norwegian mainland, the youngest dikes in the Sunnhordland region yield a mean age of 164 Ma. This age corresponds to the volcanic activity in the North Sea (Færseth et al., 1976). Furthermore, the AFT age data from southern Norway (Eidfjord, Jotunheimen) indicate a cooling event initiated at ~160 Ma, which was coincident with repeated rifting phases in the North Sea (Rohrman et al., 1995). The AFT ages and thermal model obtained from Jurassic sediments in the Horda Platform and Utsira High also imply that the areas experienced rapid cooling during the late Triassic-early Jurassic (Rohrman et al. 1996).

#### 2.4.5 Norway in the Cretaceous

On a global scale, Asian landmasses ultimately docked with Europe to form Laurasia in the early Cretaceous. At the same time, the Central Atlantic system initiated to propagate northwards and resulted in the opening of the Bay of Biscay. In the late Cretaceous, the Central Atlantic had connected with the South Atlantic. In this period, North America, Eurasia, and Greenland continuously drifted northwestward.

The Cretaceous extension in NW Europe is characterized by NW-SE extension, which was rotated and originated from a NE-SW extension in the late Jurassic (Fig. 2.5) (Torsvik et al. 2002). In the Norway region, this extension phase is well documented in the Vøring Basin (see location in Fig. 2.4) (Doré et al., 1999). The onset of rifting in this basin occurred in the early Cenomanian-early Turonian, i.e. early of Late Cretaceous times (Bjørnseth et al., 1997; Brekke, 2000), and was marked by the formation of large scale normal faults on the eastern flank of the basin (Ren et al., 2003).

At the Gjallar Ridge, the rifting also elevated northern margins of these pre-existing rifts (see location in Fig. 2.4). The southern culmination of this ridge was eroded deeply, whilst the northern high was capped by low angle normal faults. The rifting is interpreted as a series of extensional core complexes governed by heating from magmatic underplating related to the Iceland plume in Paleocene-Eocene times (Lundin and Doré, 1997; Doré et al., 1999). However, Brekke (2000) suggested that the relative uplift in the Gjallar Ridge was a response during the thermal cooling phase of the late Jurassic-early Cretaceous rifting.

Ren et al. (2003) suggested that the rifting that occurred in Cretaceous times can be characterized by (1) formation of large scale normal faults during the early rift phase at about 81-65 Ma and, (2) continued extension, regional uplift, intrusive igneous activity and erosion in the late rift phase at 65-55 Ma. The latter phase was also marked by a change from brittle to ductile extensional deformation.



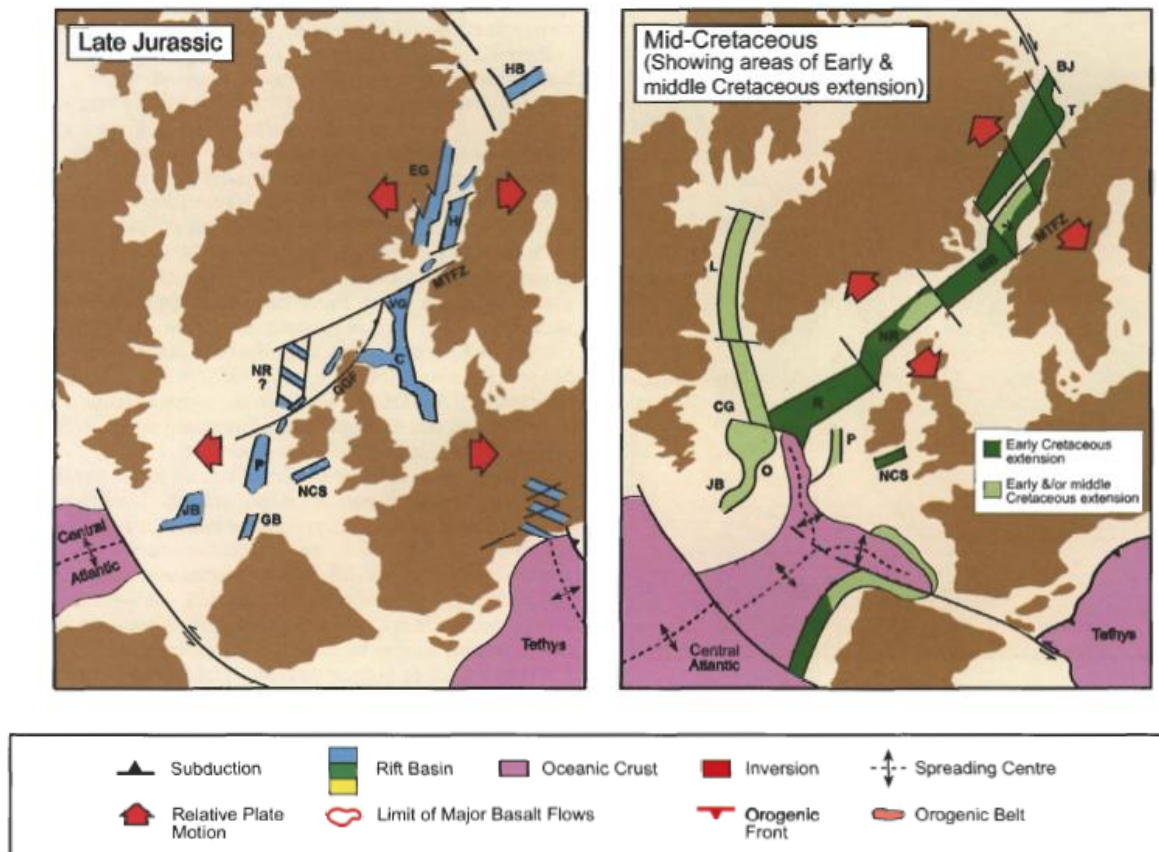


Fig. 2.5: Map shows plate reconstruction in the late Jurassic and mid-Cretaceous (Doré et al., 1999). The figure indicates relative plate motion, contemporaneous rifts and tectonosedimentary events. The abbreviations are as follows: HB = Hammerfest Basin, EG = East Greenland Rift, MTFZ = Møre-Trøndelag Fault Zone, VG = Viking Graben, C = Central Graben, GGF = Great Glen Fault, NR = Northern Rockall Through, P = Porcupine Basin, NCS = North Celtic Sea Basin, GB = Galicia Bank Basin, JB = Jeanne D'Arc Basin, MB = Møre Basin, BJ = Bjørnøya Basin, T = Tromsø Basin, V = Vestfjorden Basin, R = Rockall Through, L = Labrador Sea, O = Orphan Basin.

#### 2.4.6 *Norway during the Cenozoic*

Sea floor spreading in the NE Atlantic between Greenland and Europe began at ca. 54 Ma. This rift episode led to the connection between the Atlantic and Arctic Oceans, and it also marked the break-up of the supercontinent Pangea (Torsvik et al., 2002).

Rifting events in the Paleocene were significantly different to the ones that occurred in the Cretaceous. In contrast to the typical non-volcanic passive margin in the Cretaceous, the Paleocene rifting was a classic volcanic passive margin. The uplift event in this epoch was also signified by the presence of the Iceland plume, which in turn resulted in highly clastic incursions from the easterly continent into the Vøring and Møre Basins, and probably from marginal highs to the west (White and Lovell, 1997; Doré et al., 1999).

The existence of the plume is generally believed have been a result of migration of the plume-generated mantle which melted into the thinned axis of incipient opening (Eldholm et al., 1989). A likely product of this activity is the development of seamounts in the Rockall Trough (see location in Fig. 2.6), where basalts in this area have been dated using K-Ar resulted of 70-65 Ma (Late Cretaceous times) (Hitchen and Ritchie, 1993).

A wide range of magmatism reached approximately 2200 km in diameter and hence generated the North Atlantic Igneous Province (NAIP). The NAIP is also characterized by underplating beneath the crust, sills, dikes, and tuffs extrusion. Saunders et al. (1997) constrained the time of magmatism between 62-54 Ma (early Paleocene-early Eocene times).

Elevated asthenospheric temperatures and a high rate of Paleocene lithospheric extension governed the vast generation of melts in the area. However, the structural elements related to the Paleocene rifting are less significant in the Norwegian Sea. It has been suggested that the lack of extensional evidence is related to masking of basalt flows in this area (Torsvik et al., 2002).

The break-up phase in the Norwegian-Greenland Sea was recorded at about 55-52 Ma or 53 Ma (Doré et al., 1999), yet the most intense volcanism only happened around 1-1.5 Ma after the break-up (Eldholm et al., 2002). This event was marked by regional volcanism which produced the Vøring Marginal High (see location in Fig. 2.5) (Ren et al., 2003).

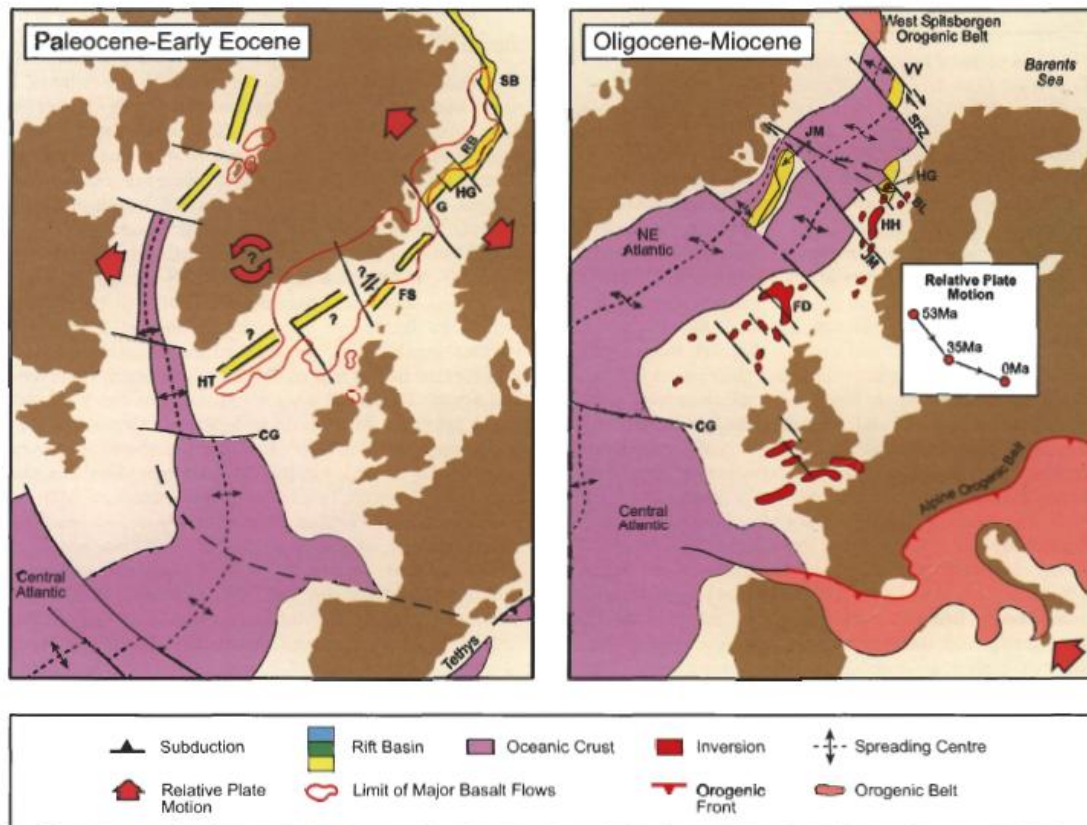
In the early Eocene, a new compressive regime became dominant. The compression was widely distributed along the Atlantic margin and generated plenty of inversion structures especially observed in the Faeroe-Rockall area and the Norwegian Sea. The general stress pattern has a NW-SE compression direction (Fig. 2.7) which is also consistent with the relative motion of Europe and Africa, and hence with the Alpine closed at the same time (Müller and Roest, 1992). Brekke and Riis (1987) inferred that the Norwegian inversion at approximately 35 Ma (upper Eocene) was attributed to the plate reorganization due to a change in relative plate motion between Greenland and NW Europe to an ESE direction.

In the Norwegian Sea, the most common inversion features are elongate domes such as the Helland Hansen Arch (see location in Fig. 2.7), the Ormen Lange Dome which was deformed in the late Eocene-early Oligocene, and the Naglar Dome at northernmost which was deformed in early-middle Miocene times. These evidences suggest that the inversion system is younging northward (Doré et al., 1999).

A local renewed extension occurred in the North Atlantic margin during the Oligocene-Miocene (Fig. 2.7). The extension culminated by the separation of the Jan Mayen microcontinent (see location in Fig. 2.7) and SE Greenland and the extinction of the Ægir Ridge at 25 Ma (Kuvaas and Kodaira, 1997). The extension was observed in the western of Barents Sea where the development of Knipovitch Ridge started at 35-20 Ma (Faleide et al., 1993). Doré et al. (1999) identified that the extension propagated to the northern Vøring Basin by the presence of Oligocen-Miocene sills onlapping onto a Paleocene unconformity.

Regionally, by about 20 Ma (early Miocene times), spreading between Greenland and North America had ceased. There was also a change of drifting direction of Eurasia, from a predominantly NW direction during late Cretaceous times to a NE direction during the early Miocene, which coincided with the plate directions of both Africa and India. During the middle Miocene, Mid Norway was located at around 65<sup>0</sup>N (Torsvik et al., 2002).

Fig. 2.7: Plate reconstruction in the Paleocene until Miocene. The figure indicates relative plate motion, contemporaneous rifts and tectonosedimentary events. The abbreviations are as follows: SB = Sørvestnaget Basin, RB = Røst Basin, HG = Hel Graben, G = Gjallar Ridge, FS = Faeroe-Shetland Basin, HT = Hatton Through, VV = Vestbakken Volcanic Province, SFZ = Senja Fracture Zone, BL = Bivrost Lineament, JM = Jan Mayen, HH = Helland Hansen Arch, FD = Faeroes Dome. This figure is modified from Doré et al. (1999).



The regional uplift is the most important event during Neogene times. The uplift was recognized almost at the whole Norwegian mainland by the uprising of Cretaceous and Cenozoic units and the truncation of units close to the Norwegian coast (Doré et al., 1999). Many workers agree that the uplift occurred in several phases during the Cenozoic, yet the greatest uplift and erosion was in the Plio-Pleistocene associated with glaciations and deglaciations in the last 2.5 Ma (Solheim et al., 1996).

When uplift and erosion occurred in the Barents Shelf and the British Isles at about 2.7 Ma, the North Sea Basins underwent tectonic quiescence which was marked by sediment deposition derived mainly from the British Isles. During the Pliocene and Pleistocene, sediment thickness attained 500-1000 meters in the central North Sea (Ziegler, 1992). Up to 1000 meters of surface uplift has been reported from the Norwegian mainland and 3000 meters have been suggested for the Barents Shelf (Torsvik et al., 2002). This uplift occurred as an of isostatic response to lithospheric unloading. At present the Scandinavian landmasses continue to undergo post glacial uplift and erosion with a rate as much as 1-5 cm/yr (Torsvik et al., 2002).

Today Eurasia and Africa are moving northeastward at speeds of 2.3 and 3.0 cm/year respectively. Half-spreading velocities between Greenland and Eurasia have been established at approximately 1 cm/yr since the late Oligocene (30 Ma) until today, although the speed of individual plates has been slightly different (Torsvik et al., 2002).

## 2.5 Geological Framework of the Present Study

The Hardangerfjord Shear Zone (HSZ) is one of the most important structures in the south of Norway which influenced the development of the North Sea rift system. The total length of this shear zone is ~ 350 km and it can be traced from the mouth of Bømlafjord toward the northeast. It passes through Aurland, along the NE side of Jotunheimen, and along the NE margin of the Jotun Nappe (Fig. 2.2). In the Hardangerfjord, this shear zone is best exposed in the area to the northeast of the Bømlafjord (Fig. 2.8). In the area between Aurland and Lærdal, the HSZ dies out and then re-appears as a more brittle fault system in the Folgefonna area, where it forms a segment of the Lærdal-Gjende Fault System. Thus, an area between Folgefonna and Aurland seems to link the two different faults systems (Fossen and Hurich, 2005).

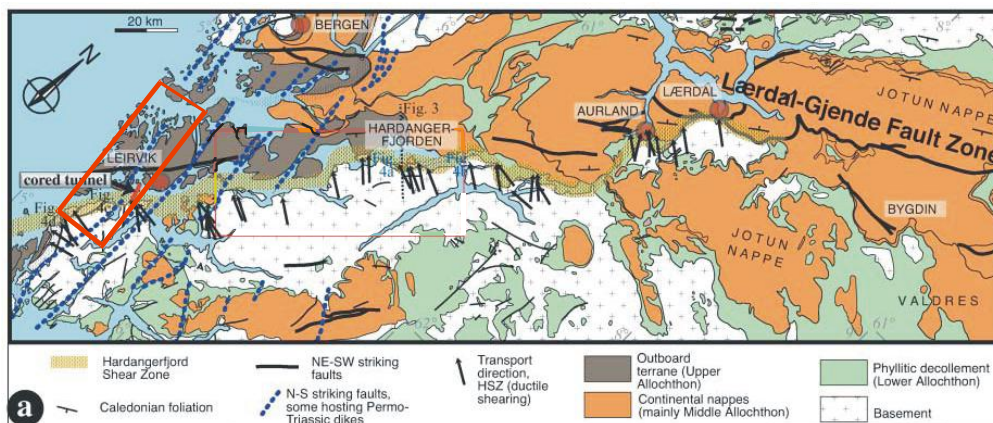


Fig. 2.8: Geological map of the Hardangerfjord area. The map shows the NE ductile extension of the HSZ which stretches out from the mouth of the Bømlafjord and re-appears as a brittle extension of the Lærdal-Gjende Fault System in the area between Aurland and Lærdal (Fossen and Hurich, 2005).

The HSZ is characterized by several features: (1) the décollement zone (sheared phyllites) and the underlying basement exhibit ductile deformation, with NW dipping mylonitic fabrics and top-to-NW sense of shear, (2) the Jotun Nappe and the décollement zone were folded by predominantly plastic deformation. The monoclinal syncline fold structure and the whole Caledonian nappe unit are only preserved in the hanging wall. The syncline folds are draped



in the hanging wall and relate to the formation of the normal fault, or a product of reactivation of the basement faults. Several folds in the hanging wall of the HSZ have subhorizontal axial surfaces and hinge lines parallel to the shear zone (Fossen and Hurich, 2005).

Seismic reflection profiles which were taken from the area of the western Norwegian coastline indicate a presence of Devonian deposition in the hanging wall. The other evidence is derived from boreholes drilled on the southern Viking Graben, north of the HSZ, which exhibited more than 400 meter of Devonian deposits (Færseth et al., 1995). The clastic sediment loading in the hanging wall is believed to have caused uplift in the footwall as described by Fossen and Hurich (2005).

The ductile shearing can be identified in both the basement and the allochthonous units. In the basement of the HSZ, middle greenschist facies metamorphic conditions are predominant. Garnet and feldspar are commonly found as porphyroclasts and exhibit top-to-NW fabrics. The thickness of the shear zone in the basement has been estimated to 5-6 km, based on onshore mapping, core samples and map reconstruction of the distance between the hinge points of the monoclinical structure (Fossen and Hurich, 2005).

In the allochthonous units, evidences of down-to-NW movement are prominently observed, such as microfolds, shear bands, S-C structures and asymmetric boudins. The average dip contact of the décollement zone and the basement of the HSZ are around  $22^{\circ}$ , yet slightly steeper in the mainland area (Fossen and Hurich, 2005).

Fossen and Hurich (2005) suggested that the throw of the HSZ is about 5 km. this estimation was obtained from a reconstruction of geological profiles across the Hardangerfjord area. A similar result was obtained by Milnes et al. (1997) who proposed a throw of about 6-7 km in the Lærdal area. The estimation difference likely arises due to the depth measurement of the uppermost basement in the hanging wall.

Regional observation shows that the HSZ has an average NE-SW trend with a dip direction towards the NW. This orientation corresponds to a NW-SE extension. However, observations at smaller scale reveal an irregular pattern, where several segments have very different trends. This situation pronouncedly appears in the Varaldsøy area, where two NE trending segments are connected with a segment with NNW direction (Fig. 2.9). The fragmented pattern is probably a result of deformation in the mechanically heterogeneous basement and is influenced by a pre-existing Proterozoic shear zone in the footwall (Fossen and Hurich, 2005).



Fig. 2.9: The relief map shows an abrupt change of the extensional HSZ direction in Varaldsøy. The HSZ is indicated by a red line. Allochthonous units located in the area north of the HSZ, are indicated by greenish color. Basement rocks south of the HSZ are shown by light brown color (Fossen and Hurich, 2005)

During the Caledonian Orogeny, the shear zone was activated after a period of northwestward transport (Mode I) (Fig. 2.3). The shearing was initiated during the Mode I extension, which affected and activated the décollement. During the Mode II extension, the décollement was inactive due to accumulated offset on the HSZ which also folded both the décollement and the overlying Caledonian nappes.

Ductile shearing in the basement caused brittle faulting in the overlying nappes. The brittle deformation that formed northeast of the HSZ is known as the Lærdal-Gjende fault system, and its development may be considered at a late stage of the HSZ formation. Rb/Sr dating from fractures in the Lærdal-Gjende fault system reveals an age of ~367 Ma (Schärer, 1980). It is then inferred that this fault system formed during Devonian times. However, evidences for major the brittle structures cannot be found along the HSZ since they die out between Aurland and the Hardangerfjord (Fossen and Hurich, 2005).

In addition to faults and fractures with NE-SW trending structures, the N-S to NNW-SSE trend is pronounced in the hanging wall of the HSZ. The Permo-Triassic alkaline dike swarms intruded these faults but not the NE-SW trending faults. Therefore, it can be concluded that the faults post-date the main NE-SW structures and pre-date the alkaline dikes (Fossen and Hurich, 2005). Færseth et al. (1976) and Løvlie and Mitchell (1982) interpreted that the intrusion of dikes in the Sunnhordland and Sotra regions occurred around 280-260 Ma (Permian times) based on the K-Ar dating method. Fossen and Dunlap (1999) who applied

$^{40}\text{Ar}/^{39}\text{Ar}$  dating on amphiboles from a similar area yielded ages around 220 Ma (Triassic). Another study from Færseth et al. (1976) also demonstrated a similar age of 220 Ma. Both the Permian and Triassic dike intrusions are correlated with rifting activities which were centered in the Horda Platform (Torsvik et al., 2002; Fossen and Dunlap, 1999).

The regional map of the uppermost basement surface (Fig. 2.10) shows a dome-shaped geometry, which is attributed to a Tertiary uplift event (Rohrman et al., 1995). The basement surface has a general elevation of 1000 m above sea level southeast of the HSZ. However, the surface elevation changes considerably close to the shear zone of about 1600 m. Reconstruction of the profile across the HSZ shows footwall uplift of about 800-1000 m (Fig. 2.10). The similar trend of these features is also observed in the area 40-50 km southeast of the HSZ which also has a parallel trend to the shear zone. In this area, closely spaced extensional shear zones and faults which are found are related to the HSZ.

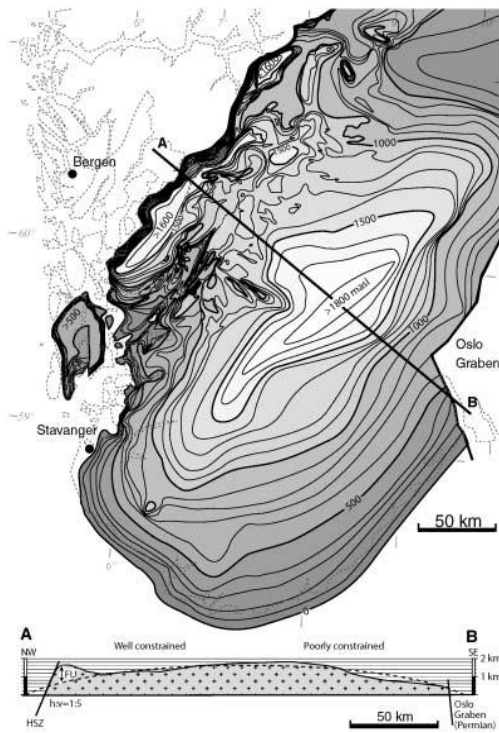


Fig. 2.10: Regional map shows the uppermost basement of southern Norway. The sub-Cambrian basement surface reaches heights of more than 1800 m a.s.l. in the area between the HSZ in northeast and the Oslo Graben in southeast. The profile below the map, displays the deviation from the general trend of the dome shape near the HSZ (Fossen and Hurich, 2005).

FU = Footwall Uplift; HSZ = Hardangerfjord Shear Zone

The reactivation of the HSZ will be identified using low temperature-thermochronological method, apatite fission track. The method will be discussed in the apatite fission track methodology chapter.

### 3. APATITE FISSION TRACK METHODOLOGY

#### 3.1 General

Every solids material, once it is penetrated by nuclear particles, will obtain linear trails of disrupted atom which also reflect damage on the atomic scale. Fission tracks are such damage feature. The emerged features are produced by spontaneous fission of the  $^{238}\text{U}$  (Gallagher et al., 1998).

In general, fission track dating is similar to the other dating methods that rely on the same equation of radioactive decay, i.e. estimating abundance both of the parent and daughter isotope. In fission track analysis, it corresponds to the number of  $^{238}\text{U}$  atom and the number of spontaneous tracks per unit volume. In order to obtain the number of spontaneous track, we simply count the number of spontaneous fission tracks on a given surface of a mineral grain. Meanwhile, the abundance of  $^{238}\text{U}$  can be determined by irradiating the samples with low energy thermal neutron in order to induce fission  $^{235}\text{U}$ . By controlling the thermal neutron flux, we obtain the number of 'induced tracks' which also signified the abundance of  $^{235}\text{U}$ . Since the ratio of the  $^{235}\text{U}/^{238}\text{U}$  is constant, hence we are able to estimate the abundance of  $^{238}\text{U}$  (Gallagher et al., 1998).

Fission tracks are metastable features which mean that the tracks can fade or anneal. The annealing tracks can lead the tracks to shorten. Therefore, length track distribution is fundamental parameter in the fission track analysis. Several factors that influence annealing are temperature, time, pressure, chemical composition and ionizing radiation (Fleischer et al., 1965b). However, temperature combined with time is the most contributing factor for the annealing. Therefore, tracks length distributions contain information of the thermal history of the analyzed samples (Gallagher et al., 1998).

Recently, applications using fission track analysis have widely known to solve geological problem. This thermochronology method is rather exceptional than others, whereas the temperature dependence of fission tracks annealing provides information of the thermal history. Various geological problems can be unraveled by this method such as the thermal history of sedimentary basins, sedimentary provenance, structural evolution of orogens, continental margin development, and long-term denudation on continents (Gallagher et al. 1998).

### 3.2 Apatite Properties

Apatite commonly appears as anhedral or euhedral accessory mineral in igneous rocks, detrital grains in sedimentary rocks, and as primary mineral or porphyroblasts in metamorphic rocks. In the volume of total rocks, the amount of apatite is only 1% or less. Apatite crystals commonly have small sized grains, about less than 300  $\mu\text{m}$  (Donelick et al., 2005). For this study, apatite which has a size larger than 100  $\mu\text{m}$  is preferable.

Apatite is phosphorus-bearing mineral which has three anions of fluoride, chloride and hydroxide ( $\text{F}^{-1}$ ,  $\text{Cl}^{-1}$ , and  $\text{OH}^{-1}$ ). The chemical formula for apatite is written  $\text{Ca}_5(\text{PO}_4)_3[\text{F},\text{Cl},\text{OH}]$ . The three of anions substitute one another and forms various end members of different composition such as fluorapatite, chlorapatite, and hydroxyapatite. Though, additional chemical elements might be substituted by other anions, such as Mn, Sr, Fe, Na and rare earth-elements (Deer et al., 1969). U and Th commonly present in apatite because of their small ionic radius cation are incompatible to other silicate minerals. Therefore, apatite is good for analysis fission track and U-Th/He analysis. Usually, the concentration of natural uranium in apatite ranges from 1-200 ppm (Donelick et al., 2005).

Apatite is a member of the  $6/m$  hexagonal dipyramidal crystal class (Deer et al., 1969), yet another rare of chlor-apatite has monoclinic crystal system (Hughes et. al., 1989). The typical apatite crystal present in the igneous rocks is prismatic. Even though, it has no strong cleavage, apatite shows a weak plane perpendicular of the crystallographic  $c$ -axis (Donelick et al., 2005).

Apatite has a density of 3.15-3.20  $\text{g}/\text{cm}^3$  which is higher than the average density of the other rock forming minerals, which are around 2.90  $\text{g}/\text{cm}^3$ .

In this study, apatite was used for analysis for several reasons: (1) its presence is ubiquitous in most of crustal rocks; (2) its physical properties; (3) its major and minor element chemistries; (4) its content of uranium and thorium; (5) its ability to retain fission tracks in the geological environment; (6) its ease for experimentalist to mimic the geological environment using laboratory analogues (Donelick et al., 2005).

### 3.3 Track Formation Process and Theory

When a heavy nuclide was charged in a solid medium at a high velocity, it will interact with the constituents of the solid (atoms and electrons), which will cause gradual loss of its kinetic energy. The rate of total energy loss was considered to be critical in track formation which means that no tracks could be formed in the solid if the minimum of total energy loss is not fulfilled. However from later experiments (Fleischer et al., 1975), it was inferred that the total energy loss is not a factor of tracks existence, but the number of ions formed per unit distance along the pathway of the moving particles.

At present, the track formation theory proposed by Fleischer and coworkers (Fleischer et al., 1965a) had been widely accepted. Their theory is called ‘ion explosion spike’ theory. According to the theory, the tracks formation can be divided by three stages (Fig. 3.1): 1) the heavy highly charged particles in the solid induces electronic interactions which produce a burst of ionization and a group of positive ions in the lattice; 2) the surrounding ions then expel each other into interstitial positions and finally it forms a series of vacancies; 3) by elastic relaxation, the local lattice then spread more widely. In the last stage, latent tracks are emerged and enable to be observed by electron microscope.

In nature, spontaneous fission only occurs on very heavy nuclides of atomic number higher than 90 and atomic mass bigger than 230 which belong to the actinide series (Th, Pa, U, Np, etc.). However, only  $^{232}\text{Th}$  and both of U isotopes ( $^{235}\text{U}$  and  $^{238}\text{U}$ ) have measurable concentration in nature. From the three of the isotopes above, only  $^{238}\text{U}$  which has a significant abundance and shorter spontaneous half life ( $8.2 \times 10^{15}$  years). In nature, sufficient uranium can be found in apatite, zircon, titanite and natural glasses (Wagner and Van den Haute, 1992).

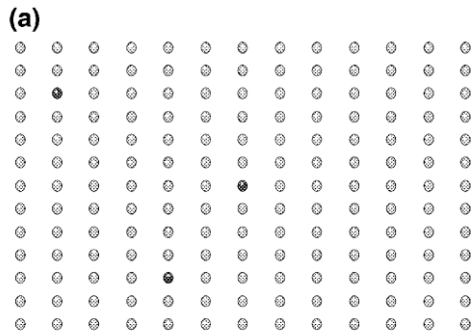
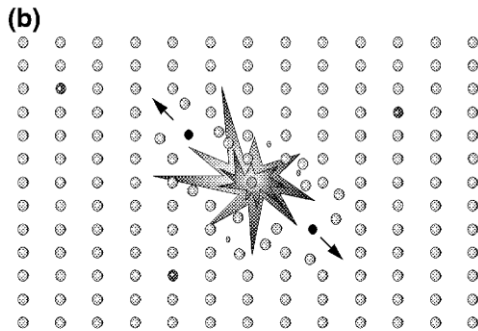
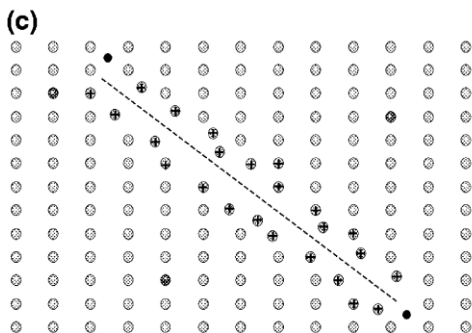


Figure 3.1 Cartoon illustrates formation and process charged particle tracks registered in a solid by the ion explosion spike model (Gallagher et al. 1998 after Fleischer et al. 1965a)

- Dark circles are traces of  $^{238}\text{U}$  which present in the crustal lattice. They are basically unstable.



- Spontaneous fission of  $^{238}\text{U}$  produces two charged heavy particles which have mass number in the ranges 85-105 and the higher one in the range 130-150. The fission also releases energy about 200 MeV. Those highly charged particles recoil due to Coulomb repulsion and interact with other atoms in the lattice caused by ionization.



- The fission particles slow down since they capture electrons and the particles' energy decreases. The damage trail left due to charge of highly particles is called a fission track.

In the fission track method, the parent of  $^{238}\text{U}$  decays not only by spontaneous fission, but also by eight of  $\alpha$ -emission ( $^4\text{He}$ ). This decay occurs  $2 \times 10^6$  times more frequently than the one from spontaneous fission (Tagami and O'Sullivan, 2005). Therefore, the total decay for the  $^{238}\text{U}$  is the decay constant for  $\alpha$ -emission and the one for spontaneous fission (see the age equation in subchapter 3.7).

In order to make the method useful and robust, there must be an adequate concentration of  $^{238}\text{U}$  to produce a detectable amount of fission events. However, too high concentration of  $^{238}\text{U}$  can result in too much fission, which makes the tracks hard to distinguish. Commonly, an appropriate range of uranium concentration for common minerals used, such as apatite, sphene and zircon is about 1-1000 ppm (Gallagher et al., 1998).

### 3.4 Track Exposure

As it has been explain above that the latent tracks are only able to be observed by transmission electron microscopy (TEM) or atomic force microscopy (AFM). In order to reveal the damaged trails under a normal optical microscope, the track are getting etched. The etching technique is a destructive method which attacks and removes material along the track itself (Wagner and Van den Haute, 1992).

Basically, the etching technique applies a suitable chemical reagent to immerse the mineral or glass. The reagent enables the tracks to become enlarged and hence visible under an optical microscope (Wagner and Van den Haute, 1992).

It is noteworthy that the etchant is not capable to reveal the whole range of a fission fragment, which means that the etchable tracks are shorter than the latent tracks. Secondly, etching only enables to reveal a part of the latent tracks that cross a glass surface. The most important is that crystals behave very different than glass with respect to etching, depending upon their crystallographic orientation and also upon the orientation of the tracks. Therefore, tracks with different orientation and/or different crystallographic symmetry will be revealed at different rates of etching (Wagner and Van den Haute, 1992).

The evolution of track density regarding to etching time can be divided into three phases: 1) an initial phase of zero density when the tracks are still under the limit of visibility; 2) phase of rapid increase of revelation of surface tracks (underetching phase); 3) the last phase is the overetching phase which is signified by much slower furrow. In this phase, the confined tracks (tracks located in the interior of the crystal) will be revealed. It however does not imply that prolonging etching time will increase the tracks density, because further deepening of the bottom of tracks is relatively slow, often absent and eventually it will be digested by removal of material at the surface. In addition, tracks will show flat-bottom when their end is reached and completely lost their channel-like parts. Tracks in this condition can hardly be recognized (Wagner and Van den Haute, 1992).

The etching process is very critical for AFT analysis. Hence, an optimal degree of track etching has to be defined. Gleadow and Lovering (1977) suggest that an optimum etching can be reached until the beginning of the third phase but not very much further.

The process of track exposure is also related to the chemical properties of the etchant and the mineral. For a given crystal surface, some reagents behave more anisotropically than others.



Additionally, a small change of concentration in the etchant may have an influence on the characteristic of the etched tracks. In fission track dating, etchants which can isotropically reveal the tracks are preferred (Wagner and Van den Haute, 1992).

### **3.5 Fading and Annealing of Fission Tracks**

Tracks are metastable, which have ability to shorten. Mostly, tracks shortening attributes from elevated temperatures. Here, track length is a parameter to measure the shortening.

#### *3.5.1 Fission Track Length*

Fission tracks derived both from glass and crystals are influenced by environmental conditions. This can be reflected in their size of tracks. In glass, the diameter of the tracks (pitch diameter) has been used as a source to understand these effects. Meanwhile, the crystals use track lengths as a parameter. The distribution of track length is measured from so called confined tracks which provide good tool to reveal thermal history information (Wagner and Van den Haute, 1992).

Two types of tracks are considered for track length measurement. The first type are surface tracks (projected tracks) i.e. tracks which cut the mineral surface; the second type are so called confined tracks which are located in the interior of the crystals, but have been revealed by the etchant because they intersect cleavage planes at the crystal surface or through the surface tracks (Fig. 3.2). Confined tracks are also called as TINTs (Track In Tracks) or TINCLEs (Tracks IN CLEavage) (Bhandari et al., 1971). In fission track dating technique, confined tracks are used as a source of information. Commonly, only confined tracks which are parallel (or nearly horizontal  $\sim 15^\circ$ ) to the c-axis will be selected. The surface tracks which intersect directly the surface are too difficult to be measured, because in spite of the tracks have to be projected vertically, the amount of the truncated tracks are unknown (Gallagher et al., 1992).

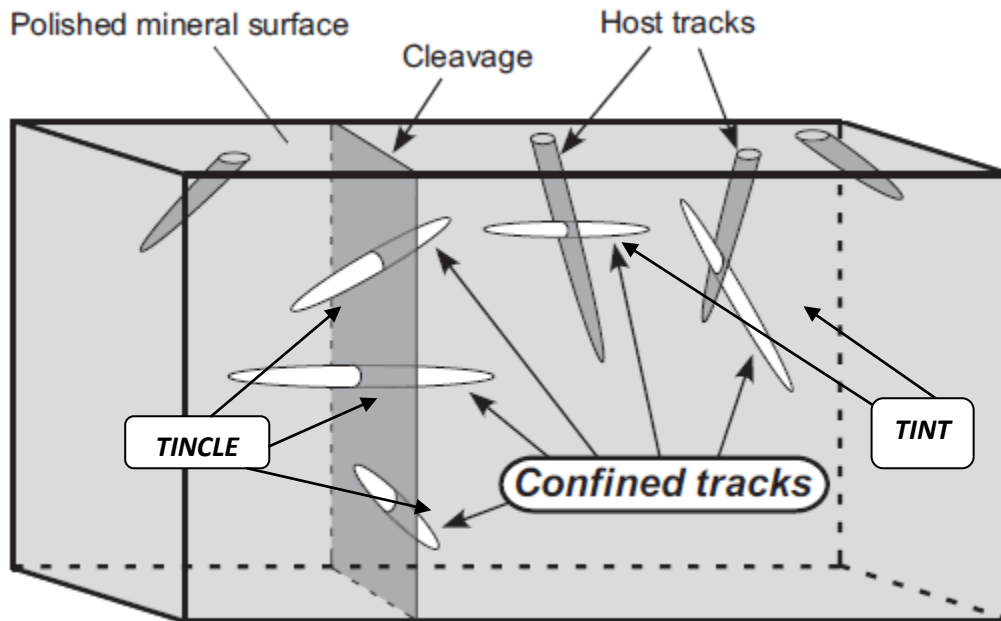


Figure 3.2 Illustration of an etched mineral that exposes confined tracks. The tracks are revealed by etchant through cleavages i.e. Tracks-IN-CLEavage (TINCLEs) and host tracks or projected tracks i.e. Track-IN-Tracks (TINTs). (Tagami and O’Sullivan, 2005 after Bhandari et al., 1971)

A collected sampling bias cannot be avoided, because the probability of longer tracks intersect the cracks or cleavage planes is higher than the shorter ones. Therefore, the amount of shorter tracks is always underestimated compared to the amount of longer tracks. Thus, as the method is determined from counting the number of tracks, it will yield an older age. In order to retrieve the correct measurement, information from the surface tracks (i.e. projected length measurement) is needed. However, it is rarely used due to the complicated mathematic formula and impractical. To do so, in practice, ideally the length tracks distribution of confined tracks has to exhibit a shape which is close to a normal distribution with an average length about 16  $\mu\text{m}$  and a standard deviation of 0.8-1  $\mu\text{m}$  (Gleadow et al., 1986).

### 3.5.2 *Fission Track Annealing*

Fission tracks are influenced by several geological factors, namely time, temperature, shock wave pressures, intergranular solutions and ionizing radiation. From all the factors above, temperature is the most dominant parameter affecting stability of the tracks (Wagner and Van den Haute, 1992). Fleischer et al. (1964b; 1965b) and Maurette et al. (1964) investigated the effect of high temperature on tracks in mica, olivine, zircon and tektite which became shorten and discontinuous proportional with elevated temperature. This phenomenon is known as fading. The fading event is not only signified by reduction of the etchable length but also by

etching rate and decreasing of the areal density of the tracks (Wagner and Van den Haute, 1992).

The track fading phenomenon actually breaks the most important prerequisite of a radiometric system, because the system is still *open* of the radiogenic daughter product. As a result, the reduction or loss of tracks tends to lower the apparent fission track ages. On the other hand, it is the advantage of this method to reveal the thermal history of the rocks (Wagner and Van den Haute, 1992).

It has been explained above that many factors influence the tracks fading. Nevertheless, temperature plays the most important role influencing the tracks stability. The track fading due to temperature is known annealing. The term of annealing refers both to the time and temperature. The reduction of track lengths and their diameter during annealing is of important because it forms a basis of the temperature-time (T-t) path from fission track records.

Etch pit diameters are used as a parameter to detect the degree of annealing in glasses. The grade of annealing in crystals are measured based upon the mean track length and the track density. In general the parameter of mean track length is used instead of the track density reduction, because the reduction of the mean track length has a direct consequence on the decreasing of the track density (Wagner and Van den Haute, 1992).

The causes of the actual annealing process are not yet fully understood. Apart of high temperature depending, other factors that influence the annealing kinetic are the crystallographic orientation, the chemical composition of apatite grains, etching characteristic of the apatite (Carlson et al., 1999), and confining pressure (Wendt et al., 2002). Measurable parameters which correlated to the fission track annealing kinetic are referred to as kinetic annealing parameters. These parameters among others are:  $D_{par}$  or parallel etch pit diameter, chlorine content (Cl), hydroxyl content (OH), infra-red microspectroscopy (IR) which is a function of absorption Cl and F, and  $\alpha$ -particle damage. From all those parameters, only two of them i.e.  $D_{par}$  and Cl content are most commonly applied (Donelick et al., 2005). In the present study,  $D_{par}$  was measured as a kinetic annealing parameter.

$D_{par}$  is an arithmetic mean of the fission track etch figure diameter (Donelick et al., 2005). Diameter of the  $D_{par}$  reaches maximum size when the etched track openings are oriented parallel to the crystallographic *c*-axis and it is measured between its two tips. There is broadly

misconception among thermochronological workers if the  $D_{par}$  parameter is a proxy of Cl content. Although, it is correct that the  $D_{par}$  is positively correlated to Cl and OH content and negatively correlated to F content (Donelick, 1993), but it has to be considered as an individual parameter which is independent to any chemical composition or other variables (Carlson et al., 1999).

Observations of  $D_{par}$  parameter from apatite grains shows conclusions as follow: (1) apatite grains having relatively low values of  $D_{par}$  ( $\leq 1.75 \mu\text{m}$  for apatite grains etched for 20 second in 5.5 M  $\text{HNO}_3$  at 21 ° C), will anneal rapidly. This is a typical of near-end member calcian fluorapatite (Carlson et al., 1999); (2) apatite grains having relatively high values of  $D_{par}$  ( $> 1.75 \mu\text{m}$  for apatite grains etched for 20 second in 5.5 M  $\text{HNO}_3$  at 21 ° C), commonly anneal more slowly (Carlson et al., 1999); (3) Failure of this  $D_{par}$  parameter from the two characteristics above, commonly occurred for near-end-member hydroxyapatite grains that show high  $D_{par}$  values but anneal faster. Unexpectedly, features of  $D_{par}$  only works well on near-end member fluorapatite grains, even with substitutions of cation such as Mn, Fe, and possibly to rare earth elements and combination of hydroxide (Carlson et al., 1999); (4) the values of  $D_{par}$  related directly to AFT and length data and need not to be converted to any values of Cl content (Donelick et al., 2005); (5) Due to the extremely fine scale measurement of the  $D_{par}$ , so sample preparation must be handled with care especially when etching step was conducted. Incorrect procedure can result inconsistent data (Donelick et al., 2005); (6) Both of  $D_{par}$  and track length data are important to constrain geological conditions in order to produce a correct inverse thermal history (Ketcham et al., 1999).

The effect of the orientation of the tracks on annealing processes have been studied by Geguzin et al. (1968) who showed that tracks with shallow dip angles with respect to the cleavage plane are more resistant to anneal than those with steep angles. It is also significant in apatite that tracks parallel to the crystallographic c-axis are more resistant to anneal than those are perpendicular. As a consequence, when the annealing proceeds, the anisotropic annealing behavior is more pronounced (Green and Durrani, 1977; Donelick, 1991).

The apatite composition  $\text{Ca}_5(\text{PO}_4)_3(\text{F}, \text{Cl}, \text{OH})$  consists of  $\text{Cl}^-$  (chlor), F (flour) and hydroxyapatite. The annealing is very depending on the Cl/F ratio (Gleadow and Duddy, 1981; Green et al. 1985, 1986). It has been showed from electron microprobe that the tracks in apatite with high content of chlorine are more resistant to anneal than those with high content of fluor (Wagner and Van den Haute, 1992).

### 3.5.2 Partial Annealing Zone (PAZ)

Annealing of fission tracks on minerals does not occur at a single temperature, yet it presents a wide temperature range. A variation of the annealing rate which is likely to occur due to the chemical composition has to be considered (Wagner and Van den Haute, 1992).

The range of temperatures with respect to track stability is divided by three zones (Wagner, 1972). Zone I, is called *total annealing* which occur at high temperatures. In this zone, no tracks form; hence the fission track age is zero. At medium temperature, the tracks are more stable with the degree of stability between 0 until 1. In this stage, which is known as the *partial annealing zone* (Zone II), the tracks are partially annealed. The partial annealing zone (PAZ) is of great importance whereas the fission track age starts accumulating at this moment. At low temperatures, the tracks are stable (1 degree of stability). Samples residing in this stage consist of unannealed tracks which formed and stay within this zone (Zone III) and tracks which have been partially annealed in Zone II. The zone is also called the *stability zone* (Zone III). All of the zones are illustrated below (Fig 3.3).

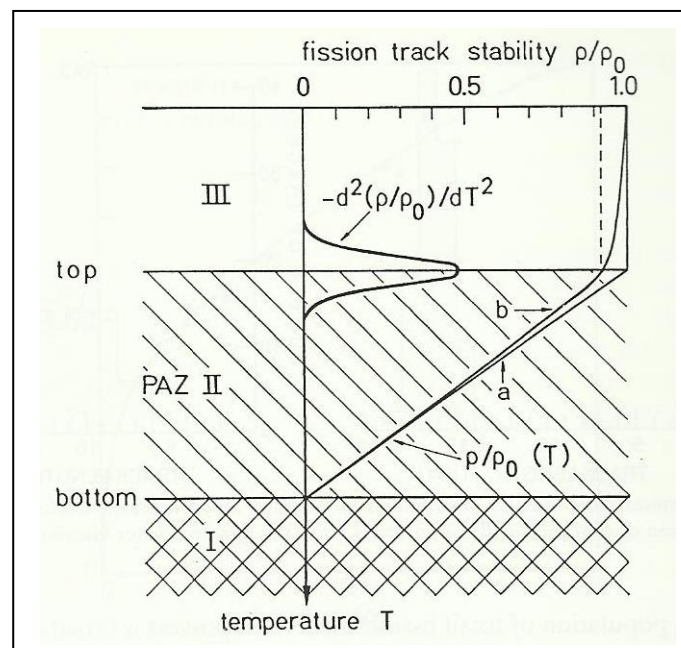


Fig. 3.3: In association with temperature, track stability is divided into three zones; instability zone (I), the partial annealing zone (II), and stability zone (III). The track stability vs. temperature function  $\rho/\rho_0(T)$  theoretically look like curve a, yet it cannot be achieved in nature. Curve b is closer to reality (Wagner and van den Haute, 1992).

In reality, the PAZ concept cannot be straightforward applied. The lowermost temperature of the PAZ is easy to determine whereas the tracks are completely extinct. However, the PAZ top is more difficult to be defined. In apatite for instance, tracks cannot reach a complete

stability at surface temperature. Therefore, the PAZ top is defined as the gradient of stability reaches its maximum, namely 0.90-0.95. On the other hand, the rate of geological process also gives the annealing temperature differently. A fast process, such as volcanism which involved a rapid change of temperature, will need a higher temperature for tracks to be annealed (Wagner and Van den Haute, 1992). The temperature required to anneal is lower for geological processes such as cooling of crystalline basement, uplift and denudation (Gleadow and Lovering, 1978b). Besides of a wide annealed temperatures range (PAZ), a single temperature value is often applied for age interpretation. It is called the closure temperature.

The experiment conducted on Durango apatite by Laslett et al. (1987), which was performed under a given temperature range and time interval resulted that the PAZ of apatite ranges from  $\sim 60^{\circ}$  to  $\sim 110^{\circ}\text{C}$ , with an uncertainty of about  $10^{\circ}\text{C}$ .

### **3.6 Dating Procedures**

Up to now, several dating procedures had been applied in order to determine fission track ages. In general, two procedures have been proposed namely grain-population method and grain by grain method. The distinction of those procedures is based on the strategy applied for analyzing the induced tracks. The grain-by-grain method uses the same grains from the same sample which had been used for the analysis of spontaneous fission. In contrary, the population methods utilize different grains from the same sample for the analysis of induces fission tracks (Gleadow, 1981). Further distinction comes from techniques for induced track revelation (etching technique).

In this master thesis, all samples have been analyzed using the grain-by-grain method which is called external detector method. This method is explained in more detail below.

#### ***3.6.1 External Detector Method (EDM)***

Today the external detector method is the most widely used method for fission track analysis. In principal, the spontaneous fission tracks are obtained from internal polished surfaces of mineral grains which have been revealed by etching beforehand, whereas the induced fission tracks are recorded afterward on a thin sheet of mica. The mica is firmly attached onto the surface of the mineral grains. The pairs of grains-mica then are stacked between standard glass dosimeter and bombarded by slow thermal neutrons in a nuclear reactor. After

irradiation and cooling, the mica is detached and etched in HF 5 molar to reveal the induced tracks, which resulted from the decay of uranium within the mineral grains during irradiation. For detail steps can be seen in Fig. 3.4.

By using this method great care has to be taken, particularly during etching. This is because spontaneous tracks and induced tracks are measured on a different material (mica detector vs. mineral grains). Hence, the etching procedure has to be in standard etching conditions (Tagami and O'Sullivan, 2005).

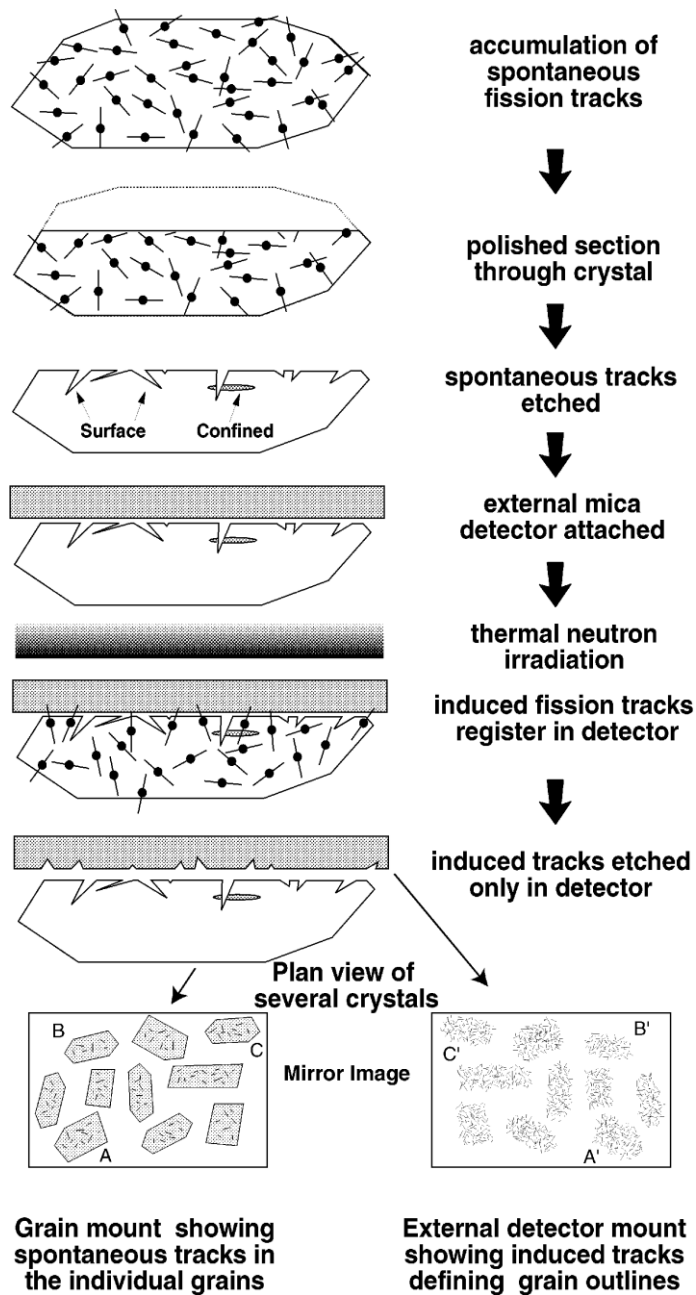


Fig. 3.4: The external detector method was proposed by Hurford & Carter (1991). The apatite after been mounted then was polished until reaches its maximum width. By etching process, the spontaneous tracks can be revealed. Then, muscovite mica is attached onto the apatite surface, and ready to be irradiated with low-energy thermal neutrons, which induces fission in  $^{235}\text{U}$ . The induced tracks have been registered on the mica surface, yet they are still invisible to be observed under an optical microscope. Hence, the mica slice is etched using HF. At the end, we can determine the uranium concentration and AFT ages by counting the number of spontaneous and induced tracks using the known ration between  $^{235}\text{U}$  and  $^{238}\text{U}$ .



### 3.7 Fundamental and Practical Fission Track Age Equation

Principally, fission track analysis method is similar to other dating methods which are based on radioactive parent decay to a more stable daughter atom. The basic equation of the radioactive decay is:

$$\frac{-dN_p}{dt} = \lambda N_p, \text{ or } N_p = (N_p)_0 e^{-\lambda t}$$

$N_p$  is a number of parent atoms remained at any time, and  $\lambda$  is called the decay constant. Integration of the equation above, in order to obtain a number of parent atom at initial time  $(N_p)_0$  yields:

$$(N_p)_0 = N_p e^{\lambda t}, \quad (3.1)$$

The number of daughter atoms  $N_D$ , is the difference between the number of parent atoms at initial time with the one at present time, or

$$N_D = (N_p)_0 - N_p$$

The equation above can be modified by substituting of  $(N_p)_0$  from the equation (3.1) to be:

$$N_D = N_p(e^{\lambda t} - 1), \quad (3.2)$$

The equation (3.2) is actually the basic equation of the isotopic-dating methods including the fission track method.

In the fission track method, the spontaneous tracks are measured instead of the daughter isotope products. It has been explained (sub-chapter 3.3) that the parent isotope of  $^{238}\text{U}$  not only decays by the spontaneous fission but also by  $\alpha$ -emission. Therefore, the total decay constant ( $\lambda_d$ ) is the decay constant for  $\alpha$  emission ( $\lambda_\alpha$ ) added to the decay constant for spontaneous fission ( $\lambda_f$ ) or it can be stated that  $\lambda_d = \lambda_\alpha + \lambda_f$ .

According to equation (3.2) the number of decays due to spontaneous fission is in fixed proportion of  $(\lambda_f/\lambda_d)$  to the total number of decays of the  $^{238}\text{U}$ . The number of fission tracks  $N_s$  accumulated (per unit of volume) is given by:

$$N_s = \frac{\lambda_f}{\lambda_d} {}^{238}\text{N} (e^{\lambda_d t} - 1) \quad (3.3)$$

Because the decay constant for spontaneous fission ( $\approx 8.5 \times 10^{-17} \text{a}^{-1}$ ) is far below the constant for  $\alpha$ -decay ( $1.5 \times 10^{-10} \text{a}^{-1}$ ),  $\lambda_d$  is stated equal to  $\lambda_\alpha$ . So, in order to obtain  $t$  from equation (3.3),  $t$  is:

$$t = 1/\lambda_\alpha \ln[(\lambda_\alpha / \lambda_f)(N_s / {}^{238}\text{N}) + 1] \quad (3.4)$$

In order to determine the quantity of  ${}^{238}\text{N}$ , the samples are then irradiated in a nuclear reactor with a known fluence of slow thermal neutrons ( $\phi$ ). The fission tracks are induced by  ${}^{235}\text{U}$ , hence the number of  $N_i$  will be given as:

$$N_i = {}^{235}\text{N}\sigma\phi, \quad (3.5)$$

where  $\sigma$  refers to the cross section of  ${}^{235}\text{U}$  for fission induced with thermal neutrons. The ratio of abundance  ${}^{235}\text{U}/{}^{238}\text{U}$  or stated as ( $I$ ) in nature is considered constant, except for some rare situation such as occurred at the Oklo mine in Africa (Wagner and Van den Haute, 1992). Hence, equation (3.5) can also be written:

$$N_i = {}^{238}\text{N}\sigma\phi I \quad (3.6)$$

By substituting equation (3.6) into equation (3.4), it yields:

$$t = 1/\lambda_\alpha \ln[(\lambda_\alpha / \lambda_f)(N_s / N_i)I\sigma\phi + 1] \quad (3.7)$$

The equation 3.7 above is a fundamental age equation of the fission track method. From the equation, there are two variables which must be determined namely the ratio of density a spontaneous fission to induced fission and the number of the thermal neutron fluence.

The numbers of  $N_i$  and  $N_s$  from equation (3.7) are numbers of tracks density per unit volume. In practical, both of  $N_i$  and  $N_s$  are measured under a microscope in two dimensions. Therefore, the densities of spontaneous and induced fission are formulated by taking into account the geometry factor ( $g_{s,i}$ ), the average etchable range of a fission fragment track in the investigated area ( $R_{s,i}$ ), the etching efficiency factor ( $\eta_{s,i}$ ), the etch time factor ( $f(t)_{s,i}$ ), and the observation factor ( $q_{s,i}$ ). The densities of observed spontaneous and induced fission ( $\rho_s, \rho_i$ ) in planar dimension are formulated by:

$$\rho_s = g_s N_s R_s \eta_s f(t)_s q_s \quad (3.8a)$$

$$\rho_i = g_i N_i R_i \eta_i f(t)_i q_i \quad (3.8b)$$

The geometry factor ( $G$ ) is a ratio of the surface observed for counting the spontaneous and induced tracks. The factor depends upon the technique applied for revelation the induced tracks. In the present study, we applied the external detector method for which  $G$  is determined equal by 0.5. The etchable range of spontaneous and induced tracks ( $R_{s,i}$ ) has a similar value if the grain-by-grain methods are applied (Togliatti, 1965; Bhandari et al., 1971). The values of  $\eta$ ,  $f(t)$  and  $q$  depend upon the techniques are used for exposure and observation of spontaneous and induced fission tracks. These three of values are then determined by the  $Q$  factor which can be considered as a procedure factor. If the exposure technique of spontaneous and induced fission is similar and both types of fissions are counted under identical conditions of observation then  $Q$  is defined by 1 or is assumed  $\approx 1$  and then a calibration based on age standards such as the  $\zeta$  (zeta)-method has been applied. The  $\zeta$  method will be explained detail in sub-chapter below. The equation for  $Q$  and  $G$  is:

$$Q = \eta_i f(t)_i q_i / \eta_s f(t)_s q_s \quad (3.9)$$

$$G = g_i / g_s$$

The equation (3.7) combined with both of equations (3.8a and b) and (3.9) finally yields the fission track age equation:

$$t = 1/\lambda_f \ln [(\lambda_\alpha/\lambda_f)(\rho_s/\rho_i)QGI\sigma\phi + 1] \quad (3.10)$$

The values of  $\lambda_\alpha$  and  $I$  published by the IUGS Sub commission on Geochronology (Steiger and Jäger, 1977) are widely accepted. The values for  $\lambda_\alpha$  and  $I$  are  $1.55125 \times 10^{-10} a^{-1}$  and  $7.2527 \times 10^{-3}$  respectively. Several methods have been applied to determine a value for the  $\lambda_f$  such as direct measurements with ionization chambers or rotating bubble chambers, radiochemical methods, accumulation of natural fission tracks in mica, and analysis of samples of known age. The most exact value for  $\lambda_f$  is  $8.46 \times 10^{-17} a^{-1}$ , which was obtained by means of a rotating bubble chamber (Galliker et al., 1970). The cross section of  $^{235}\text{U}$  neutron induced fission ( $\sigma$ ) is defined as the ratio of the number of neutrons which produce the reaction per unit of time to the total flux of neutrons. Based on experiments, the value for  $\sigma = 570.8 \times 10^{-24} \text{ cm}^{-2}$  is obtained which correspond to a velocity applied at 2200 m/sec.

### 3.8 Dating System and Calibration

The fission track age equation above needs an exact determination of the fluence of thermal neutrons ( $\phi$ ). This system is known as the absolute approach. In practical, an accurate determination of the amount of  $^{235}\text{U}$  that underwent fission during sample irradiation is difficult to achieve.

Other dating systems were developed in order to avoid the complexity of the determination of an exact value of the fluence neutrons ( $\phi$ ) and  $\lambda_f$ . These so called age standard approaches are based on comparative analyses of age standards. The most common dating system in fission track analysis is the  $\zeta$ - method which it has been also used in this study.

#### 3.8.1 The $\zeta$ - (Zeta) method

The  $\zeta$ - method was introduced by Hurford and Green (1982, 1983) to overcome the doubt of accuracy of the neutrons fluence and the value of  $\lambda_f$ . Using the  $\zeta$ - method, the unknown age samples can be determined from a comparative analysis of one or more age standards (Fleischer and Hart, 1972; Fleicher et al., 1975). The  $\zeta$ -method is basically as follows:

If  $Z$  is defined as  $QI\sigma\phi/\lambda_f$ , therefore the age equation (3.10) can be written as:

$$t_u = 1/\lambda_\alpha \ln[(\lambda_\alpha)(\rho_s/\rho_i)_u GZ + 1] \quad (3.11)$$

$Z$  has dimension of time. The value of  $Z$  is acquired from analysis of the samples of known age  $t_s$  which have been irradiated together with samples of unknown age  $t_u$  with a similar value of  $\phi$  and  $Q$ . From the analysis of the samples with known age, the  $Z$  is defined:

$$Z = \frac{(e^{\lambda_\alpha t_s} - 1)}{\lambda_\alpha (\rho_s/\rho_i)_s G}$$

A value of  $\zeta$  is determined by re-irradiation of the known age standards ( $t_s$ ) and accompanied by a glass monitor. The track density in the glass monitor ( $\rho_d$ ) is equal to the neutrons fluence or  $\phi = B\rho_d$ .  $B$  is a factor for the proportion of neutrons/track. The  $\zeta$  can be written as:

$$\zeta = Z/\rho_d = QI\sigma B/\lambda_f = \frac{(e^{\lambda_\alpha t_s} - 1)}{\lambda_\alpha (\rho_s/\rho_i)_s G \rho_d} \quad (3.12)$$

The age of the unknown age can then be defined from equation (3.11) as follows:

$$t_u = 1/\lambda_\alpha \ln[(\lambda_\alpha)(\rho_s/\rho_i)_u \rho_d G\zeta + 1] \quad (3.13)$$

According to the definition of  $\zeta$  above, the value of the  $\zeta$  will vary due to the  $Q$  and  $B$  factors. The  $Q$  factor reflects differences in track revelation and observation, whilst the  $B$  factor is affected from track counting in the glass/mica (Wagner and Van den Haute, 1992).

It has been explained above that the  $\zeta$  method uses standard age samples. These standard samples have to meet requirements which had been formulated (Hurford and Green, 1981b) as follows: (1) the rocks had been geologically well documented; (2) the samples should be uniform in age which means that the rocks contain of crystals derived from one event only without any mixture from older rocks; (3) the age of the samples should be unequivocal from stratigraphy and other isotopic dating, and display consistent results; (4) the fission track age should indicate the formation age and no correction due to spontaneous track annealing.

### 3.9 Data Analysis and Statistics

The process of radioactive decay occurred randomly. It means that their events within a given interval of time occur by chance alone. In statistical methods, a process such as measuring the activity of radionuclides which involves counting of events during an interval of time is solved by applying Poisson distribution. Poisson distribution is also applied for fission track analysis (Wagner and Van den Haute, 1992).

The Poisson distribution is an asymmetric distribution which is determined by only one parameter, namely mean ( $\mu$ ). As the mean is larger than 5, the Poisson distribution progressively becomes a normal distribution whereas statistical behaviors for continuous normal distribution are also applied (Koch and Link, 1970).

In grain-by-grain methods, the induced tracks are counted in the area that is exactly the imprint of the spontaneous track. Consequently each grain indicates its individual  $\rho_s/\rho_i$  ratio and its individual age (Galbraith and Laslett, 1985). In practice, at least 20 grains or more have to be counted in order to obtain a good statistical result. The total numbers of spontaneous ( $N_s$ ) and induced tracks ( $N_i$ ) in all  $n$  grains are counted as  $N_s/N_i$  and are used as an estimation of  $\rho_s/\rho_i$ . Theoretically, there is no uranium variation in the grains which would affect the individual ratio of  $\rho_s/\rho_i$ . However, in apatite fission track analysis commonly occur that the ratio of  $\rho_s/\rho_i$  vary in every single crystal of one sample. This condition will

lead to various AFT ages in one sample. Green et al. (1989) stated that a spread in ages is caused by different thermal annealing caused by a variety of chemical compositions.

Galbraith (1981) developed a  $\chi^2$  (chi-square) test to measure the uranium variation. The formula with degrees of freedom =  $n - 1$  is as follows:

$$\chi^2 = \sum_j \left[ (N_{sj} - \mathbb{N}_{sj})^2 / \mathbb{N}_{sj} + (N_{ij} - \mathbb{N}_{ij})^2 / \mathbb{N}_{ij} \right],$$

where  $\mathbb{N}_{sj}$  and  $\mathbb{N}_{ij}$  are the expected counts of spontaneous and induced tracks in the  $j$ th grain.  $\mathbb{N}_{sj} = N_s N_j / N$  and  $\mathbb{N}_{ij} = N_i N_j / N$ , with  $N = N_s + N_i$ , which is the total number of spontaneous and induced tracks counted in all grains.  $N_j = N_{sj} + N_{ij}$  is the number of spontaneous and induced tracks counted in the  $j$ th grain. If the chi-square probability ( $P\chi^2$ ) is larger than 5%, the single grain is considered to represent a normal Poissonian distribution.

Commonly, the fission track ages are reported as three ‘mean’ age estimates i.e. the mean, pooled, and central ages. The pooled age is simply obtained from the sum of the spontaneous tracks divided by the sum of the induced ones. The pooled age is applied if several grains meet the requirements of  $P\chi^2 > 5\%$ , hence the grains are assumed related to a given single age (Wagner and Van den Haute, 1992). However, if the distributions of count are inconsistent with purely Poissonian variation, hence the mean age is applied. The mean age is basically the arithmetic mean of the individual ratios of spontaneous to induced tracks. The most commonly used is the central age, which is the weighted mean of the log normal distribution of all single grain ages. All of these three age estimates can be applied if the variation in the count population is consistent with the Poisson distribution. Since the central age method is more robust to outlier data and non-Poissonian distribution, therefore the method is applied in the present study. The central age is formulated as follow:

$$t_c = \frac{1}{\lambda} \log \left( 1 + 0.5 \frac{\lambda \zeta \rho_d \eta}{(1-\eta)} \right),$$

where  $\rho_d$  is the density of tracks in the standard glasses,  $\lambda$  is the total decay of  $^{238}\text{U} = 1.55 \times 10^{-10} \text{a}^{-1}$ .  $\eta$  is essentially obtained from several iterations of the weighted average of the spontaneous fission to the total fissions. In a simple way, the component of  $\eta/(1 - \eta)$  is substituting  $\rho_s/\rho_i$  in the fission track age equation (Galbraith and Laslett, 1993).

### 3.9.1 Error in the Age Determination

Generally, the precision of fission track age depends upon the precision of the track-density ratio of spontaneous to induced tracks  $R (= \rho_s/\rho_i)$  and the determination of the neutron fluence ( $\phi$ ). Since we applied an age standard approach ( $\zeta$ -method), errors due to the neutron fluence determination are essentially referred to the error on the track density of the glass ( $\rho_m$ ) (Wagner and Van den Haute, 1992).

The error on the track density ratio ( $S_R/R$ ) when grain-by grain procedure is used and induced tracks are counted on separate mounts which do not contain etched spontaneous tracks is called non-substraction method. The formula is given as:

$$S_R/R = \sqrt{1/N_i + 1/N_s}$$

The formula above includes  $1\sigma$  confidence interval, which means that there is a  $\approx 68\%$  probability that the true value falls within the range of error.

The error commonly is quoted as a  $\pm$  error for example  $20 \pm 2$  Ma, whereas  $s_t/t$  is counted simply as 10%. Galbraith and Laslett (1985) suggested the lower and upper limits of the error bar are determined by  $t/(1 + s_t/t)$  and  $t(1 + s_t/t)$  respectively, due to log normally distributed of the neutron fluence ( $\phi$ ) and ratio of  $\rho_s/\rho_i$ .

### 3.9.2 Age Component Analysis

In the early of its development, several authors (i.e. Hurford et al. 1984, Yim et al. 1985, Kowallis et al. 1986) applied a graphical diagram to present the different component of AFT ages. The use of a graphical diagram has a disadvantage, i.e. tends to shift peaks and masks low-amplitude peaks (Brandon, 1992). To overcome the problem, Galbraith (1988) introduced the radial plot (Fig. 3.5) for assessing the distribution of single grain ages. On the radial plot, the x and y coordinates are formulated as:

$$x_j = 1/\sigma_j$$

$$y_j = (A_j - A_r)/\sigma_j,$$

where  $\sigma_j$  is the precision of the age estimate  $A_j$ , and  $A_r$  is a reference age (commonly the mean age of all grains). On the plot, the closer the data to the origin, the larger is the error. A



line connecting a given data point to the origin has a slope ( $y/x$ ) equivalent to the reference age. All of the data have similar normalized error (in Fig. 3.5 the error is  $2\sigma$ ).

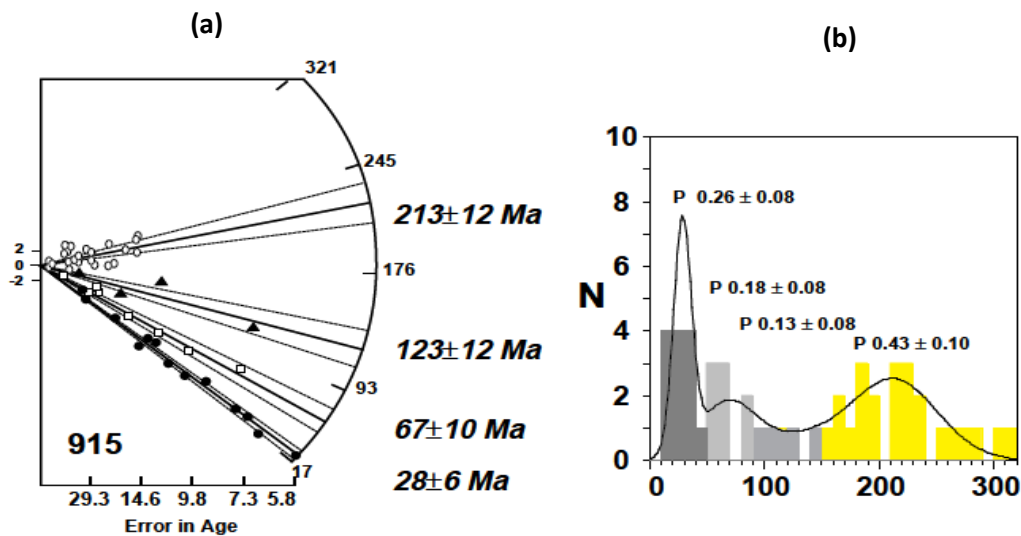


Fig. 3.5: (a) A radial plot described by Galbraith (1988) shows several component ages distributed from the population. On the graphical diagram (b), the peak of 123 Ma is absent on the age distribution. It shows that the graphical diagram has limitation to represent all the component age. (Gallagher et al. 1998)

### 3.10 Samples Preparation

As many 24 rock samples were taken for this study including structural measurements. Practically, we collected rocks with a minimum 2 kg weight per each sample for irradiation process. The rock samples were crushed at the site in a size of 2 cm. It was done to avoid contamination when using the jaw crusher. The next step of the samples preparation was:

#### 3.10.1 Crushing and Density Separation

The 2 cm-rock fragments were crushed in the Pulverisette 13 disc mill (Fig. 3.6). The grinding process has to be done several times until the whole samples run through a sieve with mesh size of  $315 \mu\text{m}$ . The rock powder was then poured into the funnel of a Wilfley 800 shaking table. In practical, only the heavy fraction which assumed contains apatite and zircon will be extracted further.

#### 3.10.2 Magnetic Mineral Separation

Apatite is a non-magnetic mineral. The objective of magnetic mineral separation is to separate the non-magnetic mineral from the magnetic ones. In this study a Frantz magnetic separator has been used (Fig. 3.6). For the first-run, the machine was set up using a current of 0.3 A.

with a vertical and horizontal tilt of  $15^{\circ}$ . This process has to be repeated after the heavy liquid separation by using a current of 0.6 A. and 1.2 A.

### 3.10.3 Heavy Liquid Separation

In order to extract apatite, heavy liquid separation had to be carried out. One of the liquids is called Lithium-based Tungstate (LST) is commonly used in order to get rid of the minerals with densities below of  $2.82\text{-}2.85\text{ g/cm}^3$ . By pouring the crushed samples into the LST, it is expected that the minerals with densities  $> 2.83\text{ g/cm}^3$ , includes apatite would be separated from the lighter ones and sink to the bottom (Fig. 3.6).

The next heavy liquid separation step is uses DIM (Di-Iod Methane). The DIM itself has a density of  $3.3\text{ g/cm}^3$ , therefore apatite will float on DIM and the heavier minerals such as zircon will sink to the bottom.

### 3.10.4 Sample Mounting, Polishing and Cutting

In order to obtain apatite grains larger than  $100\text{ }\mu\text{m}$ , the fragments were then sieved. A mixing of Buehler epoxy and hardener with ratio of 5:1 was used to embed the grains. The apatite grains were spread onto the ring evenly, before the ring was filled up with the epoxy.

After the mounts were solidified, grinding procedure could be started, firstly with 800 sika grinding powder, then with 1000 sika and at last with 1200 sika. The mounts were ground down to expose the maximum size of the internal mineral surfaces.

In the next step, polishing is conducted by a Struers polishing machine. The embedded grains was firstly polished using  $3\text{ }\mu\text{m}$  diamond paste, followed by  $1\text{ }\mu\text{m}$  diamond paste, and the latest polishing step used  $0.05\text{ }\mu\text{m}$  alumina powder.

The polished mounts were then cut into  $\sim 3\text{ mm}$  thick and grinded into small squares of around  $1\text{ cm}^2$  to fit into the irradiation container.



Fig. 3.6: (a) The Pulverisette 13 disc mill was used to crush the rocks; (b) The Wilfley 800 shaking table separates the samples by densities; (c) The Franz magnetic separator separates magnetic from non-magnetic minerals; (d) A heavy liquid i.e. LST which has a density  $2.85 \text{ g/cm}^3$  was used to separate the apatite from the other minerals.

### 3.10.5 *Etching and Packing*

Each sample was etched for 20 seconds in 5 molar  $\text{HNO}_3$  at a room temperature. After the etching procedure, the whole samples were rinsed in running water over night in order to eliminate the effect of the remaining etchant. Each sample was then attached to a similar sized mica sheet with sticky tape. All samples were then packed in a specific order, including four dosimeter glasses IRMM-540 with 12.5 ppm U and two age standards of Durango and Fish Canyon. The samples were sent for irradiation to the Garching Forschungsreaktor FRM-II at the Technical University of Munich.

### 3.10.6 *Unpacking*

Due to the radioactivity of the samples after irradiation, they cannot be unpacked until they reached a safe level. After a secure radiation level was achieved, each pairs of samples were

perforated with five holes. These pinholes are utilized as reference points when an alignment of the mounts under the microscope is done.

After the radiation, the induced tracks on the micas are still invisible under an optical microscope. In order to make these induced tracks identifiable, etching must be carried out for about 20 minutes in 40% molar HF. After etching, each mount and its accompanying mica was attached onto a standard glass slide.

The mica and the apatite mount have different thickness. Therefore, a small piece of a glass slide was placed under the mica to reach a similar elevation. A tiny copper grid with the letter 'A' was glued under the mica as a reference point for alignment (Fig. 3.7).

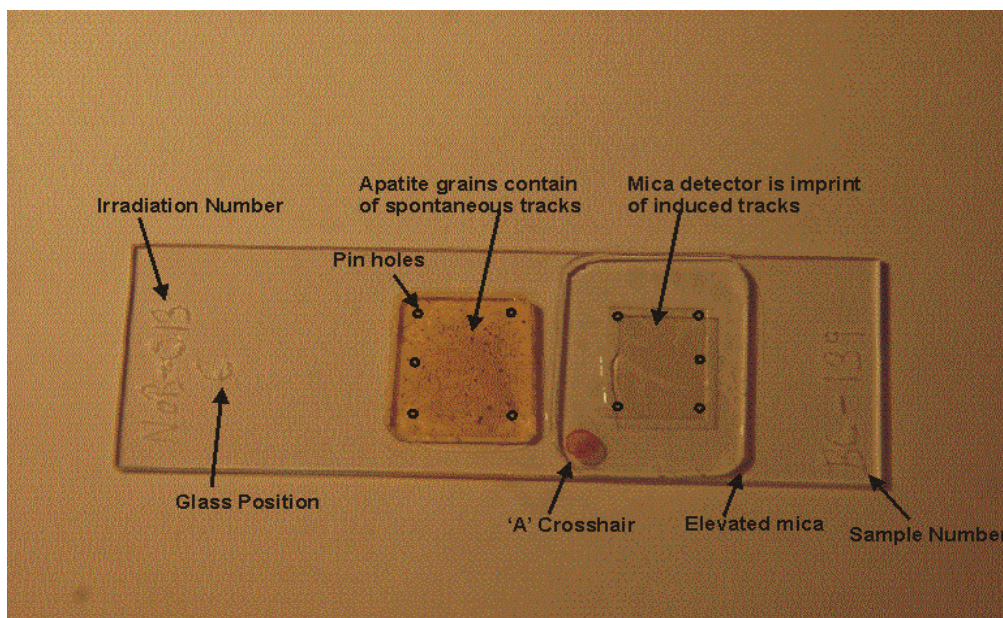


Fig 3.7: Glass slide ready for fission track analysis. A good glass slide has to be labeled properly, and contain information of irradiation number, glass position, five pin holes, crosshair and the sample number.

### 3.11 Microscopy and Modelling

For counting an Olympus BX51 optical microscope with a maximum 2000 times magnification with an automated stage was used (Fig. 3.8). For fission track analysis software namely FTstage 4.01a (© 2004-2005 Trevor A. Dumitru, ©2005 Jasper Canyon Research), TrackKey (version 4.2g 2006 by István Dunkl), and a modeling program namely HeFTy version 1.3c (© 2007 Richard A. Ketcham and Apatite to Zircon, Inc.) are used to calculating  $\zeta$  values, determined unknown AFT ages and produce thermal history.

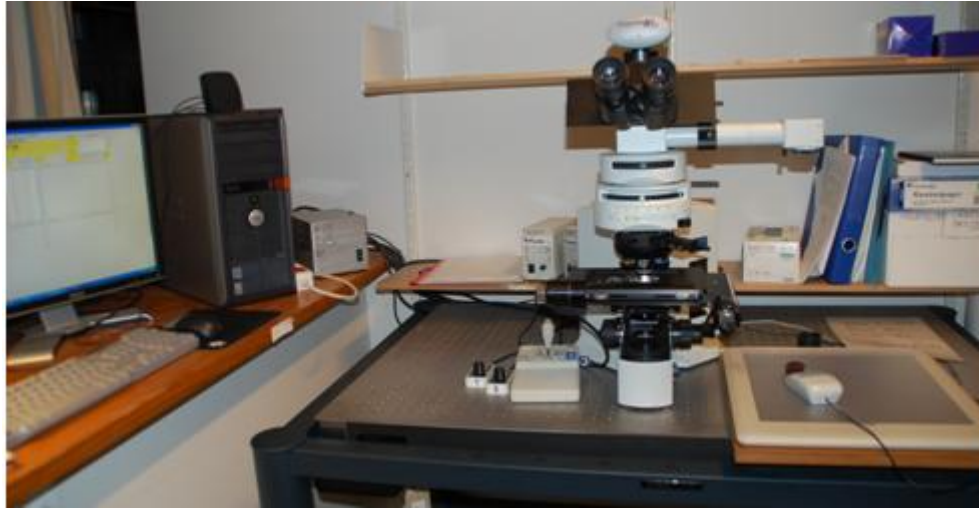


Fig. 3.8: Setup used for AFT analysis. From the left to the right subsequently are: a set of computer, adaptor for the LED, two adaptors and switches for transmitted and reflected light (the buttons are positioned next to the joystick), a joystick, an optical microscope and a stage attached, a digitizing tablet and a cursor with a LED.

### 3.11.1 Calculating the $\zeta$ Calibration Factor and AFT Ages

For determining an unknown AFT age using age standard approach, first the  $\zeta$  value must be determined. According to Hurford (1990a-b), a good  $\zeta$  value requires a calculation of five pair of standard samples which were derived from five different irradiation cans. Commonly, two standard samples were placed in the middle of each irradiation can. In total, 10 standard samples consisting of five samples of Fish Canyon Tuff and another five samples from Durango were counted.

The tracks density on the dosimeter glasses is related to the neutrons fluence and is represented as  $\rho_d$  in equation 3.12. The magnitude of the neutrons fluence depends upon the position of the samples during the radiation (see Appendix I), the closer a sample is to the radiation source, the larger its track density.  $\rho_d$  is derived from a linear regression line of several track numbers ( $N_d$ ) of each dosimeter glass in one can. The value of  $N_d$  must be divided by  $54.76 \text{ mm}^2$  (wide of one grid area in the microscope used) to produce the track density  $\rho_d$ . By plotting all of the  $\rho_d$  values in a diagram, one will have a linear trend line and its equation (see example in Fig. 3.9 and Appendix II).



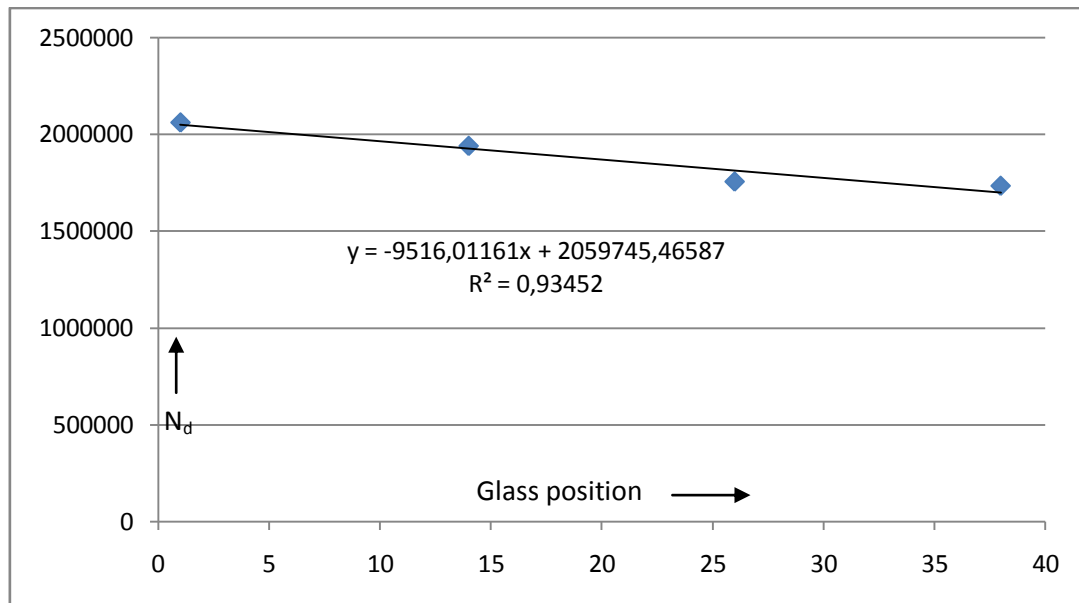


Fig 3.9: The diagram shows a plot of the number tracks on the dosimeter glasses ( $N_d$  values) in order to obtain linear equation of the track density ( $\rho_d$ ) function. Example was taken from irradiation NOB 003.

To obtain a  $\zeta$  value and correct AFT ages, several factors must be noted when selecting grains is done. They are:

- The grains counted must be orientated parallel to the crystallographic  $c$ -axis due to their isotropic behavior of etching. They are recognizable easily when observing the spontaneous tracks under reflected light because their tracks opening are parallel to each other.
- The grain size should be bigger or equal to 25 counting grids.
- Avoid choosing grains with big cracks or at least cracks smaller than 1 counting grid.
- The surface of grains should be clean and clear.
- Most important is that only 'true' tracks are counted; counting of any tracks produced by dislocations which appear similar to the real tracks must be avoided to count. The track-like defects are rather difficult to identify because they have a similar track opening when they are observed under reflected light. One of their prominent features is that they are commonly present in rows or columns with similar track direction and magnitude. Recognizing real tracks is critical; otherwise wrong AFT ages will be produced.
- Counting tracks both on the standard samples and unknown samples always involve movement of the stage between the spontaneous tracks on the grains and induced ones

on the mica. Therefore, a proper alignment must be done thoroughly in order to have a correct U content of analyzed grains.

- Avoid selecting grain contain strong zoning and other mineral inclusions particularly those having a very high uranium concentrations. The zoning represents different uranium concentration in one grain. Counting tracks in zoning areas tends to produce an incorrect number of both spontaneous and induced tracks, especially if the alignment has not been done properly.
- There is no optimal total number of grains and depends on several factors such as the degree of separation between modal ages and the relative proportions of grains in each population. Hurford et al (1984) suggested counting 50-100 grains, although Kowallis et al (1986) recommended 5-10 grains are adequate. In this present study, minimum 20 good grains have to be counted in order to have more precise AFT ages.
- Counting tracks in standard samples and the samples were done under 1250 magnification.

The number of spontaneous and induced tracks is defined as  $N_s$  and  $N_i$  respectively. A value of  $\rho_d$  for the analyzed sample is obtained from substituting the  $x$  variable of the linear regression equation with the sample position in the can (Fig. 3.9). Practically, a  $\zeta$  value can be produced easily using the TrackKey software (Fig. 3.10), by inputting  $N_s$ ,  $N_i$ ,  $N_d$ , and  $\rho_d$ ; otherwise one can put all the values into the equation 3.12 manually. The AFT age standard applied is  $31.4 \pm 0.5$  Ma (McDowell and Keizer, 1977) and  $27.9 \pm 0.5$  Ma (Hurford and Hammerschmidt, 1985) for Durango and Fish Canyon Tuff respectively. It is noteworthy that the values of  $N_s$  and  $N_i$  are still in two dimension. Therefore, in order to get a density of spontaneous and induced tracks ( $\rho_s$  and  $\rho_i$ ) in three dimensions, one first has to apply equation 3.8a and 3.8b. Once all of the  $\zeta$  values have been produced from 10 standard samples, a weighted mean of  $\zeta$  value can be obtained using the statistic program (ZetaMean software by Mark Brandon, 2001).

Procedure for having AFT age from unknown samples is almost similar to the one as we calculate the standard samples. A small difference is that a weighted mean  $\zeta$  value is added other than  $N_s$ ,  $N_i$ ,  $N_d$ , and  $\rho_d$  (RhoD in the software).



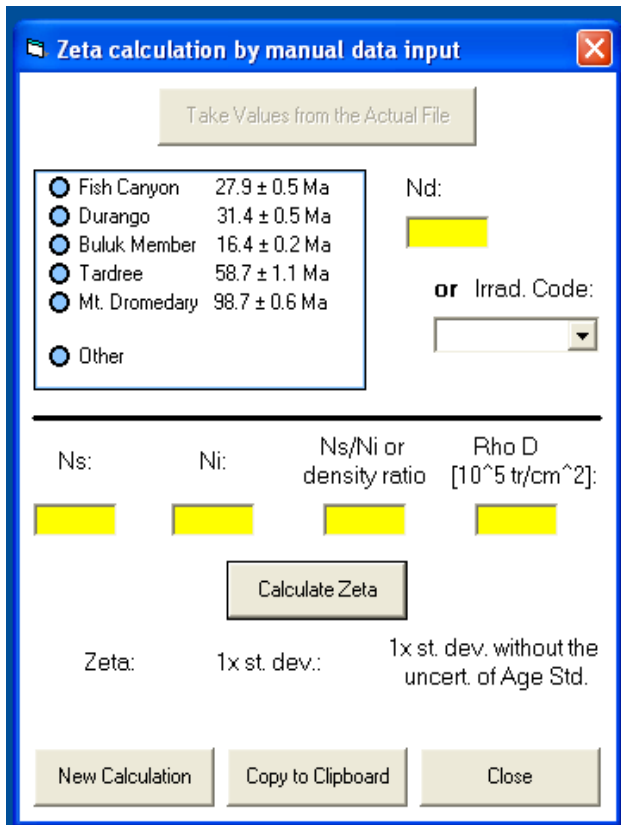


Fig. 3.10: Screen displays Zeta calculation menu of the TrackKey software (version 4.2g by István Dunkl). By inputting the  $N_s$ ,  $N_i$ ,  $N_d$ ,  $N_s/N_i$ ,  $\rho_d$  and select one of the standard age that we are counting, one of the zeta value can be produced.

### 3.11.2 Track Length Measurement and $D_{par}$

Track lengths were only measured from confined tracks which are parallel to the crystallographic c-axis. Confined tracks are tracks located in the interior of the grains but are exposed by etchant because they intersect cracks or cleavage planes at the surface (TINCLES) or other surface tracks (TINTs). The TINCLES are considered less accurate because the gap between fractures tends to lengthen their true length.

In practical work, the track lengths were measured using an optical microscope with 2000 times magnification. The rule of thumbs is to find as many as possible of confined tracks in samples by looking at their uranium concentrations. Commonly, concentration higher than 20 ppm produce more confined tracks. Confined tracks are identified easily as they are entirely located below and parallel to the surface. In general, their appearances are more or less simultaneously in focus along the total length under reflected light.

Selecting grains in which the track length is measured, is less strict than the selection process when counting the AFT age. The grains can be chosen regardless if they contain dislocations, the surfaces are not clear, or the grain width is smaller than 25 grids. However, several conditions should be noted as length measurement proceeds. They are:

- The grains must be parallel to the  $c$ -axis crystallographic projection or within the range  $\sim 15^\circ$  of horizontal to the surface.
- The etching and annealing behavior is anisotropic with respect to the crystallographic axes. In case for apatite, the annealing is slow but the etching process is fast for tracks parallel to the  $c$ -axis crystallographic (Gallagher et al., 1998). Therefore, we measure the angle of the track before length measurements were carried on.
- The tracks measured must not have contact with fractures or the rims of the grain.
- Gallagher et al (1998) suggest to measure 50-150 track length in one sample. In present study, 100 measurements have been made.

The track length data are usually presented in terms of the mean standard deviation and length distribution at 1- $\mu\text{m}$  intervals. An average length produced from each sample is called the mean track length (MTL).

The kinetic annealing parameter  $D_{\text{par}}$  was also measured together with the track length measurements. A minimum of three measurements for  $D_{\text{par}}$  were carried out adjacent of the confined track for which a length was measured. In addition, the  $D_{\text{par}}$  was measured for each grain that has been selected for counting fission track ages.

### *3.11.3 Thermal History Modeling*

To develop a time-temperature history, inverse thermal modeling was developed using HeFTy software. HeFTy is a computer program that performs both of forward and inverse modeling for low-thermochronological data including apatite fission track, U-Th/He and vitrinite reflectance (Ehlers et al., 2005).

The parameters that are used for developing time-temperature histories are the AFT ages, the kinetic annealing parameter (in this case  $D_{\text{par}}$ ), and the length track measurements. Before running the model, a boundary condition must be set up which considers both temperature and time (age when an event occurred in the vicinity of the study area) (Ketchum, 2005).

In this present study, four constraints have been used. These time constraints were obtained from other studies which applied geochronological methods in this area. The first constraint is a cooling event of the southern Norwegian crust. It was studied by Dunlap and Fossen (1998)

who used  $^{40}\text{Ar}/^{39}\text{Ar}$  dating on K-feldspar. The analysis indicated that cooling rates occurred in the range of  $2^{\circ}\text{-}5^{\circ}\text{C}/\text{Ma}$  during the period of 300-250 Ma. During this time interval, the K-Feldspar resided sustainably at temperatures range of  $250^{\circ}\text{-}300^{\circ}\text{C}$ . The exhumation event during this period was interpreted as a result of the rifting event in the Oslo region which effected lowering of the base level and an increase of the erosion rate. These data was also advocated by Eide et al. (1999) who applied  $^{40}\text{Ar}/^{39}\text{Ar}$  dating on the Western Gneiss Region and the Nordfjord-Sogn Detachment Zone. Even though, their data is slightly different in the cooling magnitude, yet the time constraint is almost similar. In this case, the time between 320-240 Ma was proposed to explain the age differences. The second time constraint was taken from a succession of alkaline dike intrusions in the Bergen-Sunnhordland area. The dikes had been dated by several authors. Færseth et al. (1976) used the K-Ar dating of amphiboles from 15 dikes in Sunnhordland. The results yielded three episodes of intrusions during Permian-Jurassic time i.e. 281, 226, and 168 Ma. Løvlie and Mitchell (1982) who dated dikes located in Sotra, north of Sunnhordland obtain ages of 250-270 Ma. They predicted that the dikes were emplaced at ambient temperatures of  $150^{\circ}\text{-}500^{\circ}\text{C}$ , assuming that the geothermal gradient was about  $30^{\circ}\text{C}/\text{km}$ . Torsvik et al. (1997) who applied paleomagnetic analysis on several dolerite dikes in the Sunnfjord area also yield age between 250-270 Ma. Here, the range of 250-280 Ma and  $150^{\circ}\text{C-}500^{\circ}\text{C}$  were selected as a second time and temperature constraint respectively. The third constraint is based on the newly discover of Jurassic sediments in the subsea road tunnel across Vatilestraumen close to Bergen. The sediment is part of the Bjorøy Formation. Based on the vitrinite analysis performed on coal fragments, it indicated that the sediments have been overburden less than one kilometer and had temperature less than  $50^{\circ}\text{C}$ . From the pollen and spore assemblages referred that the formation was deposited during the Oxfordian, 160-155 Ma (Fossen et al. 1997). The fourth constraint is the AFT age of the sample and the temperature range of  $110^{\circ}\text{C}$  until surface temperature.

In the present study, a Monte Carlo approach was applied to generate and evaluate a large number of time-temperature paths. More paths passing through a certain way are more likely close to the correct path (Ketcham, 2005). At the end of the modeling process, there are three color contours in the time-temperature window, whereas the green contours represent all the possible paths, the pink contours indicate the good paths, and a black contour is the best fit which represent the best scenario of our hypothesis (Fig. 3.11).

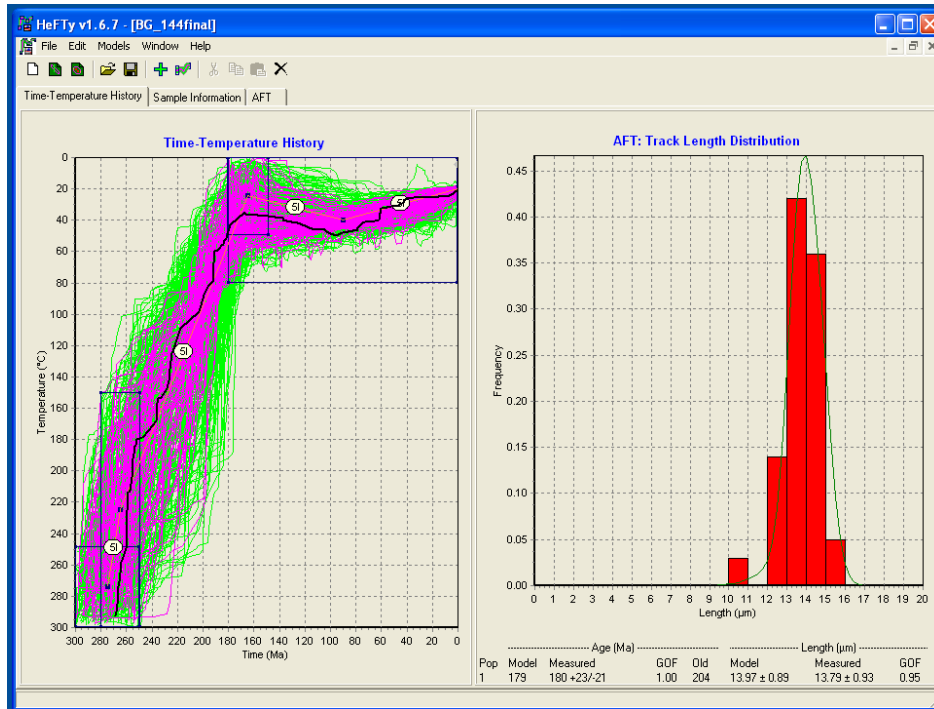


Fig. 3.11: The print screen of HeFTy program simulates sample BG-144. The model has been set up to reach 100 good paths (pink contours) and one best fitting path will be chosen (black line).

Compilation of AFT analysis, the Zeta value, and the inverse thermal modeling will be resumed in the following result chapter. Structural analysis is also explained included fracture and fault analysis.

## 4. RESULTS

In this chapter, both structure geology and AFT results are described. Analysis of structure geology includes fracture, fault, and foliation analysis. Results of AFT analysis are illustrated in tables, figures, profiles, and diagrams in order to delineate data trend of the area.

### 4.1 Field Structural Data and Analysis

During field work, 24 samples collecting and structural data were recorded. Collected field data consists of rock descriptions, orientation of foliations, trend and dip of fractures, faults, trend and plunge of striations, lineation and spacing of fractures (see Appendix III for more details). Only lithologies which are considered contain enough apatite were sampled, e.g. augen gneiss, granite, granodiorite, and diorite (Fig. 4.1). Detail rock descriptions and thin sections observations are found in the Appendix IV.

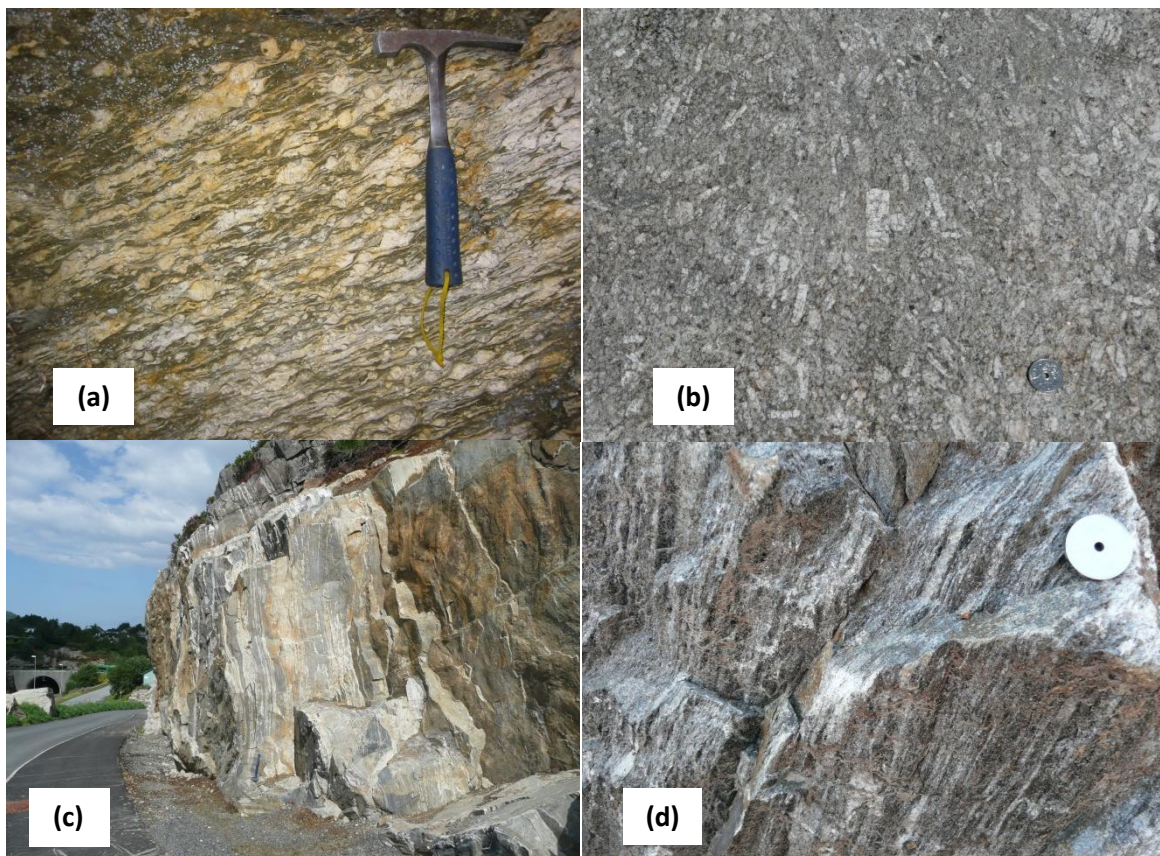


Fig. 1.1: Pictures show field outcrops; (a) outcrop of augen gneiss (sample BG-38) is rich in biotite and cm - dm feldspar, (b) outcrop of porphyritic granite (BG-63) shows a large size of K-feldspar (up to 4 cm long) in a medium-coarse grained quartz, feldspar and biotite matrix, (c) outcrop of light grey granite located at Førre, (d) Outcrop of well foliated gneiss is situated at Vindafjord (sample BG-118).



The study area has been investigated with respect to lineaments by Karpuz (1990) who produced a lineament map based on LANDSAT images (Fig. 4.2.). The lineaments in fact represent fracture zones which developed under semi-brittle and brittle deformation conditions (Valle et al. 2002).

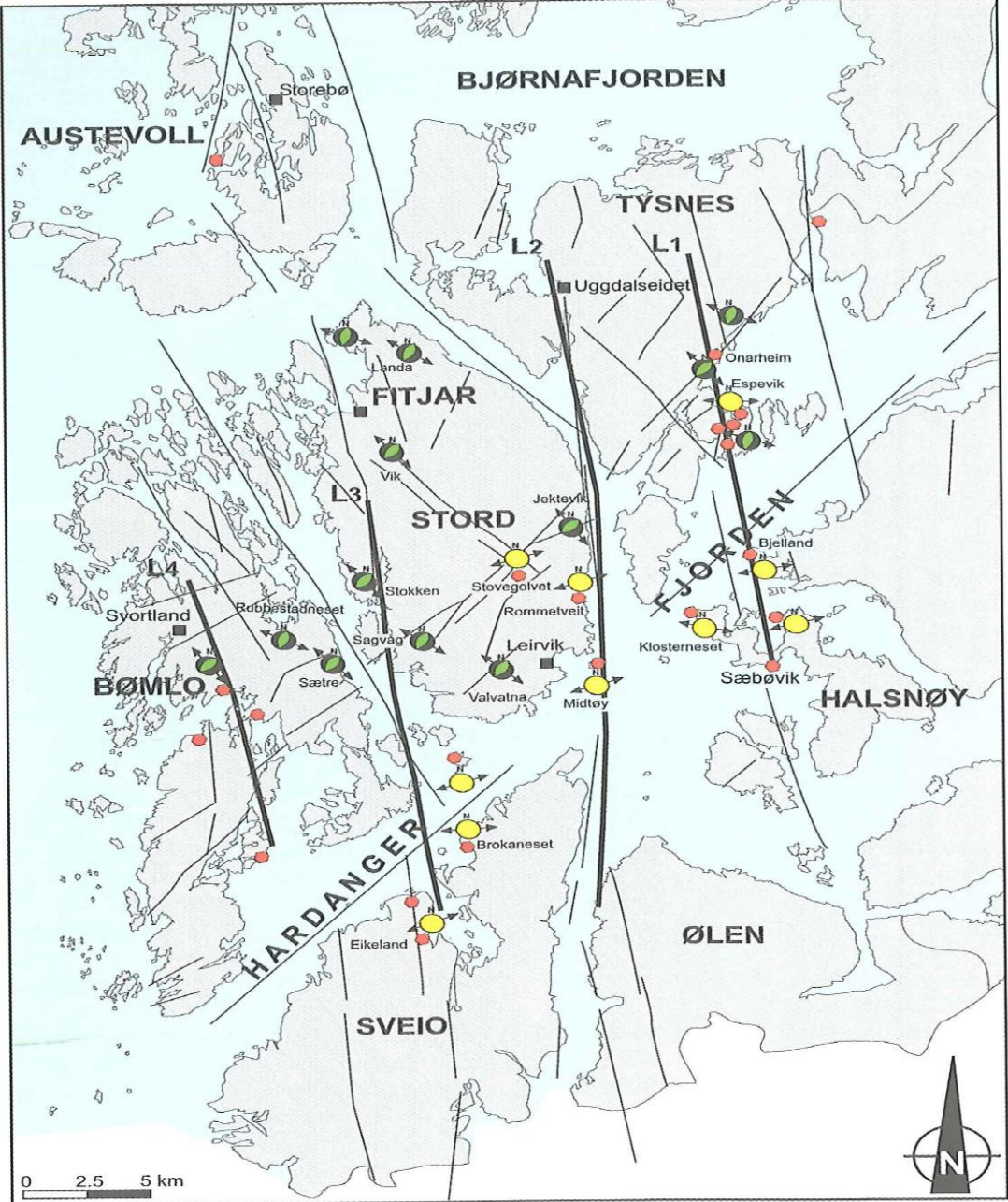
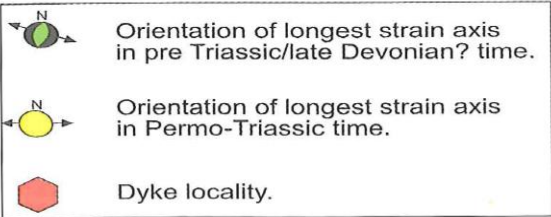


Fig. 4.2: The combined map shows the paleo stress pattern (Valle et al., 2002), and the lineament interpretation from Karpuz et al. (1991). The lineaments are signified L1-L4.



#### 4.1.1 Fracture Analysis

From 18 localities, about 98 data fractures have been measured and plotted. The fractures mainly occur as a set of joints and shear fractures. The two types of fractures are hardly distinguished in the field because of lack of ornamentation on the fractures. Commonly the shear fractures can be recognized by presence of slickenlines. However, none of the fractures appear with the presence of slickenlines. The joints typically present as conjugates, with X intersection geometries. This geometry is mostly found in the field.

The majority (68) of the total fractures (98) show dominantly a range of N-S, NE-SW and NW-SE strike direction (Fig.4.3a and b). The remaining fractures (30) display trend of E-W direction (Fig. 4.4). Most of the fractures exhibit steeply dipping and only minor show dip less than  $30^{\circ}$ .

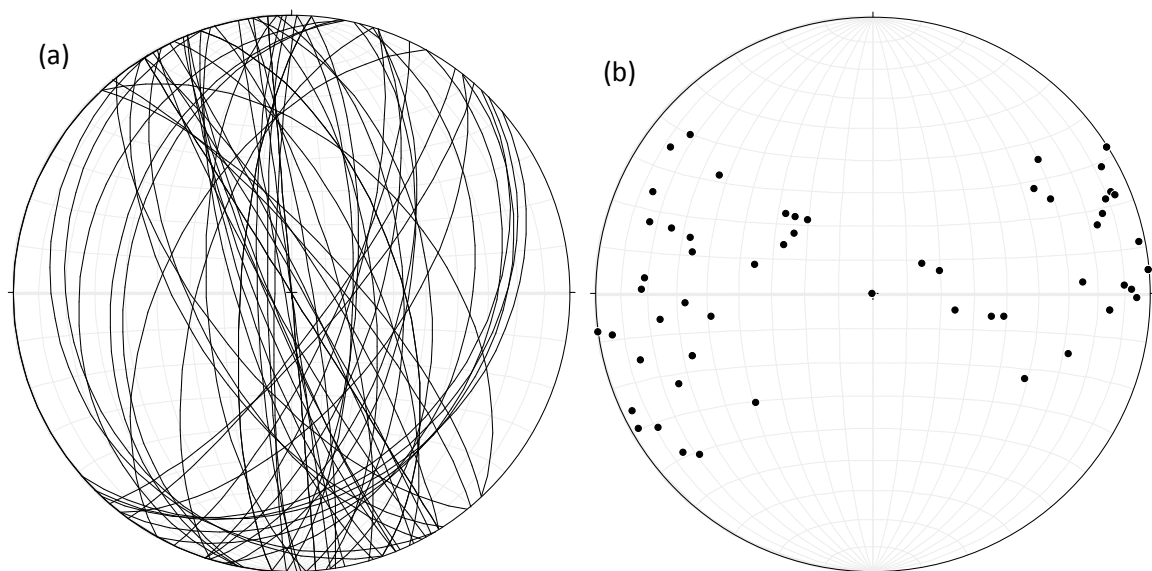


Figure 4.3 Plot of 68 fractures use stereoplot (equal area). The plot denotes that the main trend fracture is N-S, NW-SE and NE-SW direction (left). The poles of fracture are illustrated on the right which represents the longest strain axis.

One fact about joints is that they represent the response of regional stress. Here, if we assume that most of the fractures formed by pure of mode I opening without any resolved shear stress (Davis and Reynolds, 1996), hence the poles of the joints will give the direction of the longest horizontal strain axis, which in this case is parallel to the least principal stress axis ( $\sigma_3$ ) (Anderson, 1951). Fig 4.3b indicates that the longest strain axis has a range of NE-SW, E-W, and ENE-WSW direction. The NE-SW longest strain axis is interpreted have formed in Pre-



Triassic or late Devonian time. Both the E-W and ENE-WSW longest strain axis developed in the Permo-Triassic (see Fig. 4.2, Valle et al., 2002).

Several previous studies on the alkaline dykes (e.g. Furnes et al, 1982a; Torsvik et al. 1997; Løvlie and Mitchell, 1982; Færseth et al. 1976; Fossen and Dunlap, 1999) in these areas (Sunnfjord, Sotra and Sunnhordland) indicate that the dyke ages mostly range from 220-270 Ma. Only one dyke in Sunnhordland was reported having a young age of 164 Ma (Færseth et al. 1976). Even though, a cross cutting relationship between the joints and the dykes are hardly observed in the sample localities, it can be inferred from more detailed study (Valle et al. 2000) that the joints have an older age than the dykes, and hence have a minimum age of the Pre-Triassic. Færseth et al. (1995) stated that the rifting event in the North Sea, which occurred during the Mid-Permian, gives evidence of E-W extensional stress direction. It is most likely that the joints in the area reflect the rifting event during that time.

About 30 fracture measurements show deviation from the major of N-S trend direction. Most of these fractures have an E-W strike (Fig. 4.4). These fractures are evenly distributed in the study area. The presence of these minor fractures was rarely discussed in scientific journals. Three hypotheses could be proposed; the first is probably, they are a set of younger joints, which are called release joints formed near the surface during uplift and erosion. Commonly release joints form as mode I tension perpendicular to the former direction of tectonic joints (Davis and Reynolds, 1996), thus in this case perpendicular to the strike range of N-S. The second hypothesis is they formed as a response of a local stress. As we see in a bigger scale the segment fault of the Hardangerfjord Shear Zone, the Bjørnafjord Fault and the Bergen Arc Shear Zone consist of various fault directions. The last hypothesis is that they can be conjugate features of the NE-SW and NW-SE fractures. It is a common pattern found in the X intersection joint type which formed acute angles at their intersection.

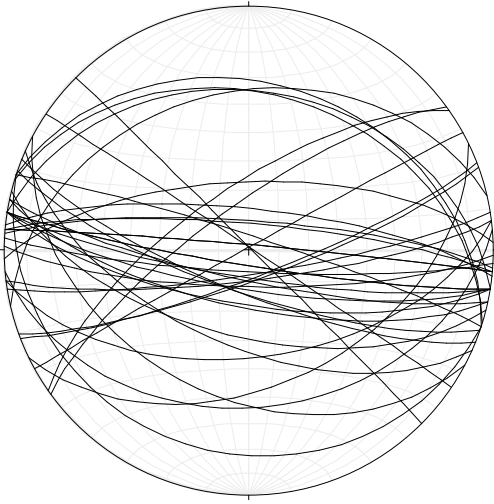


Fig. 4.4: Plot of 30 fractures exhibits main trend of E-W direction.

#### 4.1.2 Fault Analysis

Likewise the fractures, the faults in the study area also display a similar trend compared to those of the fractures. Unfortunately, the stratigraphic markers are unclear in the field to decide the relative movement on the fault surface. By referring to Valle et al. (2002) and the geological map of the area published by the NGU, reported that normal movement dominates, either by dip slip or oblique slip.

The trends are varied (Fig. 4.5), with a majority of the faults (9 measurements) oriented NE-SW and NW-SE direction with most of striae indicating down to SE oblique and only one rake shows dip slip movement (rake in the range of  $6^{\circ}$ - $66^{\circ}$ ). The remaining fault data are distributed as follows: (a) faults show SW strike direction (3 measurements) but striation data are unavailable, (b) most of fault oriented E - W direction (4 measurements) indicate down to the W oblique slip and one rake exhibits dip slip movement (rake in the range of  $32^{\circ}$ - $55^{\circ}$ ).

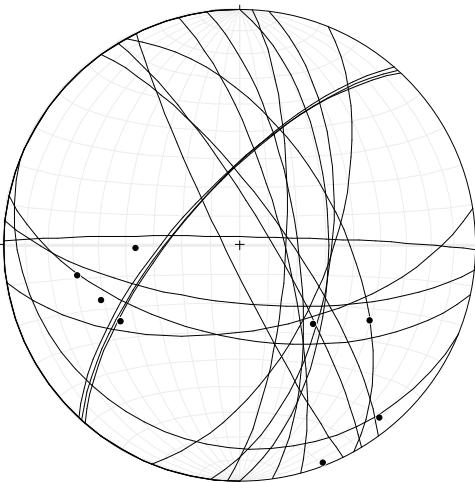


Figure 4.5: Plot of fault planes and striations data set. The fault planes are indicated by great circles, while the points are the trend and plunge of the striations.

The main trend of the Hardangerfjord Shear Zone is NE-SW striking faults with low slope less than  $30^{\circ}$ . However, those faults are slightly not prominent in the area. This might be due to limited data collection. By analyzed 161 striations, Valle et al. (2002) concluded that the NE-SW striking faults are the major faults consistent with the main trend of the HSZ.

Except of the E-W striking fault, all of the faults correspond to the lineament (Fig. 4.1) and paleostress observations in the study area. Interestingly, the E-W faults only occur in the block where the curved segment of the Bjørnafjord Fault is located. Hence, it is speculated that the Bjørnafjord Fault exerted influence to the direction of the local faults in the adjacent area.

#### 4.1.3 Foliation Analysis

About 16 foliations have been measured. The major data exhibit a NE-SW trend with dip oriented to NW and minor data show a NNW-SSE direction with dip to the W and E (Fig. 4.6). These directions entirely correspond and represent the emplacement of the thrust sheet toward the ESE (foreland) and shifted to WNW hinterland directed along the basal décollement zone. The backsliding event commenced at about 400 Ma (Fossen 1992, 1993).

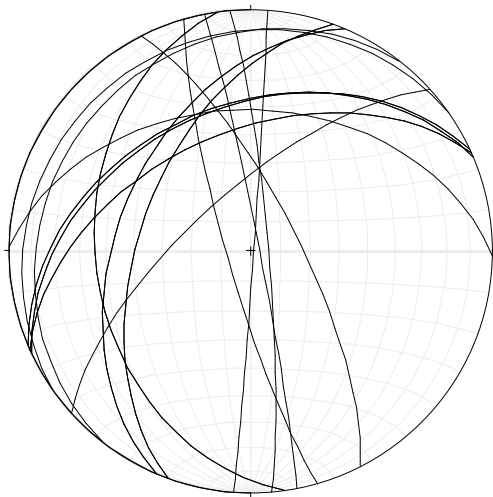


Figure 4.6: Plot of foliation exhibits mostly NE-SW direction with dip oriented to NW.

## **4.2 Result of AFT**

As many as 24 samples have been analyzed, including fission track counting, track length measurements of 5 samples, and  $D_{par}$  measurement for the entire samples. All these parameters were integrated in the HeFTy program to model five inverse thermal history models.

#### 4.2.1 Apatite Description

Generally, the whole samples display fair-good apatite quality. Several particular features on the apatite, however could lead to possible errors in the counting. Typical features are; bad grain surface, wide cracks, zoning whereas uranium is concentrated in clusters, thus the tracks are distributed unevenly on the grain, dislocations, and very low or very high uranium content (Fig. 4.7).

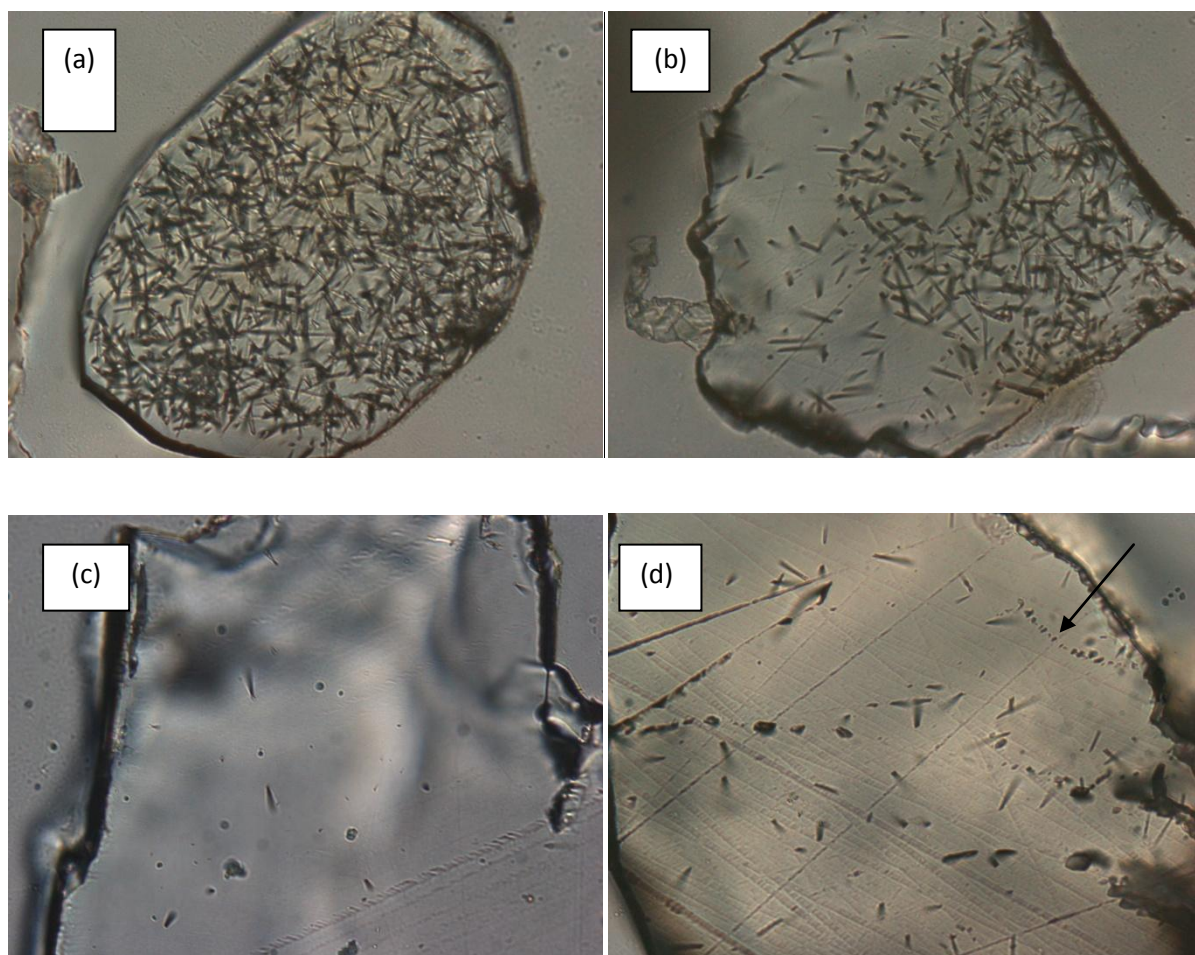


Fig. 4.7: Several defect features commonly occur on apatite. These defects lead to possible errors in the counting. They are; (a) very dense fission track due to very high uranium content, (b) zoning in response of difference uranium concentration, (c) low uranium concentration results rare fission tracks, (d) dislocation features (marked by arrow).

#### 4.2.2 Zeta Calibration Factor

The personal Zeta factor was calculated from ten standard samples. The Zeta value itself is counted as a weighted mean of individual Zeta values of all standard samples (Tab 4.1). Using the ZetaMean program by Brandon (2001), the weighted mean is determined and yield the Zeta value of  $241.97 \pm 8.76$  with  $1\sigma$  error. Here, the independent standard ages used in the

TrackKey are: Durango =  $31.4 \pm 0.5$  Ma (McDowell and Keizer, 1977) and Fish Canyon Tuff =  $27.9 \pm 0.5$  Ma (Hurford and Hammerschmidt, 1985).

Irrad. No	Sample No.	No. Of Grains	$\rho_s$ ( $\times 10^5$ )	( $N_s$ )	$\rho_i$ ( $\times 10^5$ )	( $N_i$ )	$\rho_d$ ( $\times 10^5$ )	( $N_d$ )	P ( $\chi$ )	U (ppm)	Zeta
NOB 002	FC-02	16	2.25	81	11.76	423	17.39	9622	72.5	9.71	$167.89 \pm 20.66$
NOB 002	Dur-01	19	1.63	117	11.47	823	17.50	9622	97.3	9.45	$253.11 \pm 25.46$
NOB 003	FC	18	1.94	70	15.44	557	18.60	10250	78.33	12.13	$239.25 \pm 30.75$
NOB 003	Dur	21	1.57	129	10.37	852	18.79	10250	45.23	7.95	$221.29 \pm 21.31$
NOB 006	FC-01	3	1.77	13	14.72	108	20.44	5584	82.49	10.22	$227.27 \pm 66.91$
NOB 006	Dur	18	1.70	155	20.35	1861	20.41	5584	23.81	14.11	$370.35 \pm 31.91$
NOB 008	FC-01	17	1.92	89	15.16	704	18.95	7919	96.68	11.53	$233.44 \pm 26.72$
NOB 008	Dur-01	14	1.36	66	11.51	558	18.81	7919	77.73	8.70	$283.01 \pm 37.25$
NOB 011	FC	20	2.27	163	18.04	1294	16.90	7012	12.22	15.08	$262.73 \pm 22.56$
NOB 011	Dur	14	1.42	54	10.72	408	16.86	7012	69.95	9.22	$282.12 \pm 41.24$
										<b>Weighted Mean Zeta</b>	<b><math>241.97 \pm 8.76</math></b>

Tab 4.1: All of the standard samples were analyzed using the external detector method, with a geometry factor  $G=0.5$ ,  $N_s$  and  $N_i$  are numbers of spontaneous and induced tracks respectively,  $\rho_s$  and  $\rho_i$  are the density of spontaneous and induced tracks per  $\text{cm}^2$ ,  $N_d$  is the amount of induced tracks on the mica, and  $\rho_d$  is the density of induced tracks on mica per  $\text{cm}^2$ ,  $P(\chi)$  is the chi square value indicating uranium variation in each sample.

#### 4.2.3 AFT Data and Inverse Thermal Modelling

The AFT data is presented in Tab 4.2. Single grain ages and radial plots are presented in the Appendix V. Based on the sample location distribution, three blocks were defined namely the south block, the middle block and the north block (Fig. 4.8). The south block is divided from the middle block by the Hardangerfjord Shear Zone, thus the south block is being a footwall of the zone and the middle block is its hanging wall. The middle block is also being a hanging wall of the normal Bjørnafjord Fault which extends around the Stord and Tysnesøya. The north block is located in the hanging wall of the Bergen Arc Shear Zone (BASZ) and is minor exposed in the study area.

##### 4.2.3.1 Footwall of the Hardangerfjord Shear Zone

The AFT ages in the footwall of the HSZ range between  $180 \pm 8.4$  and  $105.6 \pm 7.9$  Ma, thus all AFT ages range from middle Jurassic times until the lower Cretaceous (Fig. 4.8). However, only a few samples are in the range of middle Jurassic times. Calculation of the average AFT age is  $145 \pm 16$  Ma (see Appendix VI) which is within the range of Late Jurassic – Early Cretaceous time. 13 samples were taken from this block. All samples display errors less than 10%, hence overlap errors can be avoided. The largest error is on sample BG-120

which has the lowest U concentration. Unfortunately, two samples exhibit  $P(\chi^2)$  less than 5 %, which means the samples have more than one population. Since the central age is used, the error due to a bimodal population can be handled. The U concentration shows a wide range between 4-70 ppm. All samples were analyzed, even though only 10 grains were found in sample BG-62, which has ~70 ppm U. The Mean Track Lengths (MTL) are slightly varied between  $11.15 \pm 0.20$  -  $12.79 \pm 0.16$   $\mu\text{m}$  and the standard deviation ranges from 1.58- 1.84  $\mu\text{m}$ . The values for  $D_{par}$  are between 1.11-1.66  $\mu\text{m}$ , and the mean  $D_{par}$  is 1.32  $\mu\text{m}$ .

Inverse thermal history modeling of this block was carried out for samples BG-144, BG-38 and BG-62 (Fig. 4.9). Both samples BG-144 and BG-62 have many long tracks, which are also reflected in the T-t paths. The models display rapid cooling or short residence within the PAZ, thus the tracks had not much time to anneal. The rapid cooling of sample BG-144 has initiated around 220 Ma (Triassic), and indicates a fast cooling rate until 190 Ma. If it is assumed that the temperature of the PAZ is between  $120^{\circ}\text{C}$ - $60^{\circ}\text{C}$ , the cooling rate is predicted to be  $\sim 2^{\circ}\text{C}/\text{Ma}$  within 30 Ma. Fast and slow cooling events which occurred below and upper the PAZ are not considered, because the AFT method is only sensitive within the temperature range of the PAZ.

The inverse thermal history model for BG-62 also shows a rapid cooling within the PAZ. The cooling event commenced at 190-180 Ma. The short time of the sample resided in the PAZ implies that the cooling rate is faster than that of BG-144, which is predicted to be  $\sim 6^{\circ}\text{C}/\text{Ma}$ . Mostly long tracks dominate, reflecting a relatively short period in the PAZ. After very rapid cooling, the sample entered the PAZ during the Upper Jurassic until Middle Cretaceous time.

The T-t path for sample BG-38 is shallower than those others two. The cooling event began at 250 Ma and terminated within the PAZ at 210 Ma (Triassic). Therefore, the cooling rate is rather slow  $\sim 1.5^{\circ}\text{C}/\text{Ma}$ . In the period from Middle Jurassic until the Late Cretaceous, both the sample BG-38 and BG-62 were over buried and stayed in the PAZ. The distribution of short MTLs which range from  $11.15 \pm 0.20$   $\mu\text{m}$ , also reflects its cooling rate. On the contrary, the value for  $D_{par}$  is somewhat bigger about 1.66  $\mu\text{m}$ , compared to the others samples which show  $D_{par}$  values of  $\sim 1.3$   $\mu\text{m}$ , and a MTL about 12  $\mu\text{m}$ .





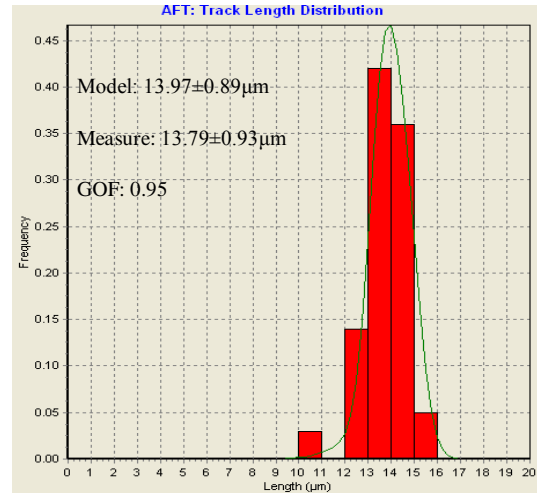
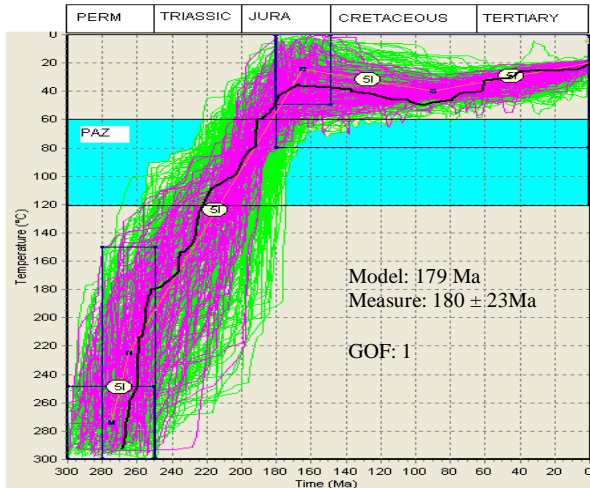
Fig. 4.8: Simplified geological map of the present study. Sample locations and their AFT ages are annotated (modified from the NGU geological map).

Sample	Rock Type	Elevation (m.a.s.l.)	Irradiation No.	No. of grains	(N <sub>s</sub> )	ρ <sub>s</sub> (x 10 <sup>5</sup> cm <sup>-2</sup> )	(N <sub>i</sub> )	ρ <sub>i</sub> (x 10 <sup>5</sup> cm <sup>-2</sup> )	(N <sub>d</sub> )	ρ <sub>d</sub> (x 10 <sup>5</sup> cm <sup>-2</sup> )	Central Age	P (χ <sup>2</sup> )	MTL ± 1σ (μm)	SD	No. of tracks	D <sub>par</sub>	No. of D <sub>par</sub>	U (ppm)	Error (%) on Central Age
<b>Footwall of HSZ</b>																			
BG-143	Gneiss	85	NOB-013	17	606	17.237	1004	28.558	10870	19.981	144.1 ± 10.7	4.13	NA	NA	NA	1.22	100	21.7	7,43
BG-144	Granodiorite	190	NOB-013	18	724	23.401	931	30.091	10870	19.354	179.9 ± 12	11.17	12.79 ± 0.16	1.58	100	1.36	287	23.7	6,67
BG-37	Tonalite	20	NOB-003	18	1636	39.623	2071	50.159	10250	17.457	165.3 ± 8.5	53.87	NA	NA	NA	1.45	95	40.2	5,14
BG-38	Augengneiss	10	NOB-003	21	2745	50.380	3158	57.960	10250	17.362	180 ± 8.4	34.43	11.15 ± 0.20	1.99	100	1.66	174	47.3	4,67
BG-61	Tonalitic gneiss	255	NOB-013	20	991	20.041	1570	31.750	10870	19.615	148.1 ± 8.2	93.17	NA	NA	NA	1.35	95	23.4	5,54
BG-62	Granite	455	NOB-013	10	921	57.013	1386	85.798	10870	19.667	156.3 ± 9.7	6.34	12.17 ± 0.18	1.84	100	1.30	234	69.6	6,21
BG-63	Porphyritic gneiss	35	NOB-013	19	526	10.441	759	15.066	10870	19.824	164.5 ± 13.9	2.77	NA	NA	NA	1.11	71	10.6	8,45
BG-66	Granodioritic gneiss	30	NOB-013	20	504	10.918	1112	24.089	10870	19.458	105.6 ± 7.9	8.35	NA	NA	NA	1.18	85	18.3	7,48
BG-91	Granite	45	NOB-013	16	1541	39.916	2117	54.836	10870	20.138	175.1 ± 8.9	41.66	NA	NA	NA	1.21	70	37.3	5,08
BG-117	Granodiorite	5	NOB-013	18	477	12.321	779	20.121	10870	19.406	142.2 ± 9.8	99.72	NA	NA	NA	1.33	115	14.5	6,89
BG-118	Gneiss	55	NOB-013	20	526	9.567	779	14.169	10870	19.563	156.4 ± 11.8	14.58	NA	NA	NA	1.23	100	11.1	7,54
BG-119	Tonalite	80	NOB-013	18	861	20.634	1306	31.299	10870	19.720	155.4 ± 9	61.84	NA	NA	NA	1.38	91	24.2	5,79
BG-120	Gneiss	20	NOB-013	20	194	2.676	371	5.117	10870	19.772	123.9 ± 11.9	97.33	NA	NA	NA	1.17	93	3.8	9,60
<b>Hangingwall of HSZ</b>																			
BG-31	Granite	15	NOB-003	22	579	7.068	675	8.240	10250	17.743	181.6 ± 12.3	87.18	NA	NA	NA	1.33	69	7.1	6,77
JN-01	NA	5	NOB-003	20	682	8.248	798	9.651	10250	17.933	183.5 ± 12.3	41.03	NA	NA	NA	NA	NA	7.4	6,70
JN-02	NA	40	NOB-003	21	641	7.244	687	7.763	10250	18.314	203.5 ± 13.5	92.13	NA	NA	NA	1.17	70	6.2	6,63
JN-03	NA	37	NOB-003	20	618	8.422	814	11.093	10250	18.218	165.2 ± 10.8	90.02	NA	NA	NA	1.20	100	8,7	6,54
JN-05	NA	10	NOB-003	20	680	8.197	826	9.956	10250	17.838	175.3 ± 11.2	68.58	NA	NA	NA	1.23	80	9.1	6,39
JN-06	NA	40	NOB-003	15	850	17.966	1018	21.516	10250	18.028	179.7 ± 10.8	42.35	9.32 ± 0.47	2.28	23	1.32	70	16.6	6,01
JN-07	NA	5	NOB-003	22	859	10.744	828	10.357	10250	18.409	227.4 ± 14.3	50.46	NA	NA	NA	1.15	95	7.8	6,29
BG-137	Diorite	10	NOB-013	20	1071	14.203	1804	23.924	10870	20.712	146.2 ± 9.3	1.27	NA	NA	NA	1.32	90	17.2	6,36
BG-138	Diorite	10	NOB-013	20	710	10.145	1009	14.418	10870	20.660	173 ± 12	7.39	NA	NA	NA	1.46	115	11.2	6,94
BG-139	Granodiorite	25	NOB-013	20	1397	20.009	1852	26.526	10870	20.608	185 ± 9.9	24.24	12.82 ± 0.15	1.51	100	1.33	275	20.3	5,35
<b>Hangingwall of BASZ</b>																			
BG-140	Granite	60	NOB-013	19	1266	22.018	1709	29.723	10870	20.556	181.6 ± 9.6	89.37	NA	NA	NA	1.27	95	20.7	5,29

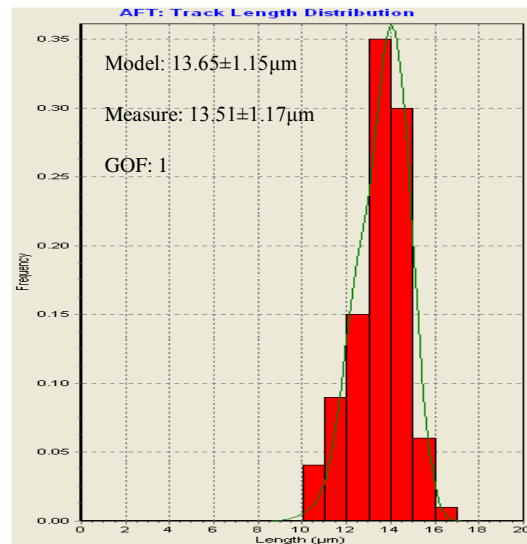
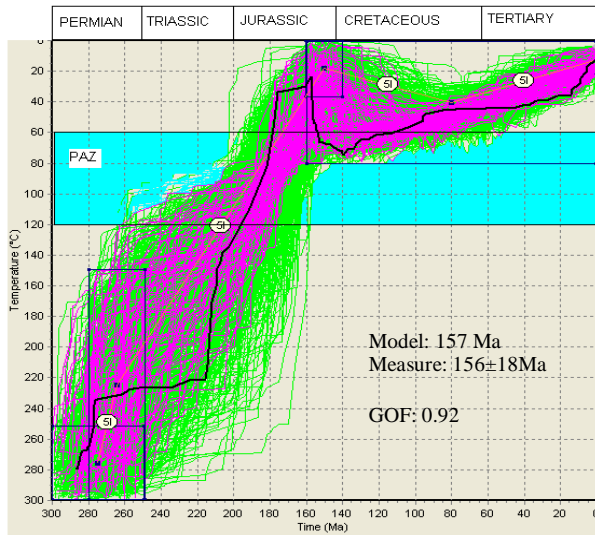
Tab. 4.2: Data of AFT ages following Hurford (1990 a, b) zeta approach. Abbreviations are ρ<sub>s</sub> : spontaneous track density, ρ<sub>i</sub> : induced track density, N<sub>s</sub> and N<sub>i</sub> are the counted numbers of spontaneous and induced tracks respectively, ρ<sub>d</sub> and N<sub>d</sub> are density and counted fission tracks on irradiated IRMM-540R glasses with 15 ppm U, P(χ<sup>2</sup>) is the chi-squared probability of a single grain's age distribution, MTL : Mean Track Length, SD: standard deviation of the MTL, D<sub>par</sub> is the mean etch pit diameter, U is the Uranium concentration.



### Sample BG-144



### Sample BG-062



### Sample BG-38

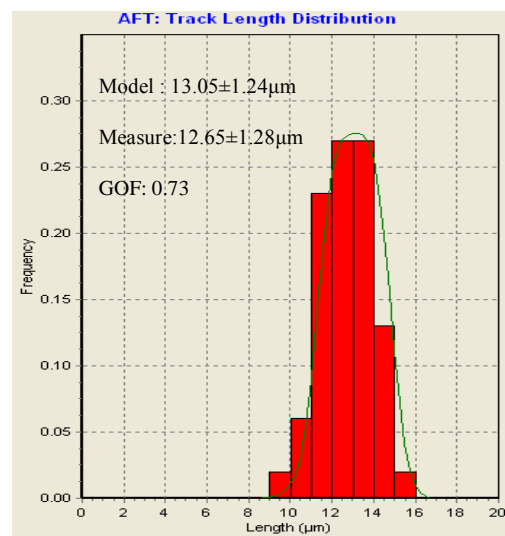
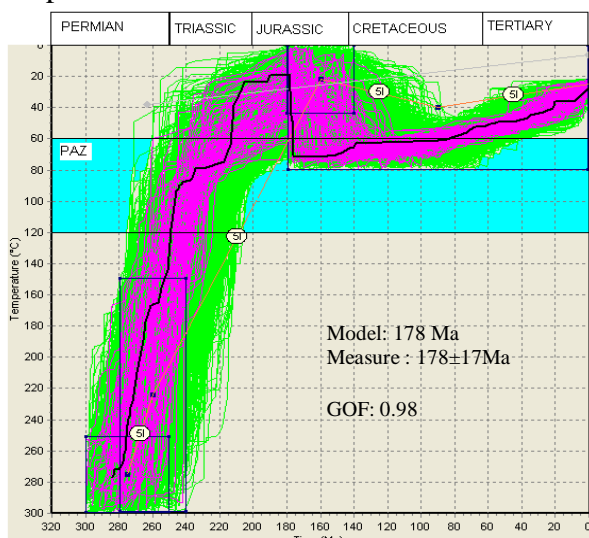


Fig. 4.9: Results of inverse thermal modeling from sample BG-144, BG-062 and BG-38. The thermal history model was modeled using HeFTy (Ketcham, 2005a). The black curve indicates the best fit path; the purple curves are the 100 good paths, whereas the green curves are all the acceptable paths. Range of the PAZ is signified in blue color; and the T-t constrains are marked by boxes; GOF is abbreviation of Goodness Of Fit.

#### 4.2.3.2 Hanging wall of the Hardangerfjord Shear Zone

In total 10 samples were taken from the hanging wall of the HSZ. They have AFT ages ranging from  $146.2 \pm 9.3$  Ma –  $227.4 \pm 14.3$  Ma, yet most of the ages are in the range of 180 Ma (Middle Jurassic) with a weighted mean age of  $174 \pm 12$  Ma (Middle Jurassic) (see Appendix VII). The age errors in this block is less than 7%, and contains only one sample which exhibits a  $P(\chi^2)$  less than 5 %. The U concentration is between 6-21 ppm. It seems that this range of U concentration is ideal to produce smaller error of age calculations. Additionally, the probability to count 20 good grains can easily be achieved. Two samples which were considered for modeling have a high U concentration i.e. JN-06 and BG-139. However, only 23 track length measurements could be taken from JN-06. In general, the values of  $D_{par}$  are between 1.15-1.46  $\mu\text{m}$  and the mean  $D_{par}$  is 1.28, a slightly smaller value than the samples from the footwall of the HSZ. The Mean Track Lengths (MTL) of JN-06 is  $9.32 \pm 0.47$   $\mu\text{m}$  and the  $D_{par}$  is 1.32  $\mu\text{m}$ , while the MTL of BG-139 is  $12.82 \pm 0.15$   $\mu\text{m}$  and the  $D_{par}$  is 1.33  $\mu\text{m}$ . Likewise in the BG-38, an inconsistency also occurs in the value of  $D_{par}$  and the MTL on sample JN-06. This contradiction will be discussed in the following chapter.

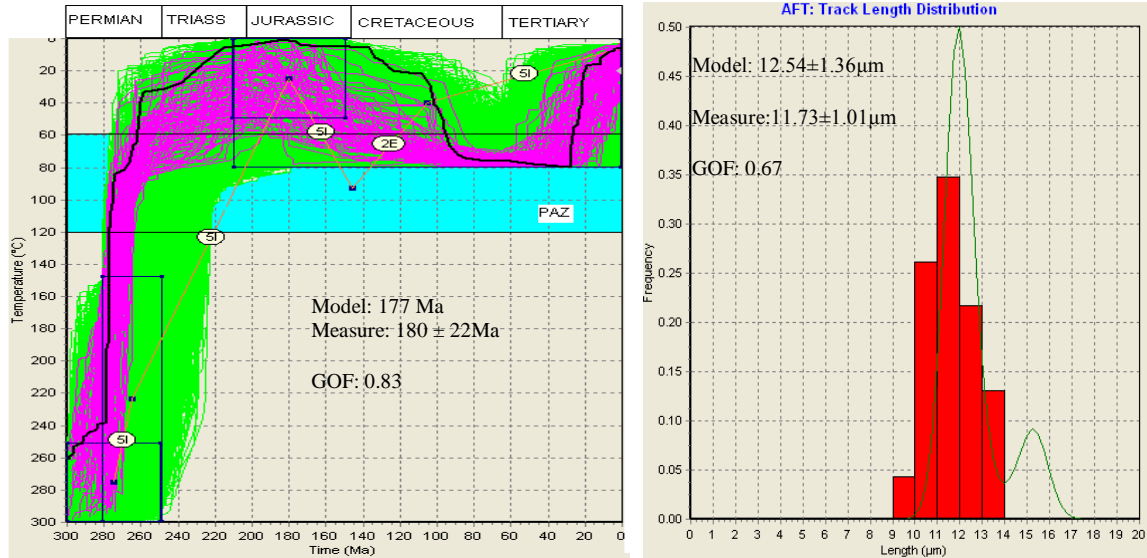
The inverse thermal history model for JN-06 is rather unreliable (Fig. 4.10). Besides the low number of MTLs, the thermal history model simulates and over estimates the MTLs in such a way (green line), that the long tracks dominate. It can be seen in the model that a very steep T-t path occurs within a short period during Permian time; while the real value of the MTLs is lower and short-moderate tracks dominate. The sample entered the PAZ after this period of rapid cooling, and it was initiated in the Middle Jurassic and ceased in the Tertiary.

A moderately rapid cooling phase for BG-139 started at about 210 Ma (the Triassic) and ceased around 190 Ma (Middle Jurassic). The cooling rate for this period is predicted  $3^{\circ}\text{C}/\text{Ma}$  (Fig. 4.9).

#### 4.2.3.3 Hanging wall of the Bergen Arc Shear Zone

Unfortunately, this block is only represented by one sample which is BG-140. Therefore, no thermal history modeling was performed. The AFT age is  $181.6 \pm 9.6$  Ma (Middle Jurassic) and  $D_{par}$  is 1.27  $\mu\text{m}$ .

(a) JN-06



(b) BG-139

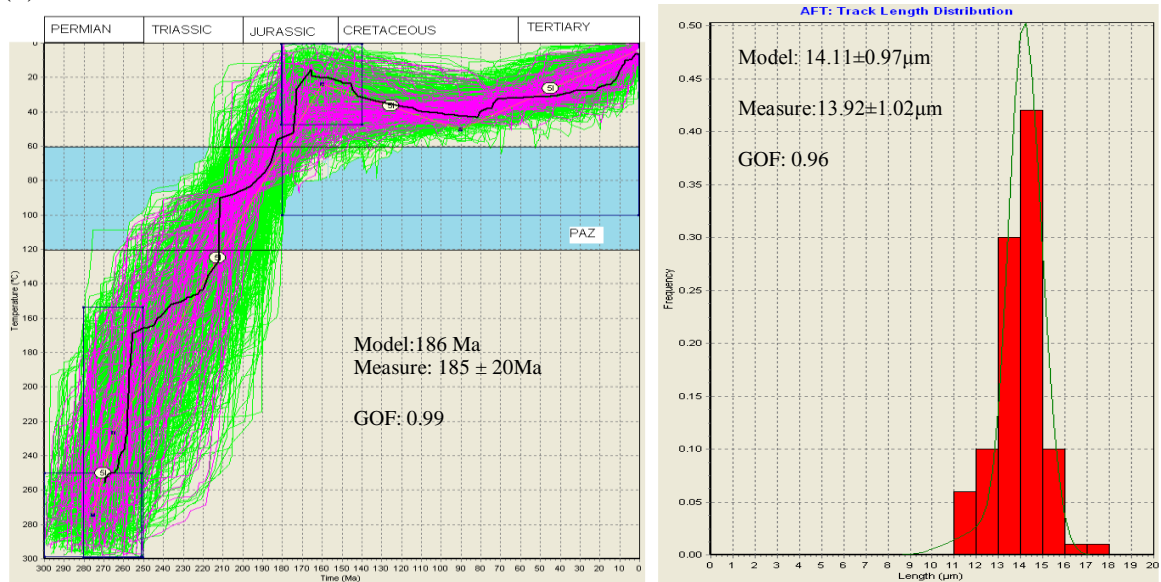


Fig. 4.10: Results of inverse thermal history modeling sample JN-06 and BG-139. The thermal history was modeled using HeFTy (Ketcham, 2005a). The black curve indicates the best fit path; the purple curves are the 100 good paths, whereas the green curves are all the acceptable paths. Range of PAZ is signified in blue color; and the T-t constrains are marked by boxes; GOF is abbreviation of Goodness Of Fit.

#### 4.2.4 AFT Diagrams

Several diagrams were constructed to see the trends and relationships between the parameters, such as a profile across the area vs. AFT age, elevation vs. AFT age, mean  $D_{par}$  vs. AFT age, MTL vs. AFT age, and MTL vs.  $D_{par}$ .

#### 4.2.4.1 AFT Age Variation along the Profile

The diagram demonstrates AFT age variations vs. distances along profile (Fig. 4.11). Major fault and shear zones are also illustrated in order to give a visual description of the AFT age variation between the two blocks. The sample locations which cross through the profile are directly plotted, while other samples located outer the profile have been projected. The line profile can be seen on the geological map.

The diagram below shows a distinct AFT age population between the two blocks of the fault. The age's population in the footwall HSZ (red lines with dots) is noticeably lower than those on the hanging wall (blue lines).

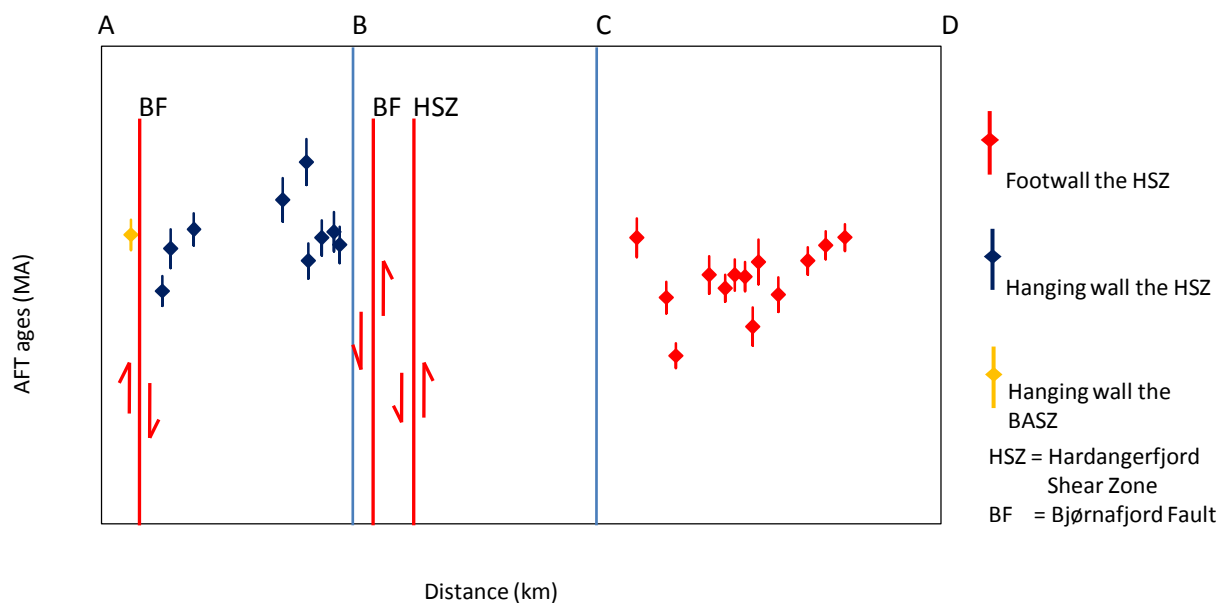


Fig. 4.11: Diagram shows distribution of AFT ages against distance along the cross section (Fig. 4.8).

#### 4.2.4.2 AFT Age vs. Elevation

Plotting of the AFT ages, either from the hanging wall of the HSZ or those from the footwall against elevation indicates that there is no correlation between those two parameters. Most of the AFT ages from the hanging wall were sampled at relatively low elevations (50 meter.). Therefore, a correlation is hardly observed. Plotting of AFT ages from the footwall shows a scatter pattern, whereas low-elevation (less than 100 meter) is associated with both young and old AFT ages, and moderate ages can be found at high elevation (Fig. 4.12).

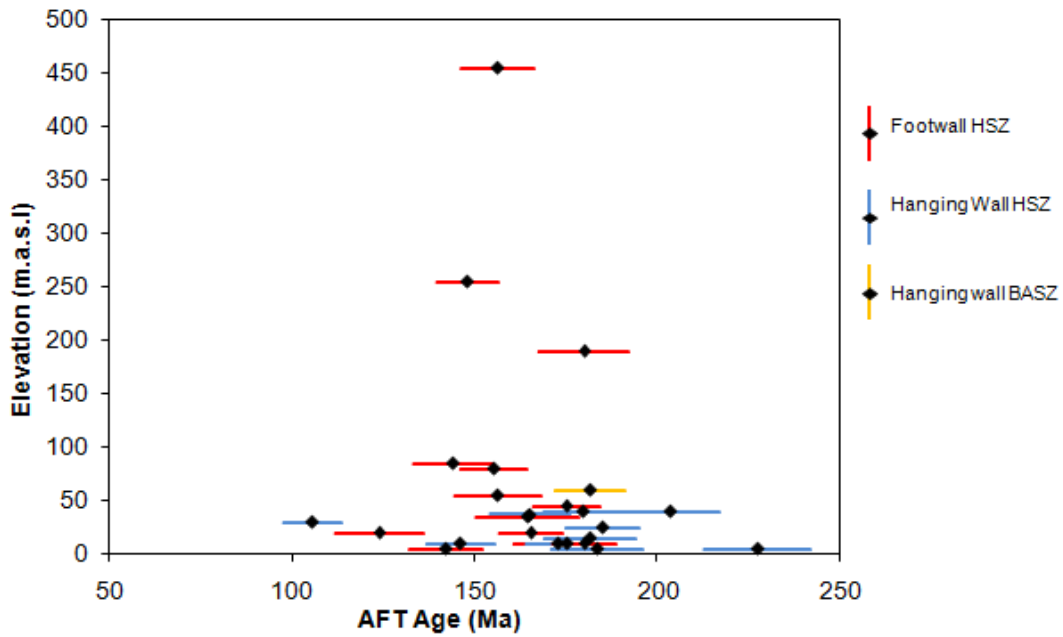


Fig. 4.12: Plotting AFT ages (Ma) against elevation (m.a.s.l). There is no correlation between these two parameters.

#### 4.2.4.3 AFT Age vs. Mean $D_{par}$

Plotting of the AFT ages against the mean etch pit diameter  $D_{par}$  indicates a cluster of AFT ages in the ranges of 150-175 Ma have a  $D_{par}$  around 1.2-1.5  $\mu\text{m}$ . In general, a good correlation is hardly observed in this diagram. An interesting feature is, whereas two oldest ages of hanging wall HSZ have  $D_{par}$  value 1.15  $\mu\text{m}$ , and on the contrary the two youngest ages of the footwall have a similar  $D_{par}$  value (Fig. 4.13).

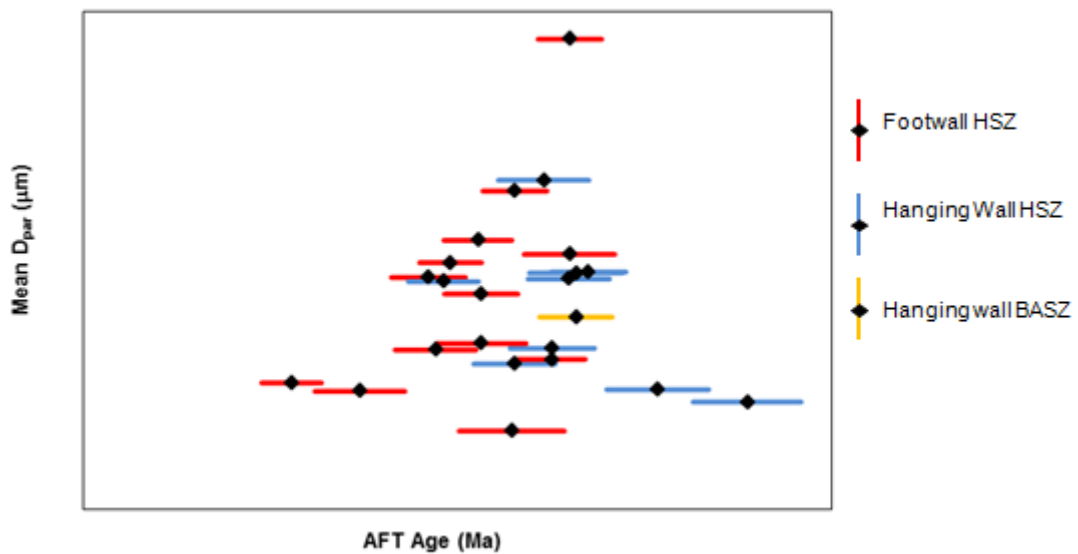


Fig. 4.13: Plotting of the AFT ages (Ma) vs. mean etch pit diameter  $D_{par}$  does not indicate any correlation.

#### 4.2.4.4 AFT Age vs. MTL

Plotting of MTL data from the footwall against the AFT age does not show any linear correlation (Fig. 4.14). Both of the similar AFT ages have different MTL values. MTLs originate from the hanging wall can hint that the older AFT age has longer MTLs and conversely, the shorter MTL belong to the younger age. Since only two samples were measured from this block, the hypothesis is rather weak.

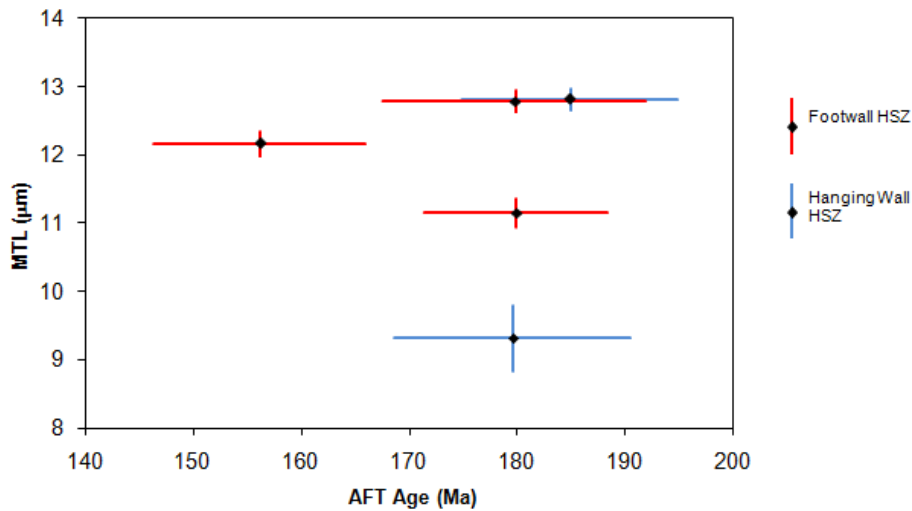


Fig. 4.14: Plotting of MTL against AFT ages generally does not exhibit strong correlation.

#### 4.2.4.5 MTL vs. Mean $D_{par}$

There is no significant correlation observed which describes the relationship between MTL against  $D_{par}$  value from the footwall. Plotting of those data from the hanging wall HSZ implies that samples with longer MTLs also have a higher mean  $D_{par}$  value and vice versa (Fig. 4.15). Unfortunately, only two measurements were provided, thus the argument is rather weak.

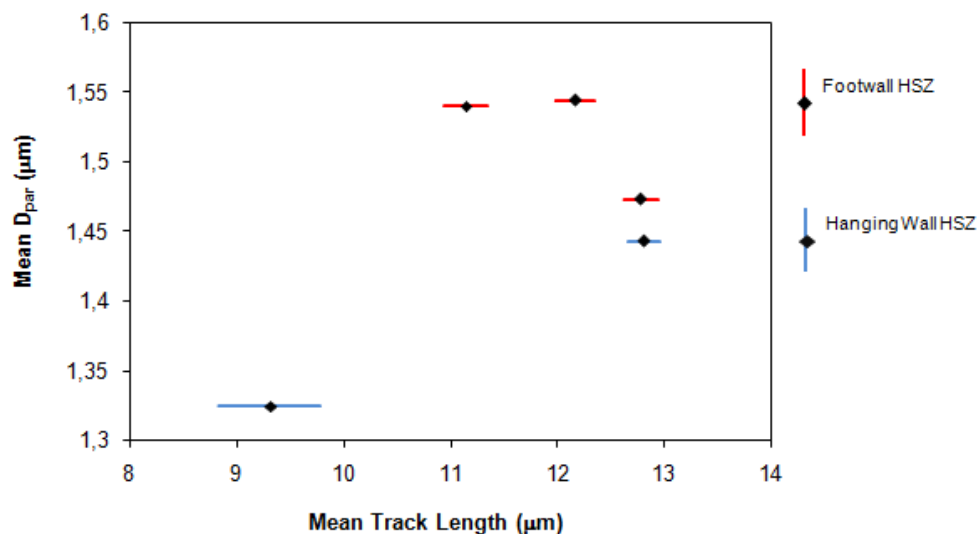


Fig. 4.15: Plotting MTL against mean  $D_{par}$  of the hanging wall shows a weak correlation due to limited data.

## 5. DISCUSSION AND INTERPRETATION

In this chapter, AFT ages including track length measurements,  $D_{par}$ , and the Zeta calibration are discussed. Also the five modeled inverse thermal history models will be discussed and compared to those of previous studies in the proximity of the present study (e.g. Magerholm, 2010; Tørresen, 2009; Johansen, 2008; Rohrman et al., 1995). At the end of this chapter, a possible exhumation history along the HSZ is proposed, based on the obtained AFT ages and the inverse thermal history models.

### 5.1 Interpretation of the AFT data

#### 5.1.1 AFT Ages

A minimum of 20 grains were selected to achieve good age measurements (Donelick et al. 2005). Most of samples 20 apatite grains could be counted, except for sample BG-62 which was only 10 grains counted due to a very high uranium concentration (close to 70 ppm). Therefore, the tracks are remarkably dense and hardly countable.

With 20 grains selected, and an assumption that 5 fossil tracks are encountered in each grain, hence the total number of spontaneous tracks will be 100. Roughly, the relative acceptable error generated on the pooled fission track would be approximately  $1/\sqrt{100} = 10\%$  (Donelick et al. 2005). This formula is unreliable because the acceptable error becomes smaller if the spontaneous tracks counted getting larger. Here, an error bar applied by Galbraith and Laslett (1985) shows a better constraint (see subchapter 3.9.1). The error is calculated from the central ages and also contains an error produced by the zeta value. From Tab. 4.2, all samples yield errors less than 10% that mean all errors are within the acceptable range.

The largest age error (9.6%) occurs in sample BG-120. This high error is most likely due to a very low uranium concentration (3.8 ppm). As already known, low uranium samples present a problem because of low induced track densities. In low uranium samples, an exact match between the areas counted in the grains and the mica is often hard to achieve. An adjustment by eye is difficult and subjective because the outline of the induced tracks on the mica does not reflect the shape of the analyzed grain.

In overall the errors do not show any systematic pattern. In many cases, the error becomes larger as the central age gets older. Other error sources probably originated from samples

containing high uranium concentration. Surprisingly those are not present in these samples. Even though, it was expected that samples with high U concentration will produce larger errors, because both the induced and spontaneous tracks were partly counted using reflected light to make counting process possible.

The  $\rho_d$  component also does not contribute significantly to the error of AFT ages. As shown in the Appendix VIII, plots of four  $\rho_d$  values from NOB 013 show less linear correlation with a linear regression of 0.36. However, those  $\rho_d$  values do not indicate any trend in the total fission ages error (Tab. 4.2).

The P ( $\chi^2$ ) test was carried out to measure uranium variations in the samples. A value of P ( $\chi^2$ ) larger than 5% means that the grains are assumed to be a single age. Here, all the AFT ages were calculated using the central age method and the radial plot; hence the age dispersions can be weighted (see Appendix V).

#### 5.1.2 Zeta Calibration

The weighted Zeta value used in this study is  $241.97 \pm 8.76$  with  $1\sigma$  error. The error is critical because this component of the Zeta will be utilized to calculate the AFT age (see subchapter 3.8.1). Therefore a large error in the Zeta leads to produce larger errors in the AFT ages. Ideally, the Zeta value gives contribution of 5-10% of the total error in the age's calculation. For accuracy reason, three unknown samples were examined using this Zeta. These unknown samples have been investigated beforehand by other co-workers for comparison. Otherwise, standard samples can also be used.

#### 5.1.3 Mean Track Length and $D_{par}$

Track length measurements were carried out for five samples; three samples from the footwall of the HSZ (BG-144, BG-37, and BG-62) and two samples from its hanging wall (BG-139 and JN-06). The samples were chosen due to their elevated uranium concentration. The minimum U concentration is about 20 ppm in order to achieve ~100 track lengths measurements. All of the samples meet this requirement except JN-06. For this sample, only 23 track lengths could be measured.

For length measurements, a source of potential bias derives from the decisions made by the analyst. The decision which track feature meets the criteria, and where the LED is being placed at both ends of the track are the most influencing factors.



The distribution of confined track lengths compared to the standard deviation of the MTLs can reveal the state of the thermal history. The majority of the crystalline basement rocks demonstrate a broad range of MTLs between 14 and 11.5  $\mu\text{m}$ . The basement data shows that as MTLs decrease, the standard deviation increases (Gleadow et al. 1986). The diagram below (Fig. 5.1) agrees with this assumption, except one of the MTLs which is below 11.5  $\mu\text{m}$  has possibly a more complex thermal history.

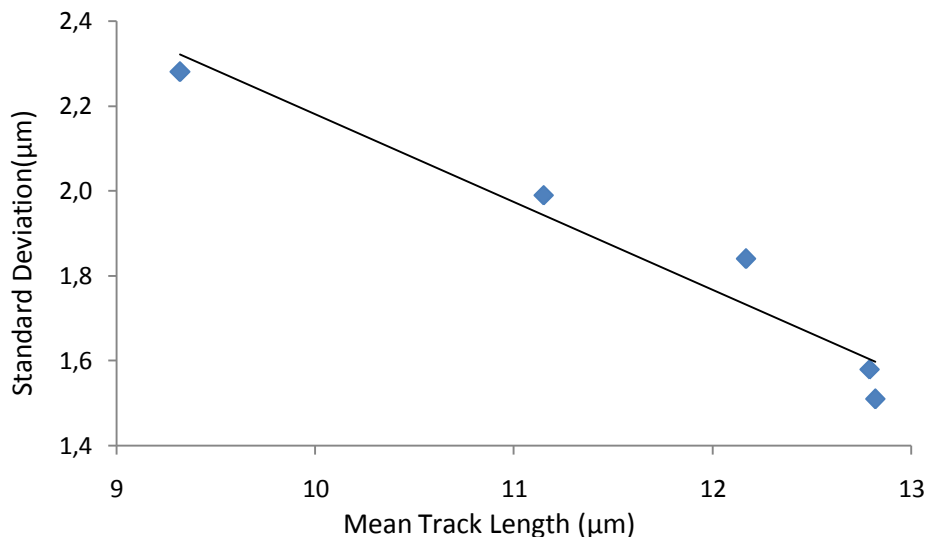


Fig. 5.1: The diagram shows a good correlation between the standard deviation against the mean track length (MTL). Increasing values of MTL are accompanied by decreases the standard deviation.

Measurements of etch pit diameters were carried out both the parallel ( $D_{par}$ ) and perpendicular to the  $c$ -axis ( $D_{per}$ ). However, the values of  $D_{per}$  are ignored because of imprecise measurements reasons. It is unlikely to obtain an accurate measurement of  $D_{per}$  using an optical microscope with the magnification which was used in this study.

The values for  $D_{par}$  are dominated by low values in the range of 1.11-1.66  $\mu\text{m}$ . Carlson et al. (1999) affirmed that  $D_{par}$  value less than 1.75  $\mu\text{m}$  anneals rapidly, which is also typical for the near-end-members calcian-fluorapatites. The fluorapatite member has been known to be less resistant to anneal than Cl-apatite (Gleadow & Duddy, 1981).

Fission track annealing kinetics can be measured by several parameters; one of them is  $D_{par}$ . By measuring  $D_{par}$ , other parameters can be predicted, because  $D_{par}$  is positively correlated with Cl wt% and OH wt% and negatively correlated with F wt% in apatite (Donelick, 1993; 1995 and Burtner et al. 1994). Experiments by Carlson et al. (1999) and Donelick et al. (2005) give evidence that a  $D_{par}$  value less than 1.75  $\mu\text{m}$  has Cl content almost 0 wt%. According to

Ketcham et al. (1999) the fission tracks with  $D_{par} = 1.5 \mu\text{m}$ ,  $Cl = 0 \text{ wt}\%$ , experience a total loss of tracks at around  $100\text{-}110^{\circ}\text{C}$  in the geological environment. Hence, it can be inferred that these samples approximately have the properties of low Cl and OH, high F content, annealing rapidly and probably typical for calcian fluorapatites.

#### 5.1.4 Comparison of AFT Ages vs. Elevation

Studies that correlate AFT ages collected on high relief mountain belts have been investigated by Wagner & Reimer (1972), Wagner et al. (1977). Their studies showed that there is a positive correlation between those two parameters. In practice, the positive correspondence is not always evident, as in this present study. It is expected that the older AFT ages derive from high elevations and the young AFT ages from the low level. However, both the young and older fission track ages come from low elevation, whilst some of the moderate AFT ages are from high elevations (Fig. 4.12). One of the reasons may be because the difference of elevations are not significant, as most of the samples are located in the range of 5-85 m.a.s.l., and only few are below 455 meter.

No correlation between AFT ages vs. elevation can occurred due to several factors. It is defined as follows:

- Commonly the fission age over high elevation about 1000-2000 meter has been interpreted as the result of high rates of erosion. However, cooling can be occurred devoid erosion process but rather by tectonic which is called tectonic denudation. A study case from shear zone and detachment faults shows this variation (Galagher et al., 1998).
- Gradient geothermal is influenced by topographic relief. As already known that the gradient is higher under a valley than under mountain peaks. Even though magnitude of the effect decreases with increasing depth, but it is still significant in the low-thermochronological method, in which generates overestimate the true rate of erosion (Mancktelow & Grasemann, 1997).
- A vertical profile of samples cannot directly give a correlation of elevation-AFT ages if the areas have been rotated after cooling (Galagher et al., 1998)
- A positive correlation between AFT age and sample elevation can be found if erosion on the surface is responsible for denudation (Fitzgerald et l., 1995).
- A study case in western USA reveals a poor correlation between apatite age and elevation. This probably occurred because topographic forms in response to isostasy,

which is controlled by the position, amount and timing of removal of crust at depth along the extensional fault (shear zone or detachment) and not by erosional process (Block and Royden, 1990).

#### 5.1.5 Comparison of AFT ages and annealing kinetic parameters

Plotting of MTL data against AFT ages (Fig. 4.14) does not display any correspondence. Theoretically, by referring the fission track age equation, there is implicit an assumption of a proportional relationship between the true mean length of fission tracks and their track density in an isotropic medium (Laslett et al., 1984). Consequently, short tracks will be followed by decreasing track densities, and thereby young fission ages. However, the MTL data seems to be plotted randomly, except a very weak positive correlation is present from the hanging wall of the HSZ but still bears uncertainties due to limited data. A number of factors can be explained as follow:

- An experiment was carried out by Gleadow and Duddy (1981) concluded that the average length of confined tracks is reduced by about 15% before there is any reduction in the fission track age. In a simple way, the reduction trend does not show a 1:1 relationship. A succession experiment also give a similar result (Laslett et al., 1984; Green, 1988) concluded that the proportionality of track length reduction and tracks density only prevails on an isotropic medium. Anisotropic processes are visible in fading stages, whereas tracks parallel to *c*-axis are most resistant to shorten; tracks perpendicular to *c*-axis are least resistant to annealing.
- The anisotropy of apatite is controlled by the structure and chemistry of the apatite crystal, thereby reflects different annealing rates. A study from Barbarand et al. (2003) revealed how compositional variation influence apatite crystal structures and fission track annealing. High Cl content leads to the more resistant tracks to shorten, thus the long MTL dominates. For samples with very low Cl values, substitution of LREE (i.e. Ce and La) is responsible for different FT annealing responses. Commonly increasing LREE results to least resistant tracks to anneal, thus most of the tracks are short.
- A failure of a positive correlation between the AFT ages and the MTL occurred because the track length is determined rather by the thermal history than the fission track ages. This occurs remarkably in multiple cooling histories, whereas

the pre-existing tracks will be shortened in significant time. If cooling histories are more complex thus also produce more complex length distributions (Gleadow et al., 1986). This situation is further explained in the subchapter 5.2.

The etch pit diameter can also assess the annealing rate. The MTL is actually a mirror of the etch pit diameter. Therefore, an increase in the etch pit size will be reflected in the increases of the MTL (Barbarand et al., 2003). A kinetic parameter of Cl content can be resolved by values of the etch pit size. It has been mentioned (subchapter 5.1.3), that small sizes of  $D_{par}$  reflect low values of Cl.

Since the diagram of AFT ages against MTL fails to show a positive correlation, and that  $D_{par}$  shares a kinetic parameter with the MTL, as a consequence the  $D_{par}$  displays no correlation with the AFT ages.

## **5.2 Evaluation of the Inverse Thermal History Model**

With respect to inverse thermal history modeling, the relation of fission track ages to the closure temperature is sensible when no significant annealing occurred after closure temperature time was reached. It means that in a bimodal distribution of MTL, a fission track age does not reflect the timing of the closure temperature. It can be obviously seen in sample JN-06. This sample experienced a rapid cooling during 280-260 Ma, and subsequently entered the PAZ about 90-30 Ma. Meanwhile, the fission track age is calculated and modeled at 177-180 Ma, which is beyond the closure temperature range of 120<sup>0</sup>C when the fission tracks start counting (Fig. 5.2). Therefore, information from the track length measurements is important to understand the cooling history.

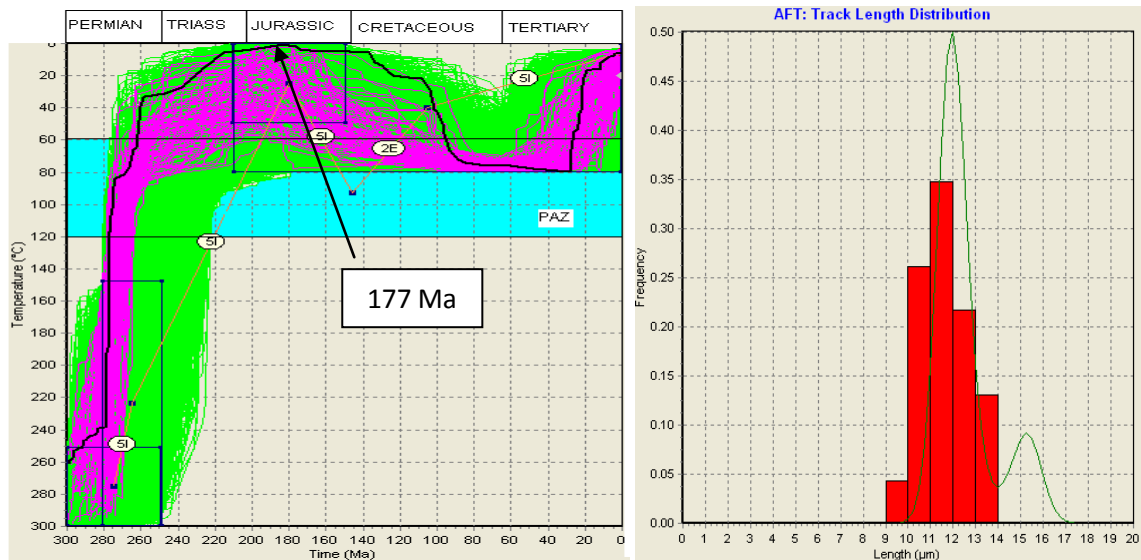


Fig. 5.2: Sample JN-06 experienced rapid cooling in the Permian and resided in the PAZ for second times during the Cretaceous-Tertiary. The AFT age of 177-180 Ma (annotated) is located beyond the PAZ.

The inverse thermal history model of JN-06 is also rather unreliable due to limited length measurements. It can be seen on the GOF of the T-t path which is 0.83 and the one of the MTL which is only 0.67. A bimodal pattern of the MTL does not appear from the measurements, but it is very significant from the model (green curve) which indicates two patterns of PAZ occurred. This pattern is called the partial overprinting model. In this situation, all the tracks which formed in the first PAZ will be shortened simultaneously. Tracks accumulated at relatively low temperature after the later stage will be longer than the previous one, resulting two peaks of track length distribution (Gleadow et al., 1985). This pattern is classified as *mixed ages* by Wagner (1972). A bimodal distribution in some cases will be formed depend on how long the tracks are subjected of annealing in the latter stage. If the pre-existing tracks are not annealed sufficiently (i.e. short time), the two component track lengths will merge to form a unimodal type but rather broad with moderately short tracks dominating and lesser frequencies of long tracks (Gleadow et al., 1985). This pattern is distinctly illustrated in BG-62 and BG-38 (Fig. 5.3). A broadness of track length distribution and its frequency depends on how long a sample stays in the PAZ. The sample BG-38 stayed longer in the PAZ than BG-62; thereby the length distribution is wider and has a lesser frequency of long tracks.

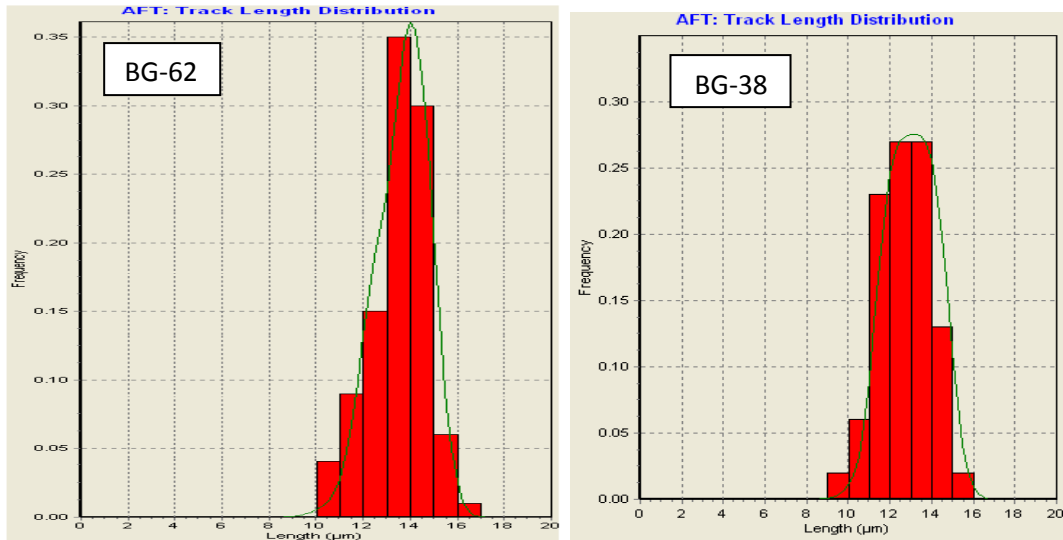


Fig. 5.3: Track length distributions for sample BG-62 and BG-38 show unimodal type but broader with short track lengths rather dominate.

Both sample BG-139 and BG-144 were subjected of one rapid cooling stage. The track length distribution is characterized as unimodal and narrow with long tracks predominate. Theoretically, a fission track age will be recorded once the samples are within the PAZ range. However, this concept is valid only if the sample cooled linearly through the PAZ, or cooled so rapidly without significant amount of time in the PAZ (Gleadow et al., 1985). In both the samples BG-139 and BG-144, the ages are beyond the timing when the samples resided in the PAZ (Fig. 5.4). This occurred due to non-linearly cooling when the samples are through the PAZ. Additionally, sources of uncertainty among others are the determination of the PAZ, the uncertainty in the initial track length and the poor quality of length measurements (Ketcham, 2005). Therefore, the inverse thermal history model should not be considered as an absolute approach but rather as an estimation of the hypothesis.

Denudation in terms of its causal is classified by two; surface process that is erosion and by tectonic events whereas the crust is thinned by extension (Johnson et al., 1997). It is possible to distinguish a responsible factor of the denudation by means of fission track analysis. If surface process is only factor responsible for the denudation, then a progressive decrease of the AFT age is comparable as denudation proceeds towards the PAZ. A surface-cause denudation is also characterized by a gentle gradient cooling history (Johnson et al., 1997). In contrary, denudation caused by tectonics is distinguished by a lack correlation between AFT ages against elevations.

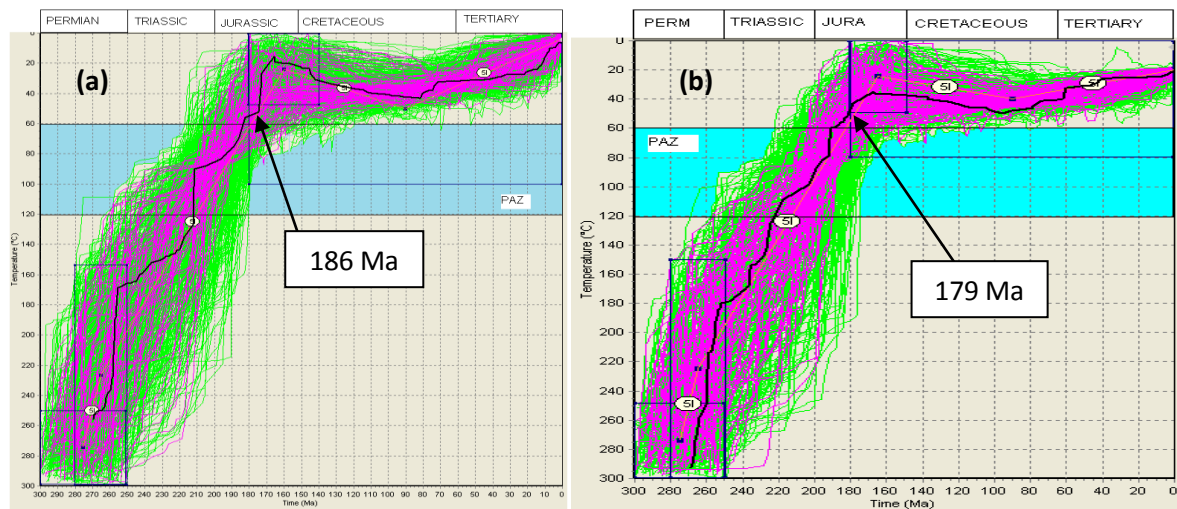


Fig. 5.4: Both sample BG-139 (a) and BG-144 (b) show plotting the AFT ages beyond the PAZ, which presumably due to several factors; the cooling rate is rather slow thus the samples stayed longer in the PAZ, oversimplified of the PAZ values, uncertainty in the initial track length.

Typical for tectonic denudation is also indicated by a very steep gradient of the cooling history experienced by many footwall rocks (Johnson et al., 1997). A very rapid cooling mainly occurs subsequently due to volcanic activity or hydrothermal activity (Duddy et al., 1998), dyke emplacement, faulting or meteorite impact (Miller & Wagner, 1979).

Most of samples display a moderate-steep gradient of cooling history and a negative correlation between the AFT age and altitude. It is predicted that tectonic force might be a main cause of the denudation. The moderate gradient of cooling history is probably a result of tectonic and erosion denudation which act together.

The samples of BG-062 and BG-38 (Fig. 5.5) resided in the second PAZ at the Middle-Jurassic-Middle Cretaceous, while sample JN-06 (Fig. 5.2) stayed in the PAZ at the Late Cretaceous-Tertiary time. This event is interpreted as a burial event coeval to the period of transgression and deposition of sediment clastics and carbonates from the offshore at Middle-Late Cretaceous (Doré, 1992; Riis, 1996). In addition, this hypothesis was also supported by Fossen et al. (1997) who had evidence of recrystallization of fractures and microbreccias in the gneiss adjacent the Bjørøy Formation. It means that the formation has been located at about 5 km depth during the latest Jurassic (Fossen et al., 1997). However, sample BG-144 and BG-139 do not show a transgression and burial event. Both samples only exhibit rapid cooling in the Triassic (Fig. 5.4). It is surprising, because the cooling history is expected shows at least a similar pattern, since the locations are nearby. It might be because the thermal history model is sensitive to the input of various kinetic parameters. Meanwhile, the kinetic

parameters depend on the chemical properties such as chlorine content which influence annealing rate. Therefore, applying value of the PAZ ( $120^0-60^0\text{C}$ ) to all samples is oversimplified.

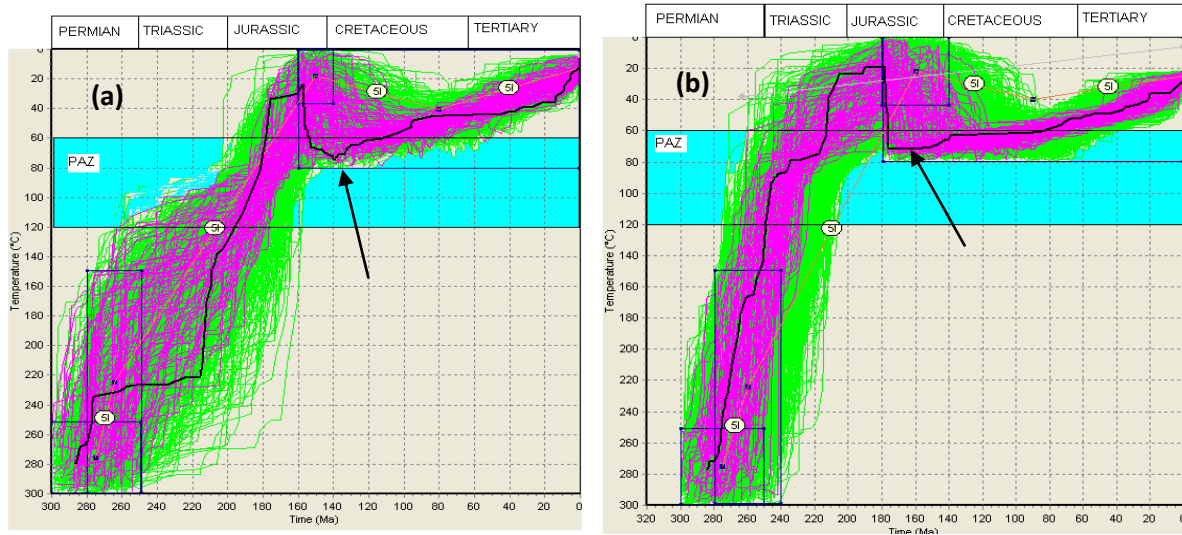


Fig. 5.5: Both the sample BG-062 (a) and BG-38 (b) resided in the second PAZ after experienced a rapid cooling. This event is interpreted as a burial event coeval to the period of transgression and deposition of sediment clastics (Doré, 1992; Riis, 1996).

### 5.3 Movement of Faults

The Hardangerfjord Shear Zone is a NW-SE trending ductile structure which runs parallel to the Caledonian orogenic belt. The zone has been reactivated since it formed at about 408-402 Ma (Fossen & Dunlap, 1999). Since its development, the HSZ progressively deformed more brittle, which indicated that the zone was exhumed toward the upper crust. The brittle Lærdal-Gjende fault system was subsequently formed and overprinted the ductile HSZ in the Lærdal area, northeastward the present study. Dating using Rb/Sr revealed the event occurred at ~367 Ma (Scharer, 1980). A subsequent development is the formation of N-S to NNW-SSE trending faults which occurred in the Permian (Fossen & Hurich, 2005; (Færseth et al., 1995). The Jurassic extension was represented by NNE-SSW trending faults (Færseth, 1996). By applying apatite fission track analysis, it is expected that the fault reactivation in the upper crust could be detected.

The weighted mean of AFT ages from the footwall of HSZ is  $145 \pm 16$  Ma (see Appendix VI) which is within the range of Late Jurassic – Early Cretaceous time. This average AFT age indicates that the footwall of HSZ was reactivated during these times. According to Færseth (1996) the Jurassic rifting event was expressed by NNE-SSW trending faults. Plotting the



fault planes (Fig. 5.6) from the footwall rather displays pronounce of the NE-SW trending of the HSZ. Other trend directions are N-S and NW-SE which probably reflect Permo-Triassic rifting. The various trend patterns of joint planes are present; though the apparent extension trend of ESE-WNW can be identified and reflect both the Permo-Triassic and the Jurassic rifting event (Fig. 5.6).

The hanging wall of the HSZ also acted as the hanging wall of the Bjørnafjord Fault. Considering the apatite abundances, most of the data and samples collection was obtained from the hanging wall of this fault, not directly from the hanging wall of the HSZ.

The Bjørnafjord Fault formed during the Devonian and is likely of one generation with the HSZ. Up to now, this fault gets little attention in the literature, thus no information can be referred except from the geological map (published by NGU). The fault has the mean AFT age of  $174 \pm 12$  Ma, which means that the fault was reactivated during Middle Jurassic time. Fossen (1992, 1993) documented microfolds, shear bands, asymmetric boudins which indicate down-to-NW movement of the Caledonian allochthon. This movement is recorded in the study area only from foliation data which was collected from both the hanging and the footwall.

The subsequent movements documented are E-W, NW-SE, and a minor NNW-SSE trending direction. The Bjørnafjord Fault runs around Stord and Tysnesøya and is terminated in Austevol. Hence, the fault shows a curving shape. The E-W, NW-SE fault direction was likely affected by the regional trend of the Bjørnafjord Fault. However, the time constraint of these faults is unknown, but probably formed after the Devonian. The NNW-SSE fault direction could be produced either by rifting in the Permo-Triassic or be exerted by the main fault of the Bjørnafjord Fault.

Plotting of joint planes from the hanging wall does not show a significant trend. The high frequencies of the joint poles are scattered, yet the NW-SE and NNE-SSW extension direction can be resolved (Fig.5.6). The NW-SE extension orientation might be formed at Pre-Triassic or Devonian time (Valle et al., 2002; Fig.4.2). Hypothesis about the NNE-SSW extension has been discussed in 4.1.1. The ESE-NNW Jurassic and Permo-Triassic extension direction is however not prominent in the hanging wall. In summary, the Jurassic reactivation is not preserved in term of fault data and that the paleostress (fracture analysis) of the study area is in accordance to what resulted by Valle et al. (2002).

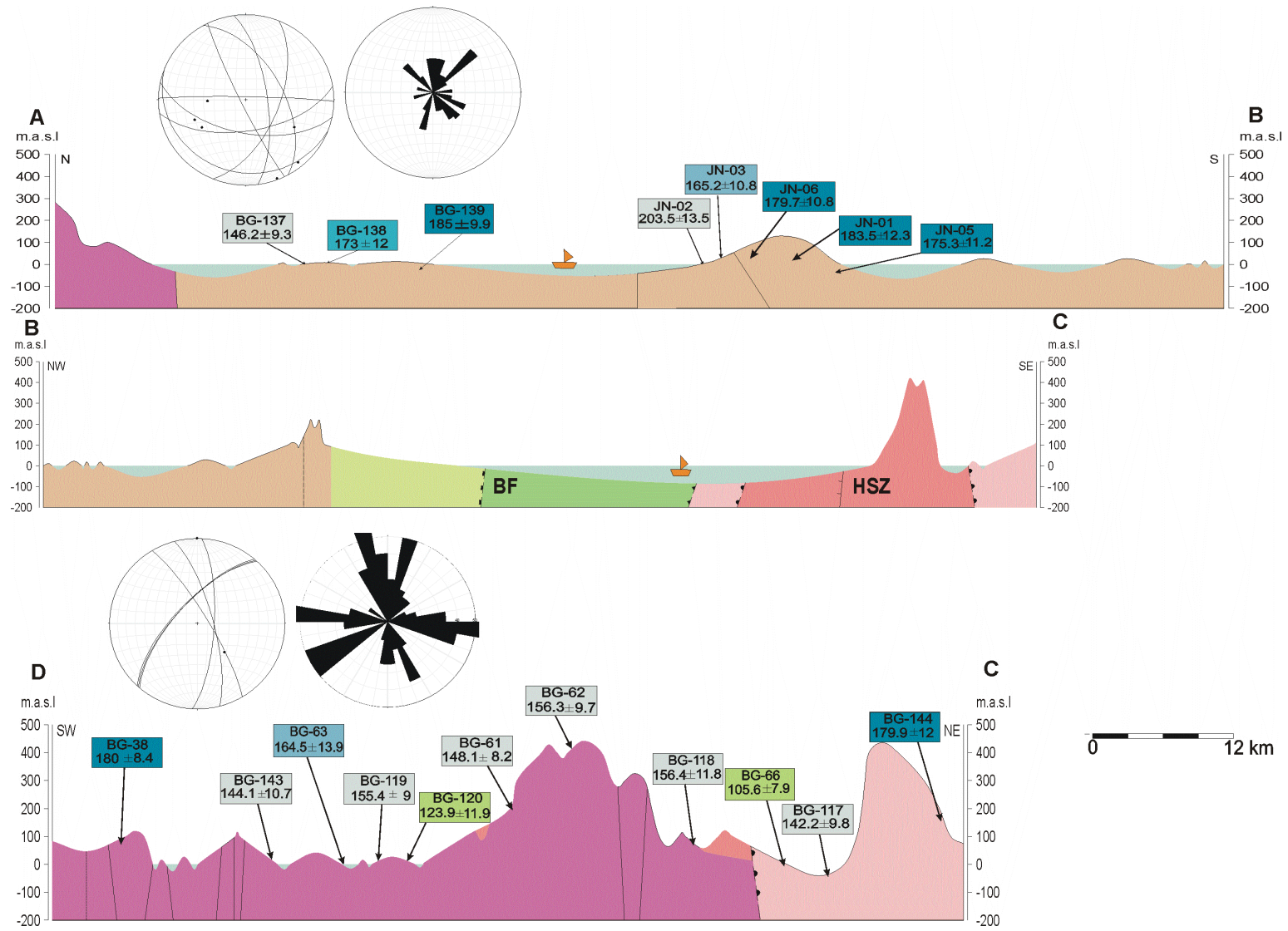





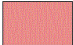

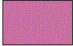


Fig. 5.6: (Previous page). Samples location and AFT ages are plotted onto profiles. The structural measurement of joints and faults are also indicated in equal stereographic projection. Profile A-B is area in the hanging wall of the HSZ, profile B-C is crossed the HSZ and BF, profile D-C is area in the footwall of the HSZ.

#### LEGEND OF LITHOLOGY

	ORDOVICIUM LANGEVOG GROUP		EARLY ORDOVICIUM ROCKS
	EARLY ORDOVICIUM TORVASTAD AND SIGGJARD GROUP		PROTEROZOIC LOWER ALLOCHTHONOUS
	ORDOVICIUM ROCK		KAMBRIO-SILUR BASEMENT
	MID ORDOVICIUM-SILUR SUNNHORDLAND GROUP		PROTEROZOIC BASEMENT

#### LEGEND OF AFT AGE

	EARLY CRETACEOUS		EARLY JURASSIC
	LATE JURASSIC		LATE TRIASSIC
	MIDDLE JURASSIC		MIDDLE TRIASSIC

## 5.4 Comparison to Previous Studies

Rohrman et al. (1995) collected and analyzed samples from the Eidfjord, Jotunheimen, Hunnedalen, and Gausta in southern Norway. The cooling events are divided by two distinct periods; the pre-and the post-Cretaceous cooling. Most of the samples were subjected to Pre-Cretaceous cooling, precisely Triassic-Jurassic cooling with a rate of  $\sim 2\text{-}2.5^{\circ}\text{C}/\text{Ma}$ . This cooling event was initiated at  $\sim 225$  Ma coincided with the progradation of major deltas from the Norwegian mainland (Doré, 1991; Steel, 1993) and a major phase of rifting in the North Sea (Ziegler, 1990). Rohrman et al. (1995) interpreted that the Triassic-Jurassic cooling is erosional combined with tectonic rift flank uplift. This hypothesis is corroborated by accumulating of coarse clastics deposition in the Fennoscandian offshore during these times. The post Cretaceous cooling event is in fact not pronounce, whereas only one sample (JOT 17) displayed slow cooling during Paleogene-Neogene time. A correlation of similar AFT ages forms AFT isochrons. The distribution of the AFT isochrons and the plotted AFT ages in cross sections display a domelike shape (Fig. 5.7).

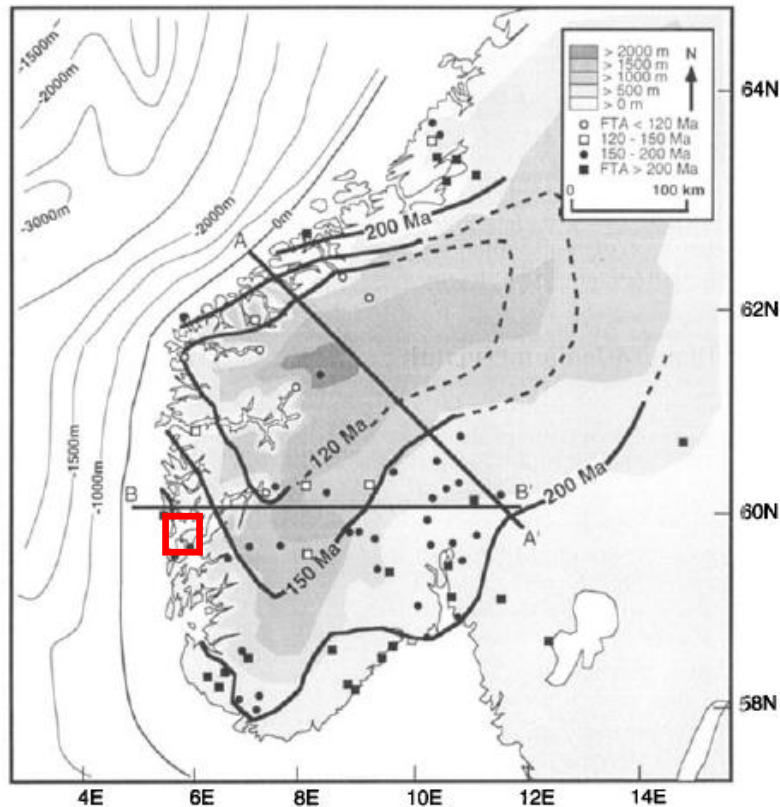


Fig. 5.7: The AFT ages plotted onto a topographic map. Fission track samples are labeled according to age (Rohrman et al., 1995). The red box indicates the present study area.

Analysis carried out by Rohrman et al. (1995) exhibits slightly similarities in the timing of rapid cooling to the one of the present study, namely the late Permian-Jurassic (250-180 Ma). However the Paleogene-Neogene slow cooling event is not present, instead of the Cretaceous event. The range of AFT ages in the present study (200-150 Ma) is comparable to the AFT isochron shown by Rohrman et al. (1995) (red box in the Fig. 5.7). In addition, analysis of thermal history modeling from the Sotra area yields cooling events that occurred since the Permian until the Jurassic (Johansen, 2008). A similar cooling time at the Permian-Jurassic time results from the Hardangerfjord Shear Zone, northeastward of the present study (Magerholm, 2010). A different cooling history of Øygarden and Masfjorden area (north of Sotra) yields cooling ages at the Devonian until the Jurassic (Tørresen, 2009).

Rohrman et al. (1995) estimated as much as 1.3-3.5 km of overburden that was removed during the Triassic-Jurassic. Tørresen (2009) calculated the exhumation rate of the Øygarden and Masfjorden area is  $\sim 9$  m/Ma. If it is assumed as in Rohrman et al. (1995) that the geothermal gradient during Triassic-Jurassic was  $35^{\circ}\text{C}/\text{km}$ , then a similar value of overburden can be produced namely 1.7-3.5 km and an exhumation rate during 250-180 Ma is 27-13 m/Ma. These numbers are approximations and depend on the values of geothermal gradient.

Distributions of AFT ages from the HSZ, northeastward to the present study area shown by Magerholm (2010) can be compared to observe a trend of fission track ages away from the offshore (Fig. 5.8). The AFT ages presented by Magerholm (2010) are fairly good except two data exhibit significant errors; thereby they were excluded from analysis and discussion (Fig. 5.8). The footwall of the HSZ in the present study yields a weighted mean of AFT ages of  $145 \pm 16$  Ma (subchapter 4.2.3.1). Meanwhile, the weighted mean of AFT ages from Magerholm's area is  $156 \pm 14$  Ma (see Appendix IX). This mean value is calculated from 8 AFT ages in the footwall, regardless one sample of TM-15 which displays too large error.

The trend of older AFT ages toward inland is interesting. A similar trend of increase the AFT ages inland is also observed from the hanging wall. The weighted mean of the hanging wall in the present study is  $174 \pm 12$  Ma. By calculating a weighted mean of three AFT data from Magerholm (2010) and excluding two of them yield of  $183 \pm 34$  Ma (see Appendix X). The two ages were omitted due to a large error, and the others display very young ages probably due to heat transfer from fluids circulating within the fault zone (Malusa et al., 2009).

The differential distributions of the AFT ages can be explained as follows: (1) the rift centre located closer to the present study, thereby away from the coastline, the rift flank is less exhumed than the one close to offshore; (2) differential rate of erosion could also lead to the varying AFT ages; (3) differential movement or tilting of the HSZ blocks. However, since the Magerholm's area also displays negative correlation of elevation against AFT ages, it is implied that the first and third hypothesis is more likely. Færseth (1996) identified that there is a difference in the distribution of stretching and structural expression in the Viking Graben during Jurassic times. This is probably responsible to the tilting of the HSZ blocks, as it seen in the distribution of AFT which tends to decrease inland.



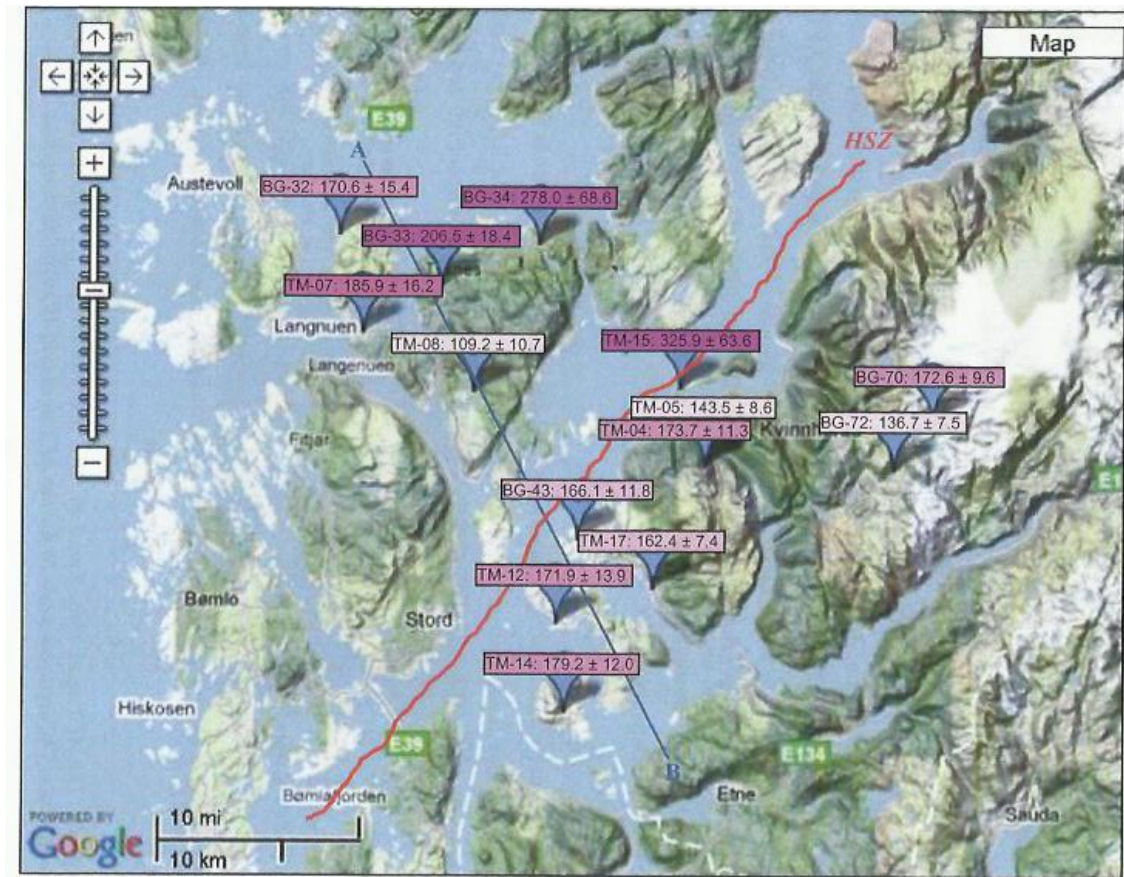


Fig. 5.8: The AFT ages are plotted onto a topographic map of the Hardangerfjord area. The red line annotated is a Hardangerfjord Shear Zone (Magerholm, 2010).

### 5.5 Proposed Exhumation History of the HSZ

The causes of uplift flanks or shoulders of rifts are due to thermal processes or other sources of buoyancy in the subsurface. The mechanisms of rift flank uplift are: (1) lateral conduction of heat from the region of extended lithosphere to the flanks; (2) heat transferred from beneath the rifts to the flanks by small scale convection; (3) magmatic thickening (underplating) of the rift flank crust due to partial melting in the underlying mantle (Weissel and Karner, 1989, and references therein). Asymmetric geometry of the rift flanks is built by normal faults which form along deeply penetrating detachment faults.

The successive events of rifting in the Norwegian Sea influence and effect the rift flanks which are constructed by series of normal faults and shear zones. The HSZ extends SW-NE from the Norwegian Sea to the rift shoulder of the Norwegian passive margin. The development of the HSZ and other faults in the rift flank are associated with the state of stress

in the basins, thus ultimately induces uplift or subsidence to the rift flank (Kooi and Cloetingh, 1992).

The HSZ formed after the reactivation of the Caledonian basal detachment zone (Mode I). The crustal collapsed by development of W and NW dipping extensional shear zones (Mode II) in which major extensional shear zones namely the HSZ, the Bergen Arc Shear Zone (BASZ), and Nordfjord-Sogn Detachment Zone (NSDZ) formed (Fossen, 2000). The late stage of Mode II has been reported occurred at about 415-416 Ma, based on  $^{40}\text{Ar}/^{39}\text{Ar}$  thermochronology of muscovite from the NSDZ (Dunlap and Fossen, 1998). Færseth et al. (1995) suggested that the allochthonous on the footwall probably has been removed and filled the hanging wall basins since Devonian times. The loading of this deposit on the hanging wall ultimately led to increase the footwall uplift. At that time, the Precambrian basement has been peneplained during the late Proterozoic and covered by latest Proterozoic to Ordovician sediments, which are found as psammitic units in the lowest nappes (Bockelie and Nystuen, 1985) (Fig. 5.9a).

The brittle deformation that formed northeast of the HSZ at the later stage of the HSZ formation is known as the Lærdal-Gjende fault system. This fault system formed ~367 Ma, in the Devonian, based upon Rb/Sr dating (Schärer, 1980). However, the evidence for brittle structures cannot be found along the HSZ.

In terms of the development of the HSZ, the period after forming the Lærdal-Gjende Fault (LGF) system until Carboniferous time is unknown. Based on the thermal history models, both of the footwall (sample BG-144 and BG-38) (Fig. 5.4b and Fig. 5.5b) and hanging wall (BG-139) (Fig. 5.4a) of HSZ have initiated to exhume since the late Permian, approximately in the ranges of 250-180 Ma. The cooling rates are varied between  $1.5^0\text{-}3^0\text{C/Ma}$ . This cooling rate is slightly low and the cooling gradient is rather gentle. Therefore, it is predicted that the cooling took place in response to erosion. Even though plotting of elevation against the AFT ages does not show a linear correlation, it can be argued that all of the samples were collected in low altitudes less than 50 meter, hence the relationship is masked. Exhumation in this period caused reactivation of the HSZ and the LGF system. The evidence from paleomagnetic analysis exhibits reactivation of the LGF occurred in the range of 260-250 Ma (Andersen et al, 1999).

The erosion process during the Permo-Triassic might be completely removed all of burial on top of the footwall of HSZ and only a part of nappes on the hanging wall have been removed.

Based on the present AFT data, it is interpreted that the erosion process was still active during the Permo-Triassic (Fig. 5.9b). A part segment of nappes on top of the hanging wall was eroded but the nappes below are still preserved. The interesting feature is that the AFT ages increase inland both in the hanging and the footwall. The AFT patterns likely are related to the presence of brittle LGF structures. This brittle structure dies out between Aurland and the Hardangerfjord (Fossen and Hurich, 2005) and appears in the Lærdal area. It might be that the brittle structure in the southwest has been eroded before Permo-Triassic time meanwhile this structure is still preserved further inland. This hypothesis is still speculative and needs further investigation.

The cooling event in the footwall is not uniform, only some samples show Permian AFT ages and most of them exhibit Jurassic fission ages. Another scenario is that the footwall probably did not exhume within the Permo-Triassic, and that the minor Permo-Triassic AFT ages are only variations due to different chemical properties in the analyzed apatite grains.

The Permo-Triassic cooling event coincided when rifting propagated into the North Sea and mainly centered in the Horda Platform (Torsvik et al., 2002). The exact timing of this rifting event is poorly constrained, however Færseth et al. (1976) assumed that it occurred during the mid-Permian (ca. 260 Ma) when a swarm of basaltic dikes formed along the coastal area of the Sunnhorland, Sotra and Sunnfjord region. Fossen and Dunlap (1999) deduced that two pulses of magmatism occurred during the formation of the Permo-Triassic rifting based on K-Ar and  $^{40}\text{Ar}/^{39}\text{Ar}$  thermochronology of the alkaline dikes in Sunnhordland. The first event took place in early Permian times (260-250 Ma) and was followed by a second pulse represented by more extensive dike intrusions in the late Triassic (220 Ma).

The Permian cooling on both blocks of the HSZ was subsequently followed by Jurassic rapid cooling only in the footwall of the HSZ (Fig. 5.9c). It was documented in sample BG-62 (Fig. 5.5a) which describes cooling rate of  $6^{\circ}\text{C}/\text{Ma}$  at 190-180 Ma (the early Jurassic). Even though, the Jurassic cooling is only represented by one sample of the thermal history models, it is expected that other samples will show similar Jurassic or younger cooling due to low average AFT ages. The cooling rate of  $6^{\circ}\text{C}/\text{Ma}$  is quite rapid and shows a steep gradient. The rapid cooling is typical for tectonic denudation. In addition the samples exhibit a negative correlation of elevation vs. AFT ages in which the altitude is varied up to 450 m. It is implied that the erosion process was minor and tectonic denudation was predominant.



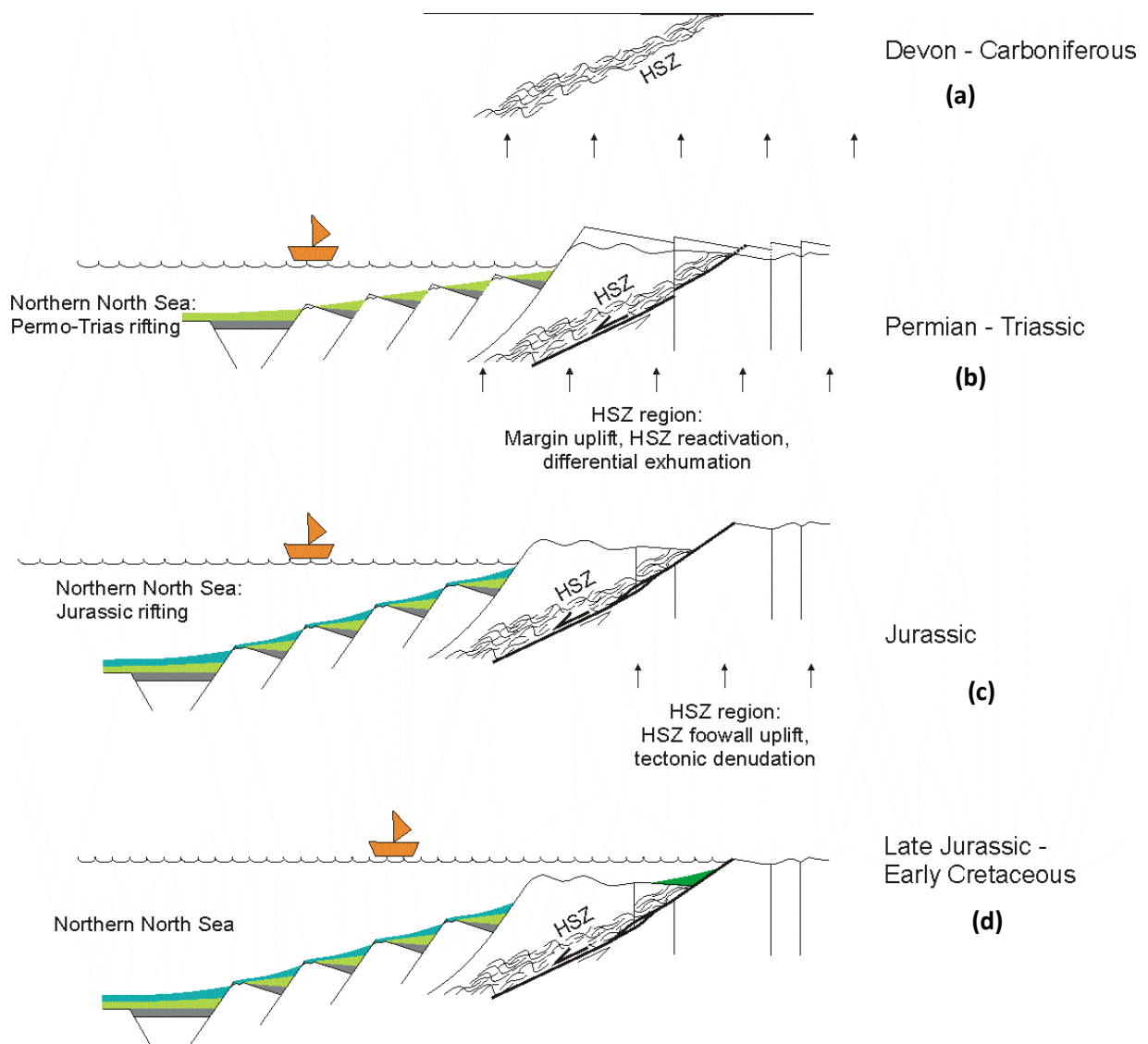


Fig. 5.9: Schematic illustration of the exhumation of the HSZ and adjacent area. See text for further explanation

This Jurassic rifting corresponds to the rifting activity which occurred in the entire Arctic-North Atlantic and affected mainly the formation of the Viking, Central and Moray Firth Grabens (Ziegler, 1991). In the Norwegian mainland, the youngest dikes in the Sunnhordland region yield a mean age of 164 Ma. This age corresponds to the volcanic activity in the North Sea (Færseth et al., 1976). This rifting event led to reactivation of the LGF system in the range of late Jurassic-Cretaceous times, based on paleomagnetic analysis (Andersen et al., 1999).

The later event was a burial event which took place at the Middle Jurassic-Middle Cretaceous, and coincided with the period of transgression and deposition of sediment clastics and carbonates at Middle-Late Cretaceous (Doré, 1992; Riis, 1996). This hypothesis was corroborated by Fossen et al. (1997) who suggested burial event during the late Jurassic.

Thermal history models of sample BG-62 and BG-38 also show burial events occurred during 180-100 Ma (Middle Jurassic-Early Cretaceous) (Fig. 5.9d).

In summary, cooling events in the HSZ and adjacent areas during the late Permian-Jurassic occurred in response to erosional events combined with tectonic rift flank uplift. This conclusion is similar to what was reported by Rohrman et al. (1995). The entire conclusion of this master thesis is summarized in the following chapter.

## 6. CONCLUSION

Analysis AFT ages and tectonics of the Hardangerfjord Shear Zone can be summarized as follow:

- Plotting the AFT ages against elevations does not show any correlation. This is caused by several factors: (a) because the differences of elevations are not significant, (b) cooling in the present study occurred rather by tectonic which is called tectonic denudation, (c) A vertical profile of samples cannot directly give a correlation of elevation-AFT ages if the areas have been rotated after cooling.
- Comparison the AFT ages against the annealing kinetic parameters (MTL and  $D_{par}$ ) also does not signify positive correlation. Several factors are considered: (a) a decrease in the AFT age is not accompanied by a decrease in the MTL. A 1:1 correlation of those parameters only occurs in isotropic medium. It can be implied that the analyzed apatite are anisotropic, (b) anisotropic feature of apatite is controlled by the structure and the chemistry, which reflects different annealing rates, (c) a multiple cooling histories result a more complex track length distributions.
- Samples were taken from the hanging wall of the HSZ have AFT ages range from  $146.2 \pm 9.3$  Ma –  $227.4 \pm 14.3$  Ma, with a weighted mean age of  $174 \pm 12$  Ma (Middle Jurassic). Meanwhile, from the footwall is obtained AFT ages range of  $180 \pm 8.4$  -  $105.6 \pm 7.9$  Ma, and the weighted mean is  $145 \pm 16$  Ma ( Late Jurassic – Early Cretaceous time).
- The thermal histories have been modeled from 5 samples; 3 samples from the footwall and 2 samples from the hanging wall. The first cooling event reactivated the two blocks of the HSZ at about 250-180 Ma. The Permian cooling rate is rather slow about  $1.5 \cdot 10^{-3} \text{ } ^\circ\text{C/Ma}$ . It is predicted that the cooling took place in response to erosion.
- The second cooling event initiated at early Jurassic time, and only reactivated the footwall of the HSZ. It was documented in sample BG-62 which describes cooling rate of  $6 \text{ } ^\circ\text{C/Ma}$  at 190-180 Ma and shows a steep gradient. The rapid cooling is typical for dominating tectonic denudation than the erosion process.
- At the Middle Jurassic-Middle Cretaceous, the areas experienced the burial event, as is shown in the thermal history models of sample BG-62 and BG-38. This event is coincided with a period of transgression and deposition of sediment clastics and

carbonates at Middle-Late Cretaceous (Doré, 1992; Riis, 1996) and supported by Fossen et al. (1997) who suggested burial event during the late Jurassic.

- In summary, cooling events in the HSZ and adjacent areas during the late Permian-Jurassic occurred due to erosional processes combined with tectonic rift flank uplift.
- The Permian and Jurassic rifting activities might be responsible to the reactivation of the faults in the rift flank notably along the HSZ and most likely affects the LGF.

## REFERENCES

- Andersen, T. B., Torsvik, T. H., Eide, E. A., Osmundsen, P. T., and Faleide, J. I., 1999:** Permian and Mesozoic extensional faulting within the Caledonides of Central South Norway. *J. Geol. Soc. London*, 156, pp. 1073–1080.
- Andersen, T.B., 1995:** Extensional tectonics in southern Norway: an overview. *Tectonophysics*, 273 (1998), pp. 129–153.
- Anderson, E. M., 1951:** The Dynamics of Faulting and Dyke Formation with Applications to Britain. *Oliver and Boyd, London (1951)*, pp. 206.
- Andriessen, P.A.M., and Boss A., 1986:** Post Caledonian thermal evolution and crustal uplift in the Eidfjord area, western Norway. *Norsk Geol. Tidsskr.*, 66 (1986), pp. 243–250.
- Barbarand, J., Carter, A., Wood, I., and Hurford, T., 2003:** Compositional and structural control of fission-track annealing in apatite. *Chemical Geology*, vol. 198, pp. 107- 137.
- Bhandari, N., Bhat, S.G., Lal, D., Rajagopalan, G., Tamhane, A. S., Venkatavaradan, V. S., 1971:** Fission fragment tracks in apatite: recordable track lengths. *Earth and planetary science letters*, volume 13 issue 1, pp. 191–199.
- Bjørnseth, H. M., Grant, S. M., Hansen, E. K., Hossack, J. R., Roberts, D. G., and Thompson, M., 1997:** Structural evolution of the Vøring Basin, Norway, during the Late Cretaceous and Palaeogene. *Journal of the Geological Society, London, Vol. 154, 1997*, pp. 559–563.
- Block, L., and Royden, L. H., 1990:** Core complex geometries and regional scale flow in the lower crust. *Tectonics*, vol. 9, pp. 557–567.
- Bockelie, J.F., and Nystuen, J. P., 1985:** The southeastern part of the Scandinavian Caledonides. In: Gee, D. G. and Sturt, B.A. (eds.) *The Caledonide Orogen Scandinavia and related areas*, pp. 69-88, Wiley, Chichester.
- Boundy, T. M., Essene, E. J., Hall, C. M., Austrheim, H., and Halliday, A. N., 1996:** Rapid exhumation of lower crust during continent-continent collision and late extension: Evidence from  $^{40}\text{Ar}/^{39}\text{Ar}$  incremental heating of hornblendes and muscovites, Caledonian orogen, western Norway. *Geol. Soc. Am. Bull.*, 108, pp. 1425– 1437.
- Brandon, M. T., 1992:** Decomposition of fission track grain age distributions. *Am. J. Sci.*, 292 (1992), pp. 535–564.
- Brekke, H., 2000:** The tectonic evolution of the Norwegian Sea continental margin with emphasis on the Vøring and Møre Basins, in Dynamics of the Norwegian Margin, edited by Nottvedt, A. *Geol. Soc. Spec. Publ.*, 167, pp. 327–378.

**Brekke, H., and Riis F., 1987:** Tectonics and basins evolution of the Norwegian shelf between 62°N and 72°N. *Nor. Geol. Tidsskr.*, 67 (1987), pp. 295–321.

**Buer, K.Y., 1990a:** The graben boundary faults of the Oslo Rift, displacement, mode of deformation and links. *Abstract 19th Nordic Winter Meeting, Geonytt*, 17 (1990), pp. 34.

**Burtner, R.L., Nigrini, A., and Donelick, R.A., 1994:** Thermochronology of lower Cretaceous source rocks in the Idaho-Wyoming thrust belt. *American Association of Petroleum Geologists Bulletin*, 78(10), pp. 1613-1636.

**Carlson, W. D., Donelick, R. A., Ketcham, and R. A., 1999:** Variability of apatite fission-track annealing kinetics: I. Experimental results. *Am. Mineral.*, 84 (1999), pp. 1213–1223.

**Cawood, P. A., Mc Causland P. J. A., Dunning, G. R., 2001: Opening Iapetus: Constraints from the Laurentian margin in Newfoundland.** *Geological Society of America Bulletin*, April, 2001, v. 113, no. 4, pp. 443-453.

**Chauvet, A., and Séranne, M., 1994:** Extension-parallel folding in the Scandinavian Caledonides: implications for late-orogenic processes. *Tectonophysics*, 238 (1994), pp. 31–54.

**Kooi, H., and Cloetingh S., 1992:** Lithospheric necking and regional isostasy at extensional basins: Stress-induced vertical motion and relative sea level changes. *J. Geophys. Res.*, 97(B12), 17, pp. 573–591.

**Davis, G. H., and Reynolds, S. J. 1996:** Structural geology of rocks and regions. *John Wiley and Sons, second edition 1996 pp. 204-268.*

**Deer, W.A., 1969:** Field excursion guide of the Tertiary Volcanic rocks of Ardnamurchan ‘Symposium on volcanoes and their root, Oxford. *International Association of Volcanology and Chemistry of the Earth’s Interior*, 1969.

**Dobrzhinetskaya, L. F., Eide E., Larsen, R. B., Sturt, B. A., Trønnes, R. G., Smith, D. C., Taylor, W. R., and Posukhova, T. V., 1995:** Microdiamond in high-grade metamorphic rocks of the Western Gneiss region, Norway. *Geology*, July, 1995, v. 23, pp. 597-600.

**Donelick, R. A., O’Sullivan, P. B., and Ketcham, R. A., 2005:** Apatite Fission-Track Analysis. Reviews in *Mineralogy and Geochemistry* 2005 v. 58 no. 1 pp. 49-94.

**Donelick, R. A., 1991:** Crystallographic orientation dependence of mean etchable fission track length in apatite: An empirical model and experimental observations. *American Mineralogist*, 76, pp. 83–91.

**Donelick, R.A., 1993:** A method of fission track analysis utilizing bulk chemical etching of apatite. *U.S. Patent 5*, pp. 267-274.

**Donelick, R.A., 1995:** A method of fission track analysis utilizing bulk chemical etching of apatite. *Australia Patent*, pp. 658-800.

**Doré, A. G., Lundin, E. R., Birkeland, Ø., Eliassen, P. E., and Jensen, L. N., 1999:** Principal tectonic events in the evolution of the northwest European Atlantic margin.

Petroleum Geology of Northwest Europe: Proceedings of the 5th Conference Held at the Barbican Centre, London, 26– 29 October 1997, edited by Fleet A. J., and Boldy, S. A. R., *Geol. Soc., London*, pp. 41–61.

**Doré, A. G., 1991:** The structural foundation and evolution of Mesozoic seaways between Europe and the Arctic. *Palaeogeographic Palaeoclimatology Palaeoecology*, vol. 87, pp. 44–492.

**Doré, A. G., 1992:** The base Tertiary surface of southern Norway and the northern North Sea. *Nor. Geol. Tidsskr.*, 72, pp. 259–265, 1992a.

**Doré, A. G., 1992b:** Synoptic paleogeography of the Northeast Atlantic Seaway: Late Permian to Cretaceous, in Basins on the Atlantic Seaboard: Petroleum Geology, Sedimentology and Basin Evolution, edited by J. Parnell. *Geol. Soc. Spec. Publ.*, 62, pp. 421–446, 1992b.

**Duddy I. R., Green, P. F., Hegarty, K. A., Bray R. J., and O'Brien G. W., 1998:** Dating and duration of hot fluid flow events determined using AFTA® and vitrinite reflectance-based thermal history reconstruction. *Geological Society, London, Special Publications January 1, 1998*, v. 144, pp. 41–51.

**Dunlap, W. J., and Fossen, H., 1998:** Early Paleozoic orogenic collapse, tectonics stability, and late Paleozoic continental rifting revealed through thermochronology of K-feldspars, southern Norway. *Tectonics*, v. 17, 1998, pp. 604– 620.

**Ehlers, T. A., Chaudhri, T., Kumar, S., Fuller, C.W., Willett, S.D., Ketcham, R. A., Brandon, M. T., Belton, D. X., Kohn, B. P., Gleadow, A. J.W., Dunai, T. J., Fu, F. Q., 2005:** Computational Tools for Low-Temperature Thermochronometer Interpretation. *Reviews in Mineralogy and Geochemistry 2005* v. 58 no. 1 pp. 589–622.

**Eide, E. A., Torsvik, T. H., Andersen, T. B., and Arnaud, N. O., 1999:** Early Carboniferous unroofing in Western Norway: A tale of alkali feldspar thermochronology. *J. Geol.*, 107, pp. 353–374.

**Eldholm, O., Thiede, J., and Taylor, E., 1989:** Evolution of the Vøring volcanic margin, Proc. Ocean Drill. *Program Science Results*, vol. 104, pp. 1033–1065.

**Eldholm, O., Tsikalas, F., and Faleide, J. I., 2002:** Continental margin off Norway 62–75°N: Palaeogene tectono-magmatic segmentation and sedimentation. *Geological Society, London, Special Publications January 1, 2002*, v. 197, pp. 39–68

**Faleide, J. I., Vågnes, E., Gudlaugsson, S. T., 1993:** Late Mesozoic-Cenozoic evolution of the south-western Barents Sea in a regional rift-shear tectonic setting. *Marine and Petroleum Geology*, vol. 10, issue 3, June 1993, pp. 186–214.

**Fitzgerald, P. G., Sorkhabi, R. B., Redfield, T. F., and Stump, E., 1995:** Uplift and denudation of the central Alaska Range: A case study in the use of apatite fission track thermochronology to determine absolute uplift parameters. *Journal of Geophysical Research*, vol. 100, no. B10, 1995, pp. 175–191.

**Fleischer, R.L., and Hart, H.R., 1972:** Fission track dating: techniques and problems. Bishop, W.W., Miller, D.A., Cole, S. (Eds.), Calibration of Hominoid Evolution. *Scottish Academic Press, Edinburgh (1972), pp. 135–170.*

**Fleischer, R. L., Price, P. B., Symes E. M., and Miller D. S., 1964b:** Fission-Track Ages and Track-Annealing Behavior of Some Micas. *Science, vol. 143, no. 3604, pp. 349-35.*

**Fleischer, R. L., Price, P. B., Walker, R. M., 1965a:** Ion Explosion Spike Mechanism for Formation of Charged-Particle Tracks in Solids. *Journal of Applied Physics Issue Date: Nov 1965 Volume: 36 Issue: 11 pp. 3645 – 3652.*

**Fleischer, R. L. Price, P. B. Walker, R. M., 1965b:** Effects of Temperature, Pressure, and Ionization of the Formation and Stability of Fission Tracks in Minerals and Glasses. *Journal of Geophysical Research, Vol. 70, No. 6, pp. 1497-1502.*

**Fleischer, R. L., Price, P. B., Walker, R. M., 1975:** Nuclear Tracks in Solids: Principles and Applications. *University of California Press, London, England, 1975, pp. 3-209.*

**Fossen, H. and Dunlap W.J., 1999:** On the age and tectonic significance of Permo-Triassic dikes in the Bergen-Sunnhordland region, southwestern Norway. *Norsk Geologisk Tidsskrift, Vol. 79, Issue 3, 1999, pp. 169-178.*

**Fossen, H. and Hurich, C. A., 2005:** The Hardangerfjord Shear Zone in SW Norway and the North Sea: a large-scale low-angle shear zone in the Caledonian crust. *Journal of the Geological Society, vol. 162, issue 4, pp. 675-687.*

**Fossen, H., 1992:** The role of extensional tectonics in the Caledonides of south Norway. *Journal Of Strucural Geology, vol.14, pp. 1033-1046.*

**Fossen, H., and Tikoff, B., 1993:** The deformation matrix for simultaneous simple shearing, pure shearing and volume change, and its application to transpression-transension tectonics. *Journal of structural Geology, Vol. 15, Issue 3-5, March–May 1993, pp. 413-422.*

**Fossen, H., and Holst, T. B., 1995:** Northwest-verging folds and the northwestward movement of the Caledonian Jotun Nappe, Norway. *Journal of Structural Geology, Vol. 17, issue 1, January 1995, pp. 3–15*

**Fossen, H., Mangerud, G., Hesthammer, J., Bugge, T., & Gabrielsen, R. H., 1997:** The Bjørøy Formation: a newly discovered occurrence of Jurassic sediments in the Bergen Arc System. *Norsk Geologisk Tidsskrift 77, pp. 269-287.*

**Fossen, H., 1998:** Advances in understanding the post Caledonian structural evolution of the Bergen area, West Norway. *Norsk Geologisk Tidsskrift 78, pp. 33-46.*

**Fossen, H., 2000:** Extensional tectonics in the Caledonides: Synorogenic or postorogenic. *Tectonics, 19, pp. 213–224.*

**Furnes, H., Thon, A., Nordås, J., Garmann, and L. B., 1982a:** Geochemistry of Caledonian metabasalts from some Norwegian ophiolite fragments. *Contribution to Mineralogy and Petrology, Vol 79, Number 3, pp. 295-307.*



- Færseth, R. B., 1996:** Interaction of Permo-Triassic and Jurassic extensional fault blocks during the development of the northern North Sea. *J. Geol. Soc. London*, 153, pp. 931– 944.
- Færseth, R. B., Gabrielsen, R. H., and Hurich, C. A., 1995:** Influence of basement in structuring of the North Sea basin, offshore southwest Norway. *Nor. Geol. Tidsskr.*, 75, pp. 105– 119.
- Færseth, R. B., Macintyre, R.M., Naterstad, and J., 1976:** Mesozoic alkaline dykes in the Sunnhordland region, western Norway: ages, geochemistry and regional significance. *Lithos*, Vol. 9, Issue 4, pp. 331-345.
- Gallagher, K., Brown, R., Johnson, and C., 1998:** Fission track analysis and its applications to geological problems. *Annual Review Earth Planetary Science*, 26 (1998), pp. 519–572.
- Galbraith, R. F., 1981:** On statistical models for fission track counts. *Mathematical Geology*, vol. 13, no. 6, pp. 471-478.
- Galbraith, R. F., 1988:** A note on graphical presentation of estimated odds ratios from several clinical trials. *Statistics in Medicine*, vol. 7 issue 8, pp. 889-894.
- Galbraith, R. F., and Laslett, G. M., 1985:** Some remarks on statistical estimation in fission track dating. *Nuclear Tracks*, 10, pp. 361 - 363.
- Galbraith, R. F., and Laslett, G. M., 1993:** Statistical models for mixed fission track ages. *Nuclear Tracks and Radiation Measurements*, vol. 21, issue 4, pp. 459–470.
- Gallagher, K., Brown, R., Johnson, and C., 1998:** Fission track analysis and its applications to geological problems. *Annual Rev. Earth Planet. Sci.*, 26 (1998), pp. 519–572
- Galliker, D., Hugentobler, E., and Hahn, B., 1970:** Spontane Kernspaltung von U-238 und Am-241. *Helv. Phys. Acta*, 43 (1970), pp. 593–606
- Gee, D. G., Guezou, J. C., Roberts, D., and Wolff, F. C., 1985:** The central-southern part of the Scandinavian Caledonides, in *The Caledonide Orogen-Scandinavia and Related Areas*, edited by Gee, D. G., and Sturt, B. A., pp. 109–133, John Wiley, Hoboken, N. J.
- Gee, D. G., Fossen, H., Henriksen, N., and Higgins, A. K., 2008:** From the Early Paleozoic Platforms of Baltica and Laurentia to the Caledonide Orogen of Scandinavia and Greenland. *Episodes*, vol. 31, no. 1.
- Gegugin, Y. E., Voreb'eva, and I. V., Berzina, I. G., 1968:** Thermal stability of uranium fission fragment tracks in muscovite single crystal (effect of anisotropy). *Soviet Physics-Solid State*, 10 (1968), pp. 1431–1433.
- Gleadow, A. J. W., and Duddy, I. R., 1981:** A natural long-term track annealing experiment for apatite. *Nuclear Tracks*, 5 (1981), pp. 169–174.
- Gleadow, A. J.W., and Lovering, J. F., 1977:** Geometry factor for external detectors in fission track dating. *Nuclear Track Detection*, Vol. 1, Issue 2, pp. 99–106.

**Gleadow, A. J. W., and Lovering, J. F., 1978b:** Thermal history of granitic rocks from western Victoria: A fission-track dating study. *Journal of the Geological Society of Australia* Volume 25, Issue 5-6, pp. 323-34.

**Gleadow, A. J. W., Duddy, I. R., Green P. F. and Lovering, J. F. 1986:** Confined fission track lengths in apatite: a diagnostic tool for thermal history analysis. *Contributions to Mineralogy and Petrology* Volume 94, Number 4, pp. 405-415.

**Gleadow, A.J.W., Duddy, I. R., Green, P. F., Lovering, J. F., 1985:** Confined fission track lengths in apatite 1985: a diagnostic tool for thermal history analysis. *Earth Planet Sci. Lett.* (1985) (to be submitted)

**Gleadow, A. J. W., and Duddy I. R., 1981:** A natural long-term track annealing experiment for apatite. *Nuclear Tracks*, 5 (1981), pp. 169–174.

**Green, P.F. and Durrani, S.A., 1977:** Annealing studies of tracks in crystals. *Nuclear Track Detection* Volume 1, Issue 1, 1977, pp. 33–39.

**Green, P. F., Duddy, I. R., Gleadow, A. J. W., Tingate, P. R., and Laslett, G. M., 1985:** Fission-track annealing in apatite: track length measurements and the form of the Arrhenius plot. *Nuclear Tracks*, 10 (1985), pp. 323–328.

**Green, P.F., Duddy, I. R., Gleadow, A. J. W., Tingate, P. R., and Laslett, G. M., 1986:** Thermal annealing of fission tracks in apatite: 1. a qualitative description. *Chem. Geol., Isot. Geoscience Sect.*, 59 (1986), pp. 237–253.

**Green, P. F., 1988:** The relationship between track shortening and fission track age reduction in apatite: combined influences of inherent instability, annealing anisotropy, length bias and system calibration. *Earth and Planetary Science Letters* Vol. 89, issues 3-4, August 1988, pp. 335-352.

**Griffin W. L., and Brueckner, H. K. 1980:** Caledonian Sm–Nd ages and a crustal origin for Norwegian eclogites. *Nature* 285, pp. 319 – 321.

**Griffin, W. L., and Brueckner, H. K., 1985:** REE, Rb-Sr and Sm-Nd studies of Norwegian eclogites. *Chemical Geology: Isotope Geoscience Section* Vol. 52, Issue 2, pp. 249–271.

**Griffin, W. L., Austrheim, H., Brastad, K., Bryhni, I., Krill, A., Mørk, M. B. E., Qvale, H., Tørud, B., 1985:** High-pressure metamorphism in the Scandinavian Caledonides, Gee, D.G. Sturt B.A. (Eds.), *The Caledonide Orogen - Scandinavia and Related Areas*, Wiley, Chichester (1985) (in press).

**Hansen, K., Pedersen, S., Fought, H., and Stockmarr, P., 1996:** Post-Sveconorwegian exhumation and cooling history of Evje area, southern Setesdal, Central South Norway. *Norsk Geol. Unders. Bull.*, 431, 49-58.

**Hartz, E. H., and Torsvik, T. H., 2002:** Baltica upside down: A new plate tectonic model for Rodinia and the Iapetus Ocean. *Geology*, March, 2002, vol. 30, pp. 255-258.

**Hendriks, B.W. H., Redfield, T. F., Andriessen, P. A. M., Cederbom, C., Huigen, Y., and Murrell, G., 2004:** The denudation of Fennoscandia: an apatite fission track map. *Abstracts, 26th Nordic Geological Winter Meeting, Geologiska Foreningen, Stockholm, vol. 126, pp. 81.*

**Hendriks, B.W. H., Andriessen, P., Huigen, Y., Leighton, C., Redfield, T., Murrell, G., Gallagher, K., and Nielsen, S. B., 2007:** A fission track data compilation for Fennoscandia. *Norwegian Journal of Geology, v. 87, p. 143–155.*

**Hitchen, K. and Ritchie, J. D., 1993:** New K-Ar ages, and a provisional chronology, for the offshore part of the British Tertiary Igneous Province. *Scottish Journal of Geology, 29, pp. 73-85.*

**Hurford, A. J., and Carter, A., 1991:** The role of fission track dating in discrimination of provenance. *Geological Society, London, Special Publications January 1, 1991, vol. 57, pp. 67-78.*

**Hurford, A. J., 1990a:** International Union of Geological Sciences Subcommittee on Geochronology recommendation for the standardization of fission track dating calibration and data reporting. *Nucl Tracks 17 pp. 233–36.*

**Hurford, A. J., 1990b:** Standardization of fission track dating calibration: recommendation by the Fission Track Working Group of the I.U.G.S. Subcommittee on Geochronology. *Chem. Geol. 80, pp. 171–78.*

**Hurford, A. J., and Green, P. F., 1982:** A users' guide to fission track dating calibration. *Earth and Planetary Science Letters Volume 59, Issue 2, July 1982, pp. 343–354.*

**Hurford, A. J., and Green, P. F., 1983:** The zeta age calibration of fission-track dating. *Chemical Geology Volume 41, 1983, pp. 285–317.*

**Hurford, A. J., and Green, P. F., 1981b:** Standards, dosimetry and the uranium-238  $\lambda_f$  decay constant: a discussion. *Nuclear Tracks, 5 (1981), pp. 73–75.*

**Hurford, A. J., and Hammerschmidt, K., 1985:**  $^{40}\text{Ar}/^{39}\text{Ar}$  and K/Ar dating of the bishop and fish canyon tuffs: Calibration ages for fission-track dating standards. *Chemical Geology: Isotope Geoscience section Vol. 58, Issues 1–2, 20 December 1985, pp. 23–32.*

**Hurford, A. J., Fitch, F. J., and Clarke, A., 1984:** Resolution of the age structure of the detrital zircon populations of two lower Cretaceous sandstones from the Weald of England by fission track dating. *Geological Magazine, vol. 121, pp. 269-277.*

**Hurich, C.A., and Kristoffersen, Y., 1988:** Deep structure of the Caledonide orogen in southern Norway: new evidence from seismic reflection profiling. *Norges Geologiske Undersøkelse Special Publication 3, pp. 96–101.*

**Johansen, L., 2008:** Exhumation history across major lineaments within and around the Bergen Arc using fission track thermochronology. *Master of Geodynamics Thesis, Department of Earth Science, University of Bergen, 75 pp.*

- Johnson, C., Harbury, N., and Hurford, A. J., 1997:** The role of extension in the Miocene denudation of the Nevado-Filábride Complex, Betic Cordillera (SE Spain). *Tectonics*, vol. 16, pp. 189-204.
- Karpuz, M. R., Karl, A., Royh, G., and Roberth, B., 1990:** Utilizing multi-sensor and geo-data for analysis of neotectonics in Sunnhordland, West Norway. *Thematic Conference on Remote Sensing for Exploration Geology: Methods, Integration, Solutions, 7th, Calgary, Canada; 2-6 Oct. 1989.* pp. 713-733.
- Karpuz, M. R., Gabrielsen, R. H., Engell-Sørensen, L., and Anundsen, K., 1991:** Seismotectonic significance of the January 29, 1989 Etne earthquake, southwest Norway. *Terra Nova* vol. 3, pp. 540-549.
- Ketcham, R. A., Donelick, R. A., and Carlson, W. D., 1999:** Variability of apatite fission-track annealing kinetics; III, Extrapolation to geological time scales. *American Mineralogist* September 1999 v. 84 no. 9 pp. 1235-1255.
- Ketcham, R. A., 2005:** Forward and Inverse Modeling of Low-Temperature Thermochronometry Data. *Reviews in Mineralogy and Geochemistry* 2005 vol. 58 no. 1 pp. 275-314.
- Ketcham, R. A., 2005a:** The role of crystallographic angle in characterizing and modeling apatite fission-track length data. *Radiation Measurements* Vol. 39, Issue 6, pp. 595–601.
- Koch, G. S., Jr., and Link, R. F., 1970:** Statistical analysis of geological data. *Vol. 1: John Wiley and Sons, New York, 375 p.*
- Kowallis, B. J., Heaton, J. S., and Bringhurst, K., 1986:** Fission-track dating of volcanically derived sedimentary rocks. *Geology* January, 1986 vol. 14, no. 1, pp. 19-22.
- Krabbendam, M., and Dewey, J. F., 1998:** Exhumation of UHP rocks by transtension in the Western Gneiss Region, Scandinavian Caledonides. *Geological Society, London, Special Publications* January 1, 1998, vol. 135, pp. 159-181.
- Kullerud, L., Torudbakken, B., Iiebekk, S., 1986:** A compilation of radiometric age determinations from the western gneiss region, south Norway. *Norsk Geol. Unders.*, 406, pp. 17- 42.
- Kuvaas, S., and Kodaira, 1997:** The formation of the Jan Mayen microcontinent: The missing piece in the continental puzzle between the Møre–Vøring Basins and East Greenland. *First Break*, 15 (1997), pp. 239–247.
- Laslett, G. M., Green, P. F., Duddy, I. R., and Gleadow, A. J. W., 1987:** Thermal annealing of fission tracks in apatite: A quantitative analysis. *Chem. Geol., Isot. Geoscience Sect.*, 65 (1987), pp. 1–13.
- Laslett, G.M., Gleadow, A. J. W., and Duddy, I. R., 1984:** The relationship between fission track length and track density in apatite. *Nuclear Tracks and Radiation Measurements* (1982) vol. 9, Issue 1, 1984, pp. 29–38.

- Li, Z. X., Bogdanova, S. V., Collins, A. S., Davidson, A., Waele, B. D., Ernst, R. E., Fitzsimons, I. C. W., Fuck, R. A., Gladkochub, D. P., Jacobs, J., Karlstrom, K. E., Lu, S., Natapov, L. M., Pease, V., Pisarevsky, S. A., Thrane, K., Vernikovsky, V. 2008:** Assembly, configuration, and break-up history of Rodinia: A synthesis. *Precambrian Research Volume 160, Issues 1–2, 5 January 2008*, pp. 179–210.
- Lundin, E. R., and Doré A. G., 1997:** A tectonic model for the Norwegian passive margin with implications for the NE Atlantic: Early Cretaceous to breakup. *J. Geol. Soc. London*, 154, pp. 545–550.
- Løvlie, R., and Mitchell, J. G., 1982:** Complete remagnetization of some Permian dykes from western Norway induced during burial/uplift. *Physics of the Earth and Planetary Interiors, Volume 30, Issue 4*, pp. 415-421.
- Magerholm, T., 2010:** Exhumation history and fault tectonics across the Hardangerfjor Shear Zone, using fission track thermochronology. *Master of Geodynamics Thesis, Department of Earth Science, University of Bergen*, 83 pp.
- Mancktelow, N. S., and Grasemann, B., 1997:** Time-dependent effects of heat advection and topography on cooling histories during erosion. *Tectonophysics*, vol. 15, pp. 167–195.
- Maurette, M., Pellas, P., and Walker, R. M., 1964:** Etude des traces de fission fossiles dans le mica. *Bull. Soc. Franc. Miner.*, vol. 87 (1964), pp. 6–17.
- McDowell, F. W., and Keizer, R. P., 1977:** Timing of mid-Tertiary volcanism in the Sierra Madre Occidental between Durango City and Mazatlan, Mexico. *GSA Bulletin October, 1977 v. 88 no. 10* pp. 1479-1487.
- McKerrow, W. S., Mc Niocaill, C., and Dewey, J. F., 2000:** The Caledonian Orogeny redefined. *Journal of the Geological Society, November 2000*, vol. 157, no. 6, pp. 1149-1154.
- Wagner, G. A., Miller, D. S., Jäger, and E., 1979:** Fission track ages on apatite of Bergell rocks from Central Alps and Bergell boulders in Oligocene sediments. *Earth and Planetary Science Letters Vol. 45, Issue 2, November 1979*, pp. 355–360.
- Mosar, J., 2003:** Scandinavia's North Atlantic passive margin. *Journal of Geophysical Research, Vol. 108, No. B8*, pp. 2360.
- Müller, R. D., and Roest, W. R., 1992:** Fracture zones in the North Atlantic from combined Geosat and Seasat data. *Journal of Geophysical Res.*, vol. 97, pp. 3337-3350.
- Mørk, M. B. E., Kullerud, K., and Stabel, A., 1988:** Sm-Nd dating of Seve eclogites, Norrbotten, Sweden — Evidence for early Caledonian (505 Ma) subduction. *Contributions to Mineralogy and Petrology Volume 99, No. 3*, pp. 344-351.
- Ragnhildstveit, J., and Heliksen, D., 1997:** Geologisk kart over Norge: Berggrunnskart Bergen-M 1: 250.000. *Norges Geologiske Undersøkelse. geological map*.
- Ragnhildstveit, J., Naterstad, J., Jorde, K., and Egeland, B., 1998:** Geologisk kart over Norge, Berggrunnskart Haugesund-M 1: 250.000. *Norges Geologiske Undersøkelse. Geological Map*.

- Osmundsen, P. T., and Andersen, T. B., 2001:** The middle Devonian basins of western Norway: Sedimentary response to large-scale transtensional tectonics? *Tectonophysics*, vol. 332, pp. 51–68.
- Pedersen, R. B., Nordgulen, Ø., Brnes, C. G., Prestvik, T., and Barnes, M. A., 1999:** U-Pb dates from dioritic and granitic rocks in Velfjord, north-central Norway. *Norsk Geologisk Forenings 16. Landsmøte 1999, program and abstracts, Geonytt*, 81.
- Price, P. B., and Walker, R. M., 1962b:** Chemical etching of charged particle tracks in solids. *J. Appl. Phys.*, 33 (1962), pp. 3407–3411.
- Ramberg, I. B., and Larsen B.T., 1978:** Tectonomagmatic evolution Dons, J. A., Larsen, B. T., (Eds.), *The Oslo Paleorift. A Review and Guide to Excursions, Nor. Geol. Unders.*, 337 (1978), pp. 55–73
- Ramberg, I. B., Gabrielsen, R. H., Larsen, B. T., Solli, A. 1977:** Analysis of fracture pattern in southern Norway. *Geol. Mijnbouw*, 56 (1977), pp. 295–310.
- Redfield, T. F., Osmundsen, P. T., & Hendriks, B. W. H., 2005:** The role of fault reactivation and growth in the uplift of western Fennoscandia. *Journal of the Geological Society*, December 2005, vol. 162 no. 6 pp. 1013-1030.
- Ren, S., Faleide, J. I., Eldholm, O., Skogseid, J., Gradstein, F., 2003:** Late Cretaceous–Paleocene tectonic development of the NW Vøring Basin. *Marine and Petroleum Geology* Vol.20, Issue 2, February 2003, pp. 177–206.
- Riis, F., 1996:** Quantification of Cenozoic vertical movements of Scandinavia by correlation of morphological surfaces with offshore data. *Global Planet Change*, 12, pp. 331–357.
- Roberts, D., 2003:** The Scandinavian Caledonides: event chronology, palaeogeographic settings and likely modern analogues. *Tectonophysics*, vol. 365, Issues 1–4, 24 April 2003, pp. 283–299.
- Rohrman, M., van der Beek, P., and Andriessen, P., 1994:** Syn-rift thermal structure and post-rift evolution of the Oslo Rift (southeast Norway): New constraints from fission track thermochronology. *Earth Planet Sci. Lett.*, 127, pp. 39–54.
- Rohrman, M., van der Beek, P., Andriessen, P., and Cloetingh, S., 1995:** Meso-Cenozoic morphotectonic evolution of southern Norway: Neogene domal uplift inferred from apatite fission track thermochronology. *Tectonics*, vol.14, pp. 704–718.
- Rohrman, M., and van der Beek, P., 1996:** Cenozoic postrift domal uplift of North Atlantic margins: An asthenospheric diapirism model. *Geological Society of America*, vol. 24 no. 10 pp. 901-904.
- Rokoengen, K., and Sørensen, S., 1990:** Late Jurassic sedimentary bedrock north of Utsira, offshore western Norway. *Norsk Geologisk Tidaakrift*, 1990, vol. 70, pp. 61-63.
- Russell, M. J., and Smythe, D. K., 1983:** Origin of the Oslo Graben in relation to the Hercynian-Alleghenian orogeny and lithospheric rifting in the North Atlantic. *Tectonophysics* Volume 94, Issues 1–4, 1 May 1983, pp. 457–472.

**Schärer, U., 1980:** U-Pb and Rb-Sr dating of a polymetamorphic nappe terrain: The Caledonian Jotun nappe, southern Norway. *Earth and Planetary Science Letters Volume 49, Issue 2, September 1980, pp. 205–218.*

**Séranne, C. A., and Faure, J. L., 1991:** Cinématique de l'extension tardiorogénique (Dévonien) dans les Calédonides Scandinaves et Britanniques, Comptes rendus de l'Académie des Sciences de Paris, in press.

**Solheim, A., Andersen, E. S., Elverhi, A., and Fiedler, A., 1996:** Late Cenozoic depositional history of the western Svalbard continental shelf, controlled by subsidence and climate. *Global and Planetary Change 12, pp. 135-148.*

**Steel, R. J., 1993:** Triassic–Jurassic megasequence stratigraphy in the Northern North Sea: rift to post-rift evolution. *Geological Society London, vol.4, pp. 299-315.*

**Steiger, R.H. and Jäger E., 1977:** Subcommittee on Geochronology: Convention on the use of decay constants in geo- and cosmochronology. *Earth Planet Sci. Lett., 36 (1977), pp. 359–362.*

**Sturt, B. A., and Roberts, D., 1991:** Tectonostratigraphic relationships and obduction histories of Scandinavian ophiolitic terranes. In: PETERSE TAL. (eds.) *Ophiolite Genesis and Evolution, Kluwer Academic Publishers, Amsterdam, pp. 745-769.*

**Sundvoll, B., Neumann, E. R., Larsen, B. T., and Tuen, E., 1990:** Age relations among Oslo Rift magmatic rocks: implications for tectonic and magmatic modelling. *Tectonophysics Volume 178, Issue 1, 1 June 1990, pp. 67–87.*

**Tagami, T., and O'Sullivan, P. B., 2005:** Fundamentals of Fission-Track Thermochronology. *Reviews in Mineralogy and Geochemistry 2005 vol. 58 no. 1 pp. 19-47.*

**Terry, M. P., Robinson, P., and Ravn, E. J. K., 2000:** Kyanite eclogite thermobarometry and evidence for thrusting of UHP over HP metamorphic rocks, Nordøyane, Western Gneiss Region, Norway. *American Mineralogist vol. 85, no. 11-12, pp. 1637-1650.*

**Togliatti, V., 1965:** Distribuzioni dei ranges e distribuzioni angolari delle tracce de fissioni fossili di  $U^{238}$  e delle fissioni indotte di  $U^{235}$  in mica. *Boll. Geofis. Teor. Appl., 7 (1965), pp. 326–335.*

**Torsvik, T. H., and Cocks, L. R. M., 2005:** Norway in space and time: A Centennial cavalcade. *Norwegian Journal of Geology, Vol. 85, pp. 73-86.*

**Torsvik, T. H., Sturt, B. A., Swensson, E., Andersen, T. B., and Dewey, J. F., 1992:** Palaeomagnetic dating of fault rocks: Evidence for Permian and Mesozoic movements and brittle deformation along the extensional Dalsfjord Fault, western Norway. *Geophys. J. Int., 109, pp. 565– 580.*

**Torsvik, T. H., Andersen, T. B., Eide, E. A., and Walderhaug, H. J., 1997:** The age and tectonic significance of dolerite dykes in western Norway. *J. Geol. Soc. London, vol. 154, pp. 961– 973.*

- Torsvik, T. H., Carlos, D., Mosar, J., Cocks, L. R. M., and Malme, T., 2002:** Global reconstructions and North Atlantic palaeogeography 440 Ma to Recent. BATLAS-Mid Norway Plate Reconstruction Atlas With Global and North Atlantic Perspectives, *edited by E. Eide*, pp. 18–39, *Geol. Surv. Of Norway, Trondheim, 2002*.
- Torsvik, T. H., Smethurst, M. A., Meert, J. G., Van der Voo, R., McKerrow, W. S., Brasier, M.D., Sturt, B.A., and Walderhaug, H. J., 1996:** Continental break-up and collision in the Neoproterozoic and Palaeozoic: A tale of Baltica and Laurentia. *Earth Science Reviews* 40, pp. 229–258.
- Tørresen, S., 2009:** Exhumation history and fault tectonics across the North Sea margin in the Nordhordland area, Øygarden to Masfjorden, using fission track thermochronology. *Master of Geodynamics Thesis, Departement of Earth Science, University of Bergen, 123 pp*.
- Valle, V., Færseth, R. B., Fossen, H., 2002:** Devonian-Triassic brittle deformation based on dyke geometry and fault kinematics in the Sunnhordland region, SW Norway. *Norwegian J. Geol.*, vol. 82, pp. 3-17.
- Wagner, G. A., and Reimer, G. M., 1972:** Fission track tectonics: The tectonic interpretation of fission track apatite ages. *Earth and Planetary Science Letters* Vol.14, Issue 2, March 1972, pp. 263–268.
- Wagner, G. A., 1972:** Geological interpretation of fission track ages. *Trans. Amer. Nucl. Soc.* 15, No. 1, pp. 117.
- Wagner, G. A., and Van den haute, P., 1992:** Fission Track Dating. *Kluwer Academic Publishing, Dordrecht (1992), 285 pp*.
- Wagner, G. A., Reimer, G. M., and Jäger, E., 1977:** Cooling ages derived by apatite fission track, mica Rb/Sr and K/Ar dating: the uplift and cooling history of the Central Alps. *Inst. Geol. Mineral., Univ. Padova, Mem.*, 30.
- White, N., and Lovell, B., 1997:** Measuring the pulse of a plume with the sedimentary record. *Nature*, Vol. 387, pp. 888-891.
- Yim, W. W. S., Gleadow, A. J. W., van Moort, J. C., 1985:** Fission track dating of alluvial zircons and heavy mineral provenance in Northeast Tasmania. *Journal of the Geological Society, London*, 142, pp. 351-356.
- Ziegler, P. A., 1990:** Geological Atlas of Western and Central Europe (2<sup>nd</sup> Eds.). *Shell Int. Petrol. Mij. B.V., dist. by Geol. Soc. Publ. House Bath.* 239 pp.
- Ziegler, P. A., 1991:** Geological Atlas of Western and Central Europe. *Shell/Elsevier, Gravenhage, The Netherlands (1991)*.
- Ziegler, P. A., 1992:** Geodynamics of Rifting. *Reprints from Tectonophysics, Amsterdam, London, NewYork, Tokyo: Elsevier.* pp. 901.



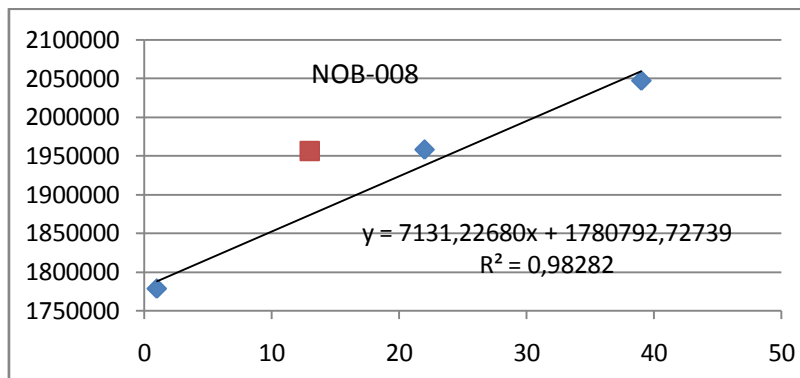
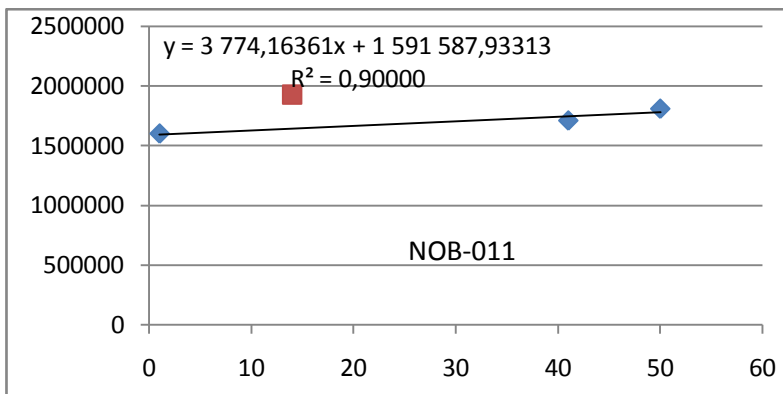
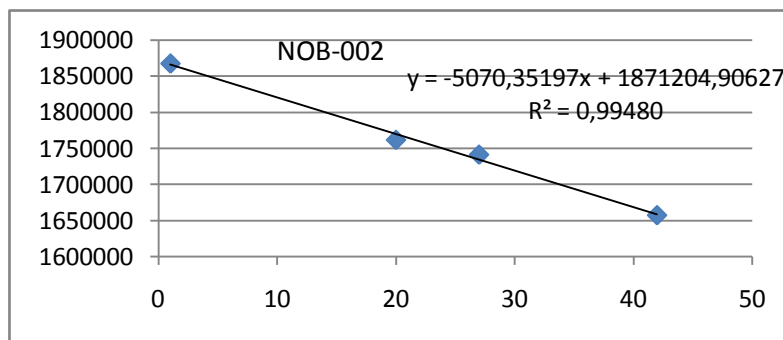
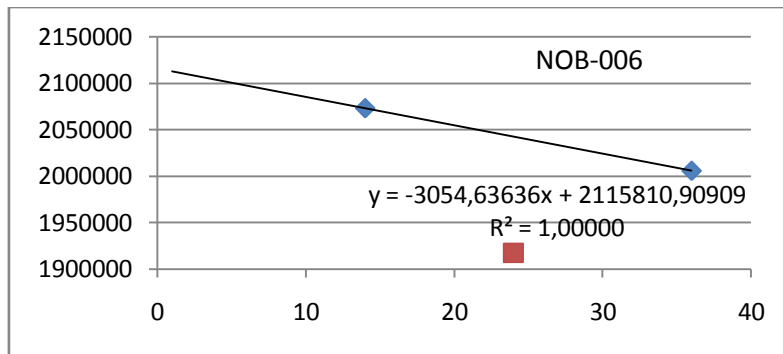
## APPENDIX

### APPENDIX I: SAMPLES POSITION AND RHOD

Glass poss. of NOB-013	Sample Number	RhoD	Glass poss. of NOB-003	Sample Number	RhoD
1	<b>IRMM 3-2</b>	2086925	1	<b>IRMM 1/2</b>	2050229,454
2	BG-087	2081699	2	JN-16	2040713,443
3	BG-086	2076474	3	JN-15	2031197,431
4	BG-137	2071248	4	JN-14	2021681,419
5	BG-138	2066022	5	JN-13	2012165,408
6	BG-139	2060797	6	JN-12	2002649,396
7	BG-140	2055571	7	JN-19	1993133,385
8	BG-069	2050346	8	JN-20	1983617,373
9	BG-068	2045120	9	BG-02	1974101,361
10	BG-122	2039894	10	BG-01	1964585,35
11	BG-121	2034669	11	BG-22	1955069,338
12	BG-142	2029443	12	BG-23	1945553,327
13	BG-067	2024218	13	JN-21	1936037,315
14	<b>IRMM 3-1</b>	2018992	14	<b>IRMM 2/2</b>	1926521,303
15	BG-091	2013766	15	JN-23	1917005,292
16	BG-092	2008541	16	JN-22	1907489,28
17	BG-093	2003315	17	BG-32	1897973,269
18	BG-143	1998090	18	BG-33	1888457,257
19	<b>Dur</b>	1992864	19	<b>Dur</b>	1878941,245
20	<b>FCT</b>	1987638	20	<b>Lim</b>	1869425,234
21	BG-063	1982413	21	<b>FC</b>	1859909,222
22	BG-120	1977187	22	BG-34	1850393,21
23	BG-119	1971962	23	JN-07	1840877,199
24	BG-062	1966736	24	JN-02	1831361,187
25	BG-061	1961510	25	JN-03	1821845,176
26	BG-118	1956285	26	<b>IRMM 3/2</b>	1812329,164
27	<b>IRMM 3-4</b>	1951059	27	JN-06	1802813,152
28	BG-066	1945834	28	JN-01	1793297,141
29	BG-117	1940608	29	JN-05	1783781,129
30	BG-144	1935382	30	BG-31	1774265,118
31	BG-145	1930157	31	BG-43	1764749,106
32	BG-165	1924931	32	BG-35	1755233,094
33	BG-162	1919706	33	BG-37	1745717,083
34	BG-161	1914480	34	BG-38	1736201,071
35	BG-160	1909254	35	BG-39	1726685,06
36	BG-159	1904029	36	BG-40	1717169,048
37	BG-158	1898803	37	BG-41	1707653,036
38	BG-164	1893578	38	<b>IRMM 4/2</b>	1698137,025
39	BG-163	1888352			
40	<b>IRMM 3-3</b>	1883126			

APPENDIX II:

REGRESSION LINES TO OBTAIN RHOD VALUES IN ODER TO DETERMINE ZETA VALUE



APPENDIX III: FIELD DESCRIPTIONS

	UTM position (32N)		Elevation	Municipality	Locality	Outcrop	Lithology	Structural measurements			
	East	North						Dip dir.	Dip	Type	Comment
BG-031	293869	6637381	15	Fitjar	Western Stord, road from Petarteigen to Skardet (sign to Dáfjorden), ca. 140 m northwest of the driveway to the school and ca. 30 m south of a driveway to private houses	Roadcut, ca. 7 m high x 60 m wide, rel. fresh	Medium-grained, light green granitoid; grey, smokey qz, white to green fsp, dark green ?, black bt; pyrite on joints (or faults?); many joints have a white or pink alteration zone	112	59	Fault	
								82	70	Fault	
								128	29	Joint	Dominant joint direction, dm-spacing
								139	29	Joint	Dominant joint direction, dm-spacing
								133	35	Joint	Dominant joint direction, dm-spacing
								119	30	Joint	Dominant joint direction, dm-spacing
								135	32	Joint	Dominant joint direction, dm-spacing
								299	53	Joint	Secondary joint direction, m- to 10s of m-spacing
								173	54	Joint	Secondary joint direction, m- to 10s of m-spacing
								58	80	Joint	Secondary joint direction, m- to 10s of m-spacing
BG-037	292307	6612195	20	Sveio	Buavåg, road no. 541 from Buavåg to Haugesund, ca. 100 m southwest of the road to Sveio	Roadcut, ca. 4 m high x 50 m wide, fresh	Grey, medium- to coarse-grained tonalite (?); qz, fsp, bt; foliation varies between none at all and moderate; some sheared layers, locally with qz-veins, more or less parallel to the foliation; xenoliths of dark grey, fine-grained gneiss, dm- to m-size; some qz-fsp+/-bt pegmatie veins	293	44	Foliation	
								262	36	Foliation	
								290	52	Foliation	

BG-038	288527	6604327	10	Sveio	Road to Ryvarden Lighthouse, ca. 200 m from the turning area ("snuplass") at the end of the public road	Roadcut, ca. 6 m high x 40 m wide; rather overgrown with lichen and slightly weathered at the surface	Coarse-grained augengneiss; bt-rich with large (several cm diametre) augen of fsp (and sometimes qz?); cm- to dm thick qz-rich layers and some finer grained sheared layers	336	49	Foliation	
								337	39	Foliation	
								335	40	Foliation	
BG-061	310685	6605786	255	Vindafjord	Langåsdalen (between Skjold and Vikebygd), in the brook, ca. 700 m east of the eastern end of Langåsdalsvatnet	Outcrops in small brook, strongly weathered and overgrown by lichen	Greenish-grey, fine- to medium-grained tonalitic gneiss; bt, hbl(?), plg, +qz?; strongly foliated; veins and cavities filled with qz	94	89	Foliation	
								85	84	Foliation	
								79	87	Foliation	
								173	80	Joint	
								6	76	Joint	
								5	81	Joint	
BG-062	309407	6605091	455	Vindafjord	Vassnuten (between Skjold and Vikebygd), close to top, ca. 50 m southwest of small tarn	Outcrops on mountain top, strongly weathered and overgrown by lichen	Medium- to coarse-grained granite; qz, fsp, bt; generally unfoliated, but locally foliated zones of several dm width; many qz-fsp-ms pegmatite dykes	103	56	Joint	Dominant joint direction
								107	58	Joint	Dominant joint direction
								91	72	Joint	Dominant joint direction
								358	67	Joint	Secondary joint direction
BG-063	305611	6605304	35	Vindafjord	Road from Skjold/Isvik to Vikebygd, between turnoffs to Trovåg and Bjørndal/Langåsdalen, at turnoff to Kriken/Tongafæl/Svensbøøy	Roadcut, ca. 2 m high x 10 m wide, fresh	Porphyritic granite, light grey to light pink, white when weathered; Kfsp up to 4 cm long in medium- to coarse-grained matrix of qz, fsp, bt, +ms(?); bt-rich patches and schlieren; 10 cm wide pegmatite dyke (qz, pink fsp, bt, +ms?); locally swirly patterns of flow-aligned Kfsp phenocrysts	9	35	Joint	Dominant joint direction?, dm- to m-spacing

								17	36	Joint	Dominant joint direction?, dm- to m-spacing
								18	32	Joint	Dominant joint direction?, dm- to m-spacing
								267	65	Joint	Secondary joint direction?, dm- to m-spacing
								251	77	Joint	Secondary joint direction?, dm- to m-spacing
								154	44	Joint	Secondary joint direction?, dm- to m-spacing
								4	80	Joint	Secondary joint direction?, dm- to m-spacing
BG-066	318746	6613628	30	Vindafjord	Road no. 543 from Ølsvågen to Innbjøa, south of Ulvanes, opposite small forest (with house in the middle) east of the road	Roadcut, ca. 1.5 m high x 10 m wide, rel. fresh	Grey granodioritic (?) gneiss; qz, fsp, bt; fsp augen of up to 2 cm size in medium-grained matrix; well foliated	325	11	Foliation	
								171	82	Joint	
								183	83	Joint	
BG-091	295360	6592744	45	Tysvær	Førre, road to "Førre Hageby" and "Førre Terrasse", turnoff of new road to new apartment blocks, ca. 80 m southeast of the southeastern end of the tunnel on road no. E134	Roadcut, 3-7 m high x >100 m wide, fresh	At sample location: light grey to brownish-grey granite; medium- to coarse-grained; qz, fsp, bt; unfoliated to poorly foliated. Higher up along the road: migmatitic gneisses; pegmatite dykes (qz, pink fsp, bt, ms)	34	89	Joint	dm-spacing
								241	84	Joint	dm-spacing
								248	80	Joint	dm-spacing
								247	83	Joint	dm-spacing
								268	80	Joint	dm-spacing
								271	85	Joint	dm-spacing
								269	83	Joint	dm-spacing
								279	86	Joint	dm-spacing
BG-117	319287	6614902	5	Vindafjord	Road from Ølen to Dreganes, ca. 1 km south of the end of the road, opposite some boat/holiday houses	Small roadside quarry, ca. 10 m high x 40 m wide, fresh	Dark grey gneiss, granodioritic-tonalitic?; fsp, hbl, bt, +qz?; medium-grained with larger (1-10 mm) fsp; mostly poorly foliated but some areas are well foliated; layers and schlieren of coarse-grained qz; complexly folded	318	70	Foliation	
								74	76	Joint	m- to several m-spacing

BG-118	313356	6606004	55	Vindafjord	Road to Blikrabygda, ca. 200 m southeast of turnoff from road no. E134 and ca. 70 m east of the road to Blikrabygda along new gravel road to new building site	Freshly bulldozed outcrop, ca. 12 m wide x 1 m high	Grey, well foliated, medium-grained gneiss; qz, fsp, bt, hbl?; bt locally oxidised to brownish or metallic colours; qz-fsp layers (mm to cm thick) and augen-shaped aggregates	254	82	Foliation	
								331	89	Joint	Several m-spacing
								324	75	Joint	Several m-spacing
BG-119	308169	6601575	80	Vindafjord	Road no. E134, ca. 1.4 km (along the road) east-northeast of Skjold church, opposite bus stop	Roadcut, ca. 100 m wide x max. 4 m high, fresh	Grey tonalitic(?) gneiss, very homogenous, medium- to coarse-grained; poorly foliated; qz, fsp, bt, hbl?	63	74	Foliation	
								313	69	Fault	
								311	70	Fault	
								312	70	Fault	
								65	66	Joint	
								83	66	Joint	
								82	49	Joint	
								199	76	Joint	
								192	80	Joint	
BG-120	306591	6600792	20	Vindafjord	Road along the coast from lsvik to Skjoldavik, small quarry above the road, ca. 90 m northeast of the garbage/recycling station, ca. 200 east of where the road crosses road no. E134	Small quarry, ca. 100 m long x max. 6 m high, fresh	Grey gneiss, homogenous, poorly foliated, medium- to coarse-grained; qz, fsp, bt, +greenish ?; fine-grained, darker xenoliths, rounded or smeared out to schlieren; qz-fesp pegmatite veins and dykes; locally shear bands; outside the quarry interlayered with amphibolite	5	88	Joint	m- to several m-spacing
								189	85	Joint	m- to several m-spacing
								71	58	Joint	m- to several m-spacing
								265	90	Joint	m- to several m-spacing
								238	90	Joint	m- to several m-spacing
								274	75	Pegmatite dyke	

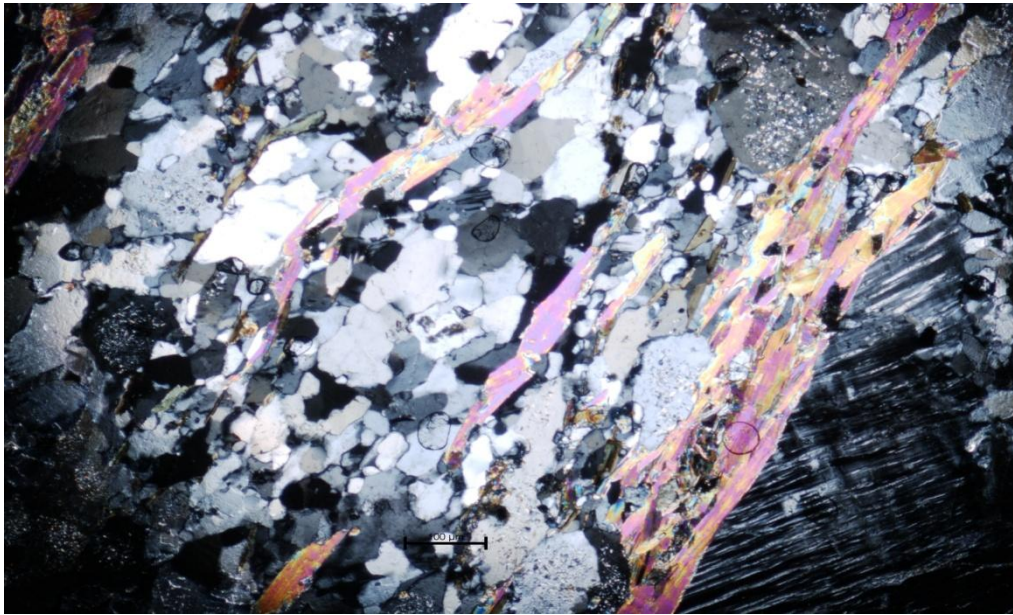
BG-137	283116	6672615	10	Austevoll	Kvaløy, along road no. 156, ca. 60 m SE of the bridge to Stora Kalsøy (Bakkasund) and ca. 250 m NW of the bridge to Nautøy, due N of a house	Roadcut, 60 m wide x max. 5 m high, fresh	Grey, locally greenish, medium- to coarse-grained quartz-diorite (?); qz, fsp, bt, greenish ?; very weakly foliated; locally larger (up to 3 cm) idiomorph fsp phenocrysts; fsp-qz pegmatite veins mostly cm-wide but up to 30 cm	61	55	Fault	
								120	36	Striations on fault plane	
								259	88	Joint	m-spacing
								143	89	Joint	m-spacing
								108	65	Joint	m-spacing
								82	90	Joint	m-spacing
								104	36	Joint	m-spacing
								237	59	Joint	m-spacing
								239	17	Joint	m-spacing
								87	57	Joint	m-spacing
								192	71	Joint	m-spacing
								18	85	Joint	m-spacing
								280	40	Joint	m-spacing
BG-138	284953	6672004	10	Austevoll	Hundvåkøy, along road no.153, ca. 125 m NW of turnoff to Barmen bay and quay, SW of the only house in the area	Roadcut, ca. 30 m wide x 4 m high, fresh	Grey to greenish, medium- to coarse-grained quartz-diorite (?); qz, fsp, bt, greenish ?, titanite; some pink qz-fsp pegmatite veins, 1-10 cm wide; locally very weak foliation; some finer grained shear bands	171	60	Fault	m-spacing
								237	40	Striations on fault plane	
								202	16	Fault	m-spacing
								141	6	Striations on fault plane	
								244	85	Fault	m-spacing
								159	1	Striations on fault plane	
								1	87	Fault	m-spacing
								268	54	Striations on fault plane	
								108	73	Joint	m-spacing
								224	49	Joint	m-spacing
								81	84	Joint	m-spacing
								204	58	Joint	m-spacing

BG-139	289539	6668624	25	Austevoll	Northern Huftarøy, along road no. 546, ca. 150 m SE of the dam to Indreholmen, opposite the entrance to the new parking/viewing area	Roadcut, >100 m wide x max. 12 m high, fresh	Dark grey granodiorite (?); grain size variable from fine to coarse but mostly medium-grained; fsp, bt, hbl (?), qz?; content of mafic minerals varies somewhat; network of many thin (mm-cm) and a few thicker (cm-dm) qz-fsp pegmatite and qz veins; locally weakly foliated; many undulating shear planes/faults with greenish-brown coating	192	58	Fault	
								248	37	Striations on fault plane	
								175	36	Fault	
								198	18	Fault	
								45	89	Joint	
								50	78	Joint	
								47	74	Joint	
								281	25	Joint	
								281	36	Joint	
								251	21	Joint	
								347	35	Joint	
								97	58	Fault	
								BG-140	293941	6681341	60
186	70	Fault									
259	31	Striations on fault plane									
54	75	Fault									
90	59	Fault									
208	40	Joint	several dm- to several m-spacing								
202	76	Joint	several dm- to several m-spacing								
194	61	Joint	several dm- to several m-spacing								
47	48	Joint	several dm- to several m-spacing								
248	84	Joint	several dm- to several m-spacing								
128	59	Joint	several dm- to several m-spacing								
159	81	Joint	several dm- to several m-spacing								
231	66	Joint	several dm- to several m-spacing								



BG-143	303142	6597965	85	Vindafjord	Road no. E134 between Våg and Isvik/Skjold, ca. 80 m SSW of the turnoff to Liavik swimming beach and Dancer Holding AS, outcrop along the small parallel road E of E134, approximately between the bus stop and the tunnel under E134	Roadcut, ca. 100 m wide x 7 m high, fresh	Dark grey gneiss, mostly fine-grained but with larger ms (up to 1 cm); moderately foliated; qz-fsp pegmatite veins of variable thickness (cm-dm-1m); outcrop locally strongly fractured; rusty brown staining common on fracture planes	1	41	Foliation	
								329	32	Lineation	
								131	76	Joint	Dominant joint direction, m-spacing
								126	79	Joint	Dominant joint direction, m-spacing
								160	80	Joint	Dominant joint direction, m-spacing
								64	86	Joint	Secondary joint direction, several m-spacing
								60	87	Joint	Secondary joint direction, several m-spacing
								253	74	Joint	Secondary joint direction, several m-spacing
BG-144	324568	6613977	190	Etne	Road no. E134 between Ølen and Etne, ca. 120 m NNE of "kommunegrense" Vindafjord/Etne, small quarry W of road	Small quarry, ca. 30 m wide x max. 10 m high, fresh	Grey gneiss; thinly banded with qz-rich layers and mica-rich layers; moderately to well foliated; qz, fsp, bt, hbl?, ms; micas are corroded, bt is brownish; grainsize mostly fine to medium but some qz-layers are coarse to very coarse; locally fsp augen texture	308	15	Foliation	
								93	74	Fault	
								137	52	Striations on fault plane	
								94	71	Joint	m- to several m-spacing
								115	76	Joint	m- to several m-spacing
								189	72	Joint	m- to several m-spacing
								189	81	Joint	m- to several m-spacing
								181	78	Joint	m- to several m-spacing

#### APPENDIX IV: THIN SECTIONS

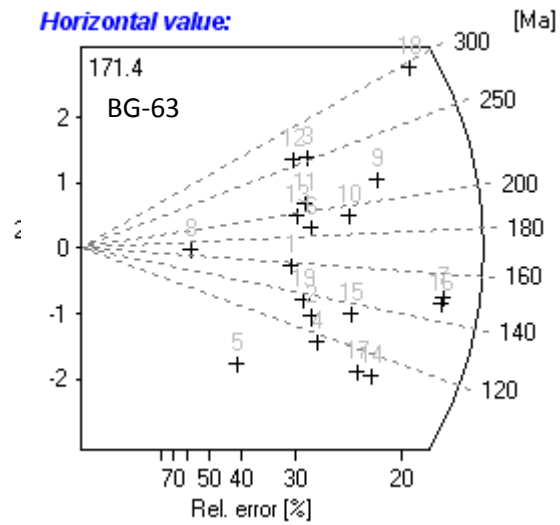
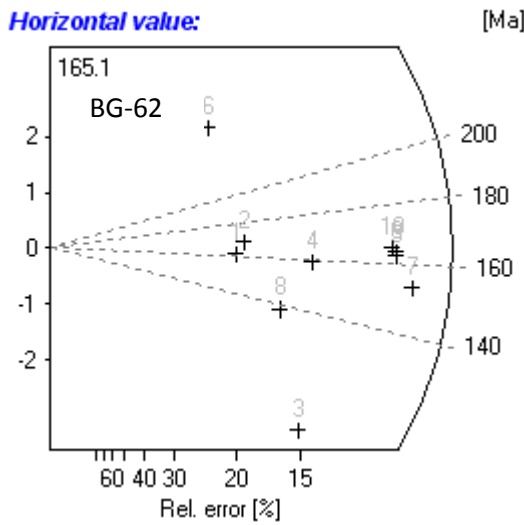
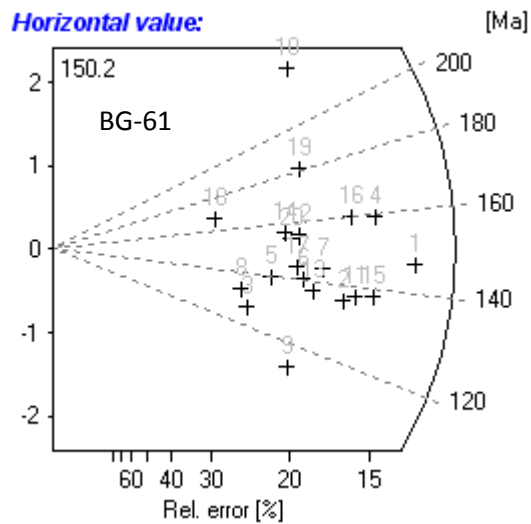
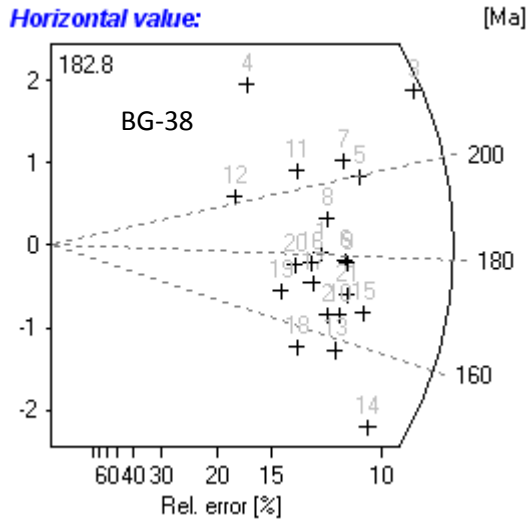
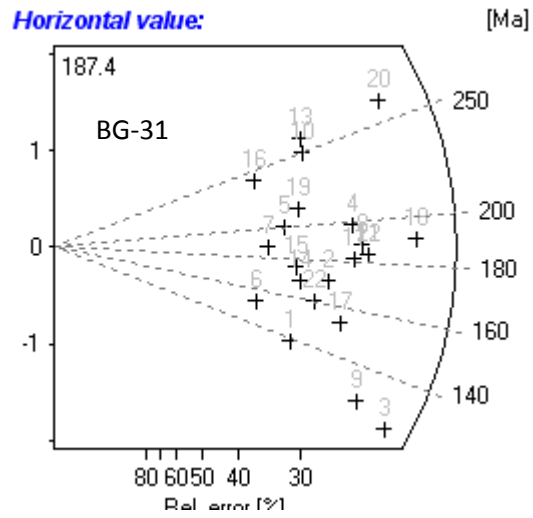
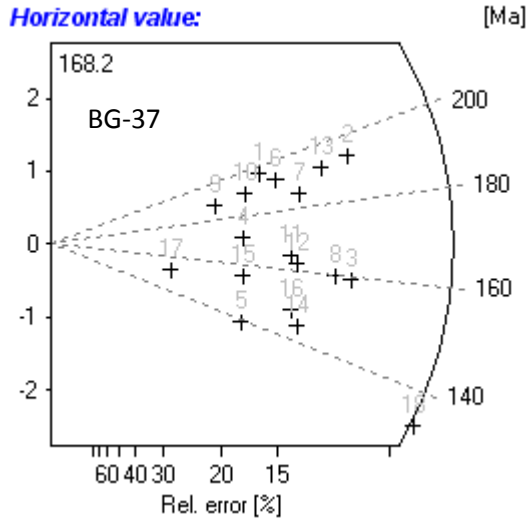


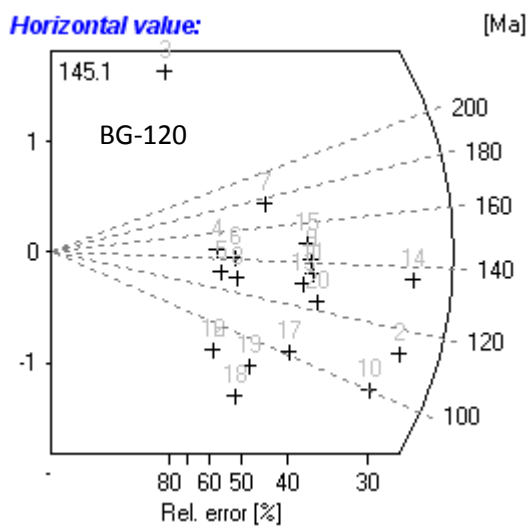
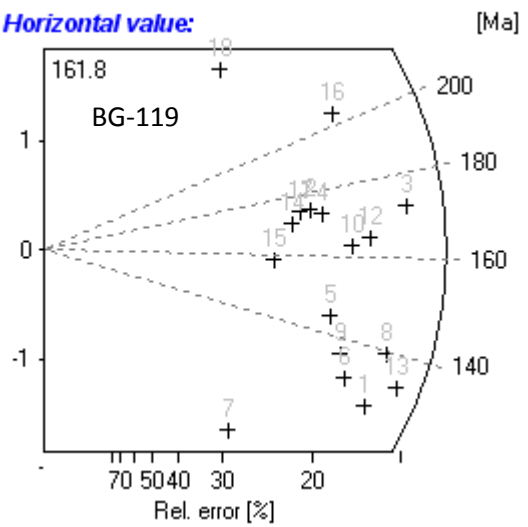
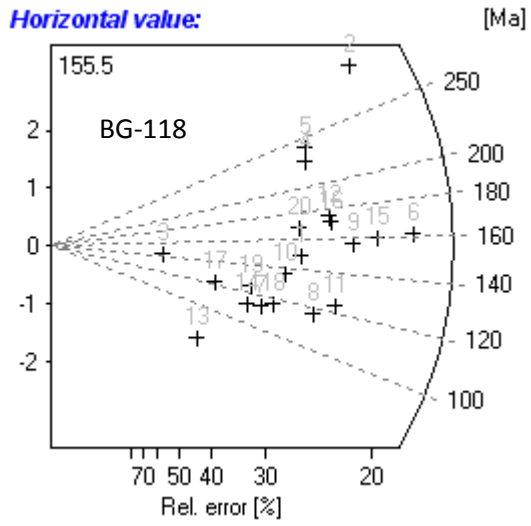
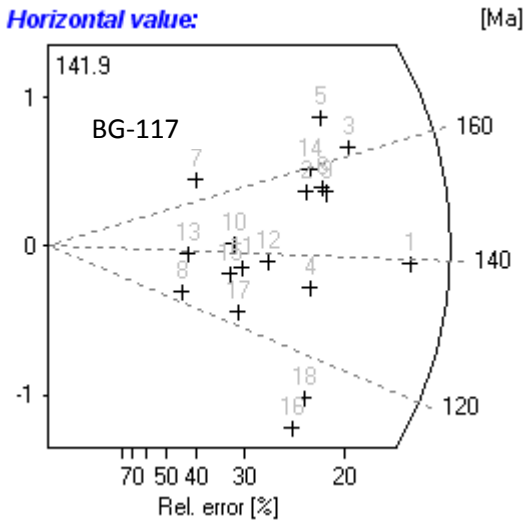
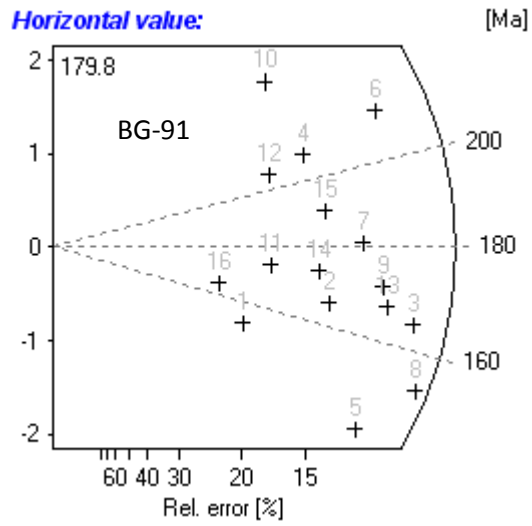
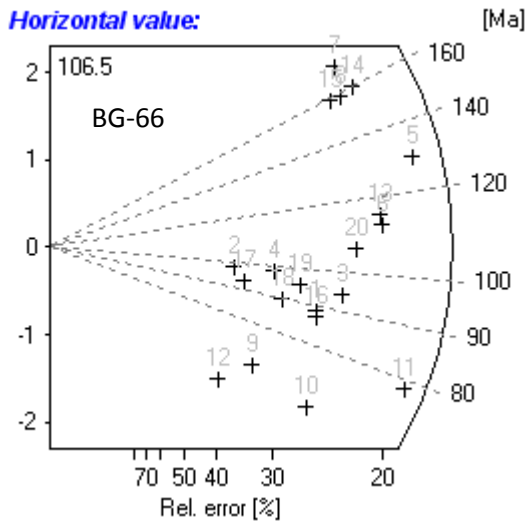
Thin section of augen gneiss consists mainly of anhedral quartz, muscovite with high interference colors (XP) and low relief in (PP), minor biotite (high relief in PP, brown in XP). Plagioclase in the lower right corner shows twinning; meanwhile the upper one has been altered to micaceous materials.



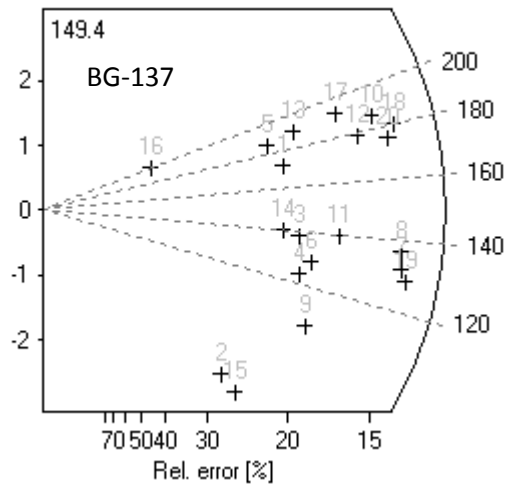
Thin section of gneiss composes domiantely of anhedral quartz, minor muscovite (high interference color at XP), rare biotite and hornblende. Plagioclase shows twinning in the center lower part and has been altered at the upper part.

APPENDIX V: RADIAL PLOTS

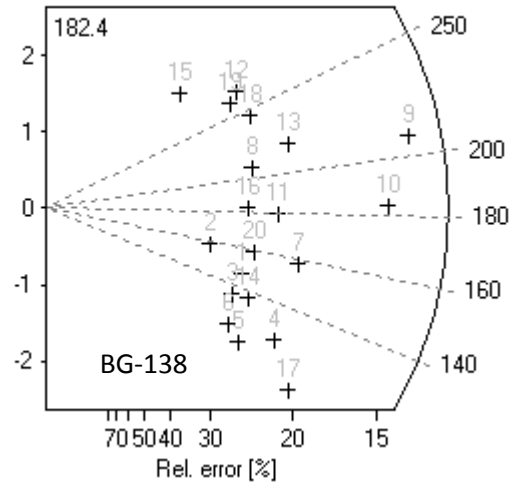




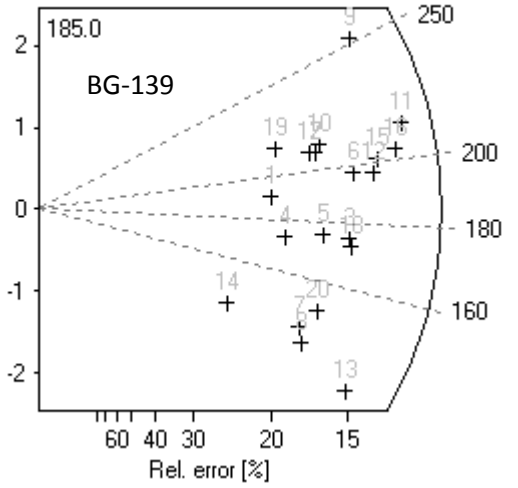
Horizontal value:



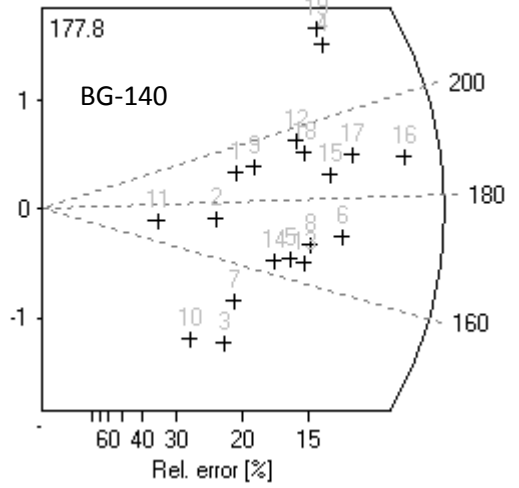
Horizontal value:



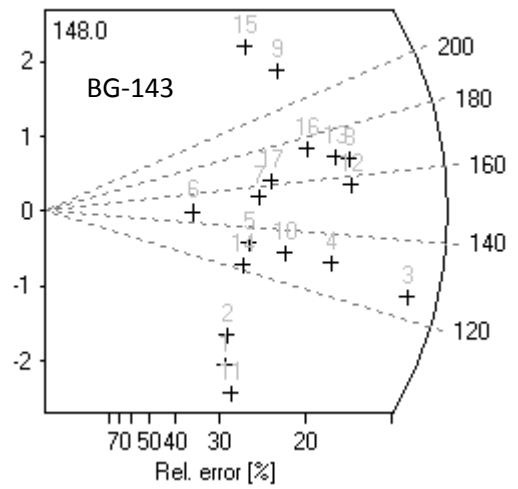
Horizontal value:



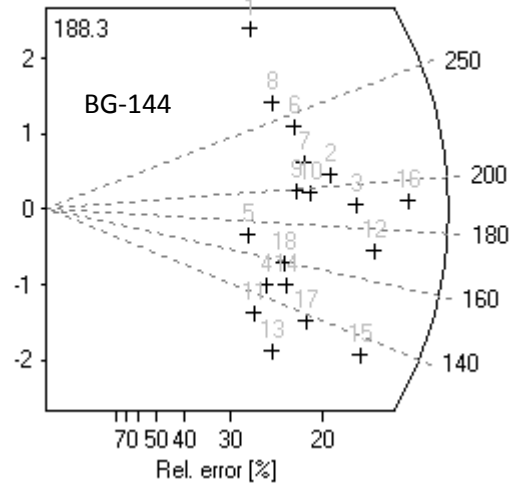
Horizontal value:



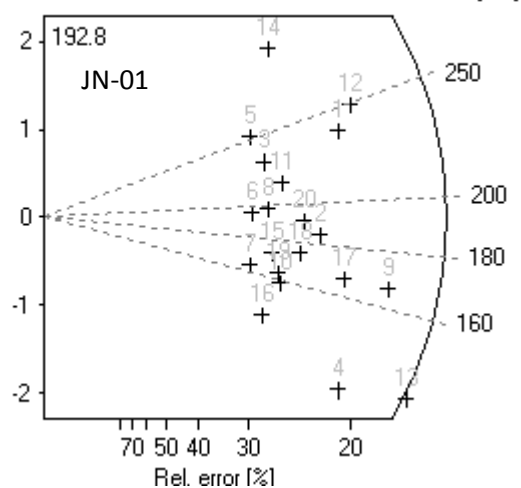
Horizontal value:



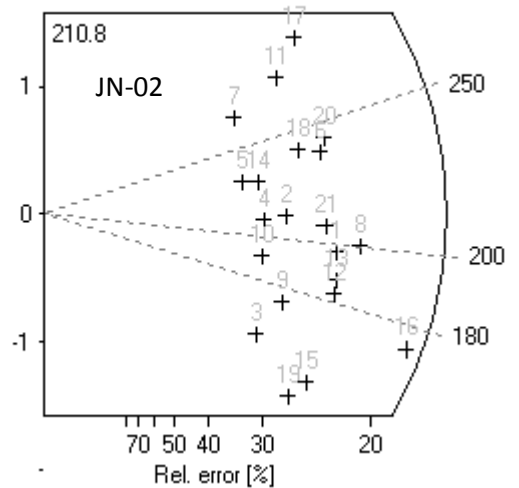
Horizontal value:



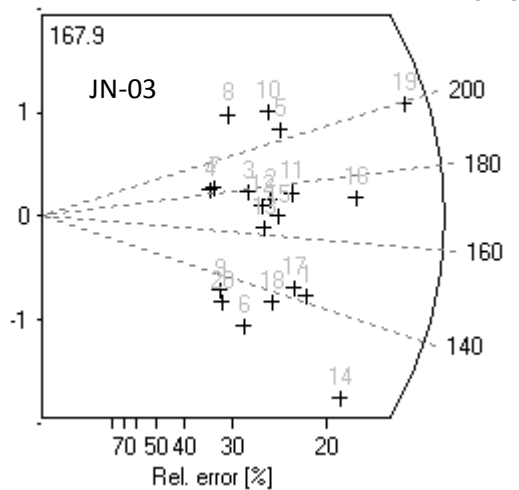
Horizontal value:



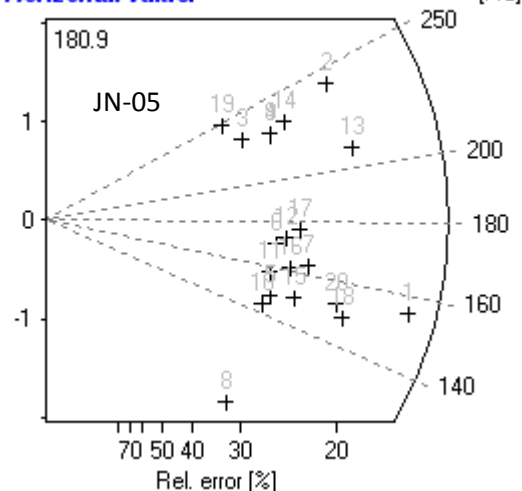
Horizontal value:



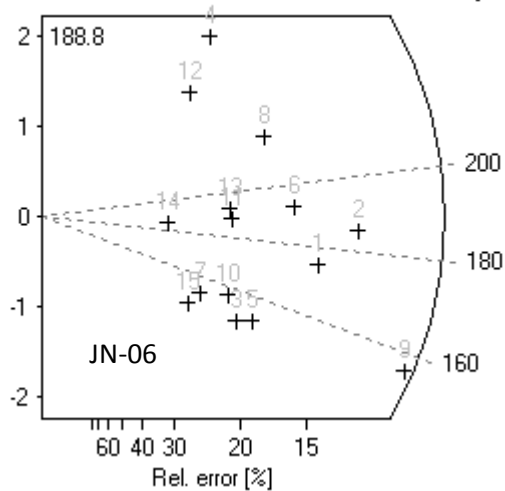
Horizontal value:



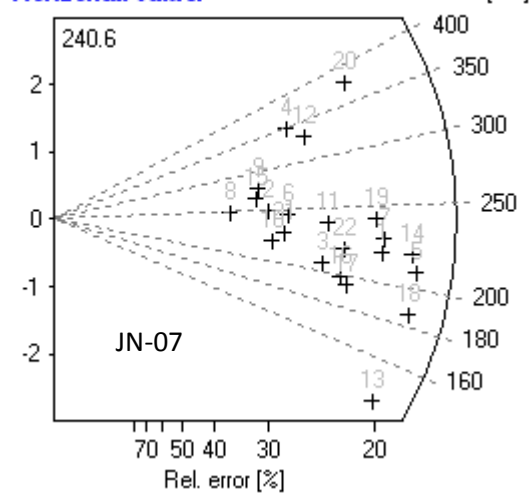
Horizontal value:



Horizontal value:

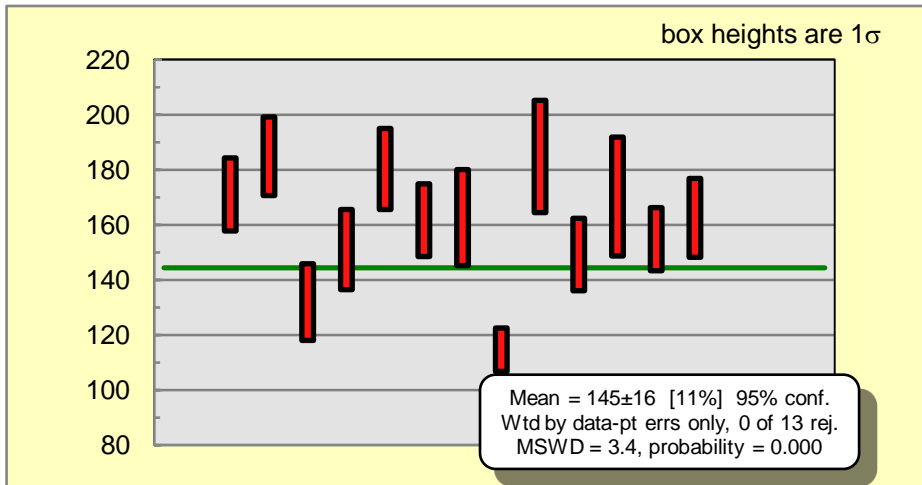


Horizontal value:



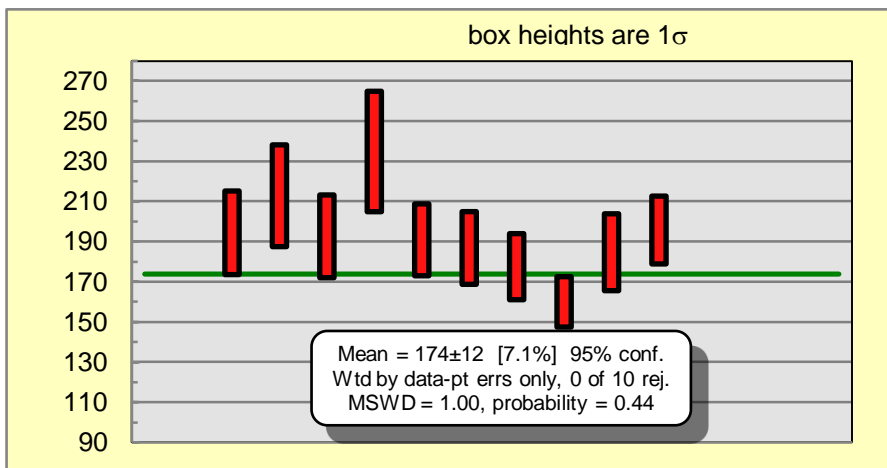
APPENDIX VI:

THE WEIGHTED MEAN OF AFT AGE FOR THE FOOTWALL OF THE HSZ

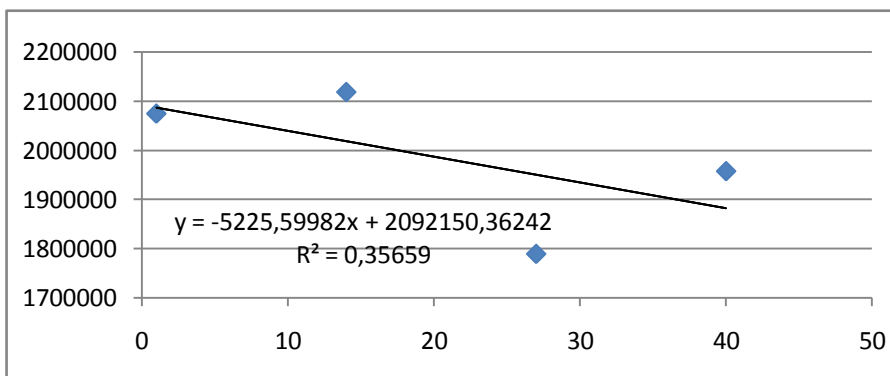


APPENDIX VII:

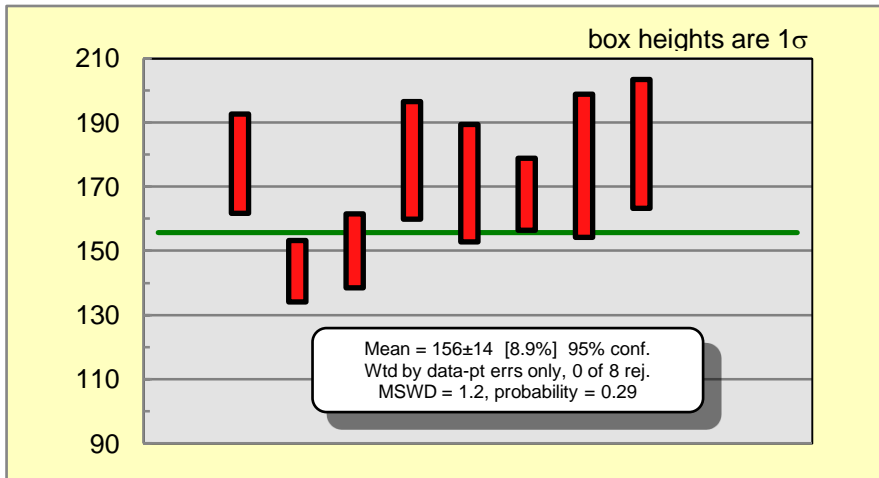
THE WEIGHTED MEAN OF AFT AGE FOR THE HANGING WALL OF THE HSZ



APPENDIX VIII: CALCULATION RHOD FOR NOB-013



APPENDIX IX: THE WEIGHTED MEAN OF AFT AGE FOR THE FOOTWALL OF THE HSZ (MAGERHOLM'S AREA)



APPENDIX X: THE WEIGHTED MEAN OF AFT AGE FOR THE HANGING WALL OF THE HSZ (MAGERHOLM'S AREA)

